博士論文

Development of a 3D 4-mirror optical cavity
for the ILC polarized positron source

（ILC 偏極陽電子源の為の
3 次元 4 枚鏡光共振器の開発）

赤 木　智 哉

広島大学大学院先端物質科学研究科

2013 年 9 月

目次

１．主論文

Development of a 3D 4-mirror optical cavity for the ILC polarized positron source
（ILC 偏極陽電子源の為の 3 次元 4 枚鏡光共振器の開発）
赤木　智哉

２．公表論文

Development of a three dimensional four mirror optical cavity for laser-Compton scattering
T. Akagi, S. Araki, Y. Funahashi, Y. Honda, H. Kataoka, T. Kon, S. Miyoshi, T. Okugi, T. Omori, K. Sakaue, H. Shimizu, T. Takahashi, R. Tanaka, N. Terunuma, J. Urakawa, M. Washio and H. Yoshitama
Nuclear Instruments and Methods in Physics Research Section A **724,** 63-71 (2013).

３．参考論文

(1) Photon generation by laser-Compton scattering at the KEK-ATF
S. Miyoshi, T. Akagi, S. Araki, Y. Funahashi, T. Hirose, Y. Honda, M. Kuriki, X. Li, T. Okugi, T. Omori, G. Pei, K. Sakaue, H. Shimizu, T. Takahashi, N. Terunuma, J. Urakawa, Y. Ushio and M. Washio
Nuclear Instruments and Methods in Physics Research Section A **623,** 576－578 (2010).

(2) Production of gamma rays by pulsed laser beam Compton scattering off GeV-electrons using a non-planar four-mirror optical cavity
T. Akagi, S. Araki, J. Bonis, I. Chaikovska, R. Chiche, R. Cizeron, M. Cohen, E. Cormier, P. Cornebise, N. Delerue, R. Flaminio, S. Funahashi, D. Jehanno, Y. Honda, F. Labaye, M. Lacroix, R. Marie, C. Michel, S. Miyoshi, S. Nagata, T. Omori, Y. Peinaud, L. Pinard, H. Shimizu, V. Soskov, T. Takahashi, R. Tanaka, T. Terunuma, J. Urakawa, A. Variola and F. Zomer
Journal of Instrumentation **7**, P01021 (2012).

(3) Gamma-rays Generation with 3D 4-mirror Cavity for ILC Polarized Positron Source
T. Akagi, M. Kuriki, S. Miyoshi, T. Takahashi, R. Tanaka, H. Yoshitama, S. Araki, Y. Funahashi, Y. Honda, T. Okugi, T. Omori, H. Shimizu, N. Terunuma, J. Urakawa, K. Sakaue, M. Washio, H. Kataoka and T. Kon
Proceedings of IPAC2012, New Orleans, Louisiana, USA (2012).

主論文

Abstract

We performed a gamma ray generation experiment by means of reflecting laser photons off high energy electron beams (laser-Compton scattering) for the development of a polarized positron source of the International Linear Collider (ILC). The ILC is the project to build a 30 km long linear accelerator to search for new phenomena or explore the origin of the universe via electron-position interactions. In electron-positron interactions, the accuracy of measurements can be remarkably improved by using polarized beam, the ILC plans to use polarized electron beams. In addition, it is desirable to use polarized positron beams in order further to improve performance of the facility.

In general, polarized positrons are generated using polarized gamma rays. The polarized gamma rays are injected to a thin target and polarized positrons are created via pair creation processes. Therefore, making intense polarized gamma beams is a key issue to realize polarized positron sources. Laser-Compton scattering is a method to generate gamma rays through the inverse Compton scattering process. An advantages of this scheme is to generate gamma rays with relatively low energy electrons compared to the synchrotron radiation, thus the entire facility can be much smaller than the synchrotron facility.

In addition to the compactness of the facility, polarization of gamma rays are easily controlled by polarization of the laser photons. In the baseline design of the ILC, an undulator is installed in the main linac of the ILC where the energy of the electron is more than 150 GeV to generate gamma rays. The undulator scheme has potential difficulty such that, high energy electrons can be only provided by the main linac of the ILC and the control of the polarization is not as easy as the laser-Compton scheme. On the other hand, the energy of electron beams required for the positron production by laser-Compton scattering is about 1 GeV. An issue for the laser-Compton scattering is, however, the cross section of laser beam and electron beam is small and it is technically difficult to generate sufficient number of gamma rays required by the ILC positron source. The development of the technology is a key issue.

In this study, we develop a method to increase intensity of laser pulses by coherently stacking low energy laser pulses from a seed laser in an optical resonant cavity. In previous studies, we achieved a finesse of 1800 and a waist size of 30 µm in σ with the 2-mirror Fabry-Perot cavity and succeeded in generating photons by laser-Compton scattering. In order to further improve the number of gamma rays generated by laser-Compton scattering, it is necessary to increase the power enhancement factor and to reduce the waist size of the laser beam in the optical cavity. However, it is difficult to improve the power enhancement factor and focusing of laser beam simultaneously with a 2-mirror Fabry-Perot cavity. Therefore, we developed a 3D 4-mirror cavity to achieve higher power enhancement factor and smaller waist size simultaneously.

We performed an R&D to increase the intensity of the laser beam using the 3D 4-mirror optical cavity. The 3D 4-mirror cavity has an advantage over 2-mirror

Fabry-Perot cavity; high tolerance for the misalignment of optical components. By utilizing this feature, improvement of the finesse and the waist size of laser beam can be achieved simultaneously. In the case of a planar 4-mirror cavity, the effective focal length in the tangential plane and the sagittal plane, is different, which causes astigmatism at the focal point. To avoid astigmatism, we designed the 3D 4-mirror cavity in which the laser light circulates 3 dimensional trajectory. The 3D 4-mirror cavity has properties that it only resonates separately with the left or right circularly polarized laser beam at different optical paths due to the geometric phase originated with the 3D (twisted) optical path and the profile of the laser pulses in the cavity in principle elliptic shape. We optimized the three dimensional configuration of mirrors of the cavity to maximize the efficiency of laser-electron interaction.

The optical cavity consists of two flat mirrors and two concave mirrors. The reflectivity of the coupling mirror is 99.9% while the other's is 99.99%. The performance of an optical cavity can be denoted by a parameter called finesse (F) which is defined by the reflectivity of mirrors. The power enhancement factor becomes larger and width of resonance peak becomes narrower as the finesse becomes higher. The required accuracy of the optical path in order to keep resonance of the optical cavity becomes severe as the finesse becomes high. The measured finesse of the 3D 4-mirror cavity was $F = 4000$. The power enhancement factor was estimated to be 1200 which was estimated with measured finesse and the transmittance of the coupling mirror. We also estimated the stored power in the cavity from the measurement of the transmitted and the reflected power and found that two measurements are consistent each other.

We installed the 3D 4-mirror cavity in the KEK-ATF damping ring to perform an experiment on gamma ray generation by laser-Compton scattering. The energy of the electron beam is 1.28 GeV and the ATF is operative up to 10 bunches per train with the bunch separation of 5.6 ns. The experiment was performed in single and 5 bunches per train. We used a mode-locked laser whose wave length, repetition rate, average power were, 1064 nm, 357 MHz, and 10 W, respectively. The crossing angle of the laser and the electron beams was 14°, which determined the maximum energy of the gamma ray at 28 MeV. The energy of the gamma rays in the detector acceptance is 19–28 MeV with the average of 24 MeV, which was limited by the slit of 0.26 mrad aperture placed between the laser-electron interaction point and the detector.

The average of 2.6 kW of laser light was successfully accumulated in the optical cavity which corresponded to the power enhance factor of 1200. The fluctuation of stored power was 1.5%, it means that the length of optical path was controlled with the precision of about 4 pm. The laser beam spot sizes in its major and minor axis were estimated to be 27 µm and 10 µm respectively from the measurement of transmitted beam profile. The size of laser beam in vertical direction was estimated to be 13 µm from the laser beam position scan. It was consistent with the estimation from transmitted beam profile. The average of 124 ± 1 photons per collision was generated in the detector acceptance in 5 bunch operation of the ATF. It corresponded to the photon intensity of 2.7×10^8 photons per second. The number of generated gamma ray is consistent with the estimation by the numerical

simulation.

For the ILC positron source, we need further improvement of the gamma ray generation efficiency. The requirement of power enhancement factor of the optical cavity for laser-Compton scheme is approximately 10^4, which is about ten times higher than present status. We plan to replace mirrors of the cavity with higher reflectivity ones aiming at finesse of 30000 or more. In this study, we achieved control accuracy of the length of optical path of 4 pm. It indicates that target finesse can be achieved from a viewpoint of a feedback system. On the other hand, we observed effect of the thermal load on mirror when high power laser was accumulated in the cavity. For accumulation of higher power, use of ultra low loss mirrors is indispensable.

In this study, laser-Compton scattering experiments were performed using the 3D 4-mirror cavity and improvement of gamma rays generation efficiency was demonstrated. We also found issues and possible solutions to further improve gamma ray intensity which shows a clear direction of future research and development.

Contents

List of Figures

List of Tables

Chapter 1

Introduction

1.1 Photon source

High energy photons (i.e. X-ray or gamma ray) are widely applied in fields such as high energy physics, biological science, material science and medical science. For example, evaluation of the spin polarization of spintronic materials using high energy X-rays is expected to be applied in fundamental research of the giant magnetoresistive (GMR) effect, which is used in the driving principle of magnetic heads in hard disk drives [1]. X-rays are used in medical imaging such as X-ray phase-contrast imaging. Talbot interferometer allows the visualization of soft tissue, which is hard to be imaged by conventional X-ray imaging [2]. In this work, we have studied a scheme for gamma ray source using laser-Compton scattering for the ILC polarized positron source which required intense gamma rays of O(10 MeV).

Synchrotron radiation has been widely used as high energy photon sources. It has many features such as natural collimation, high intensity, broad spectral bandwidth, high polarization and pulsed time structure, which make it useful for wide variety of applications [3]. For example, Super Photon ring-8 GeV (SPring-8, Japan) [4] is a third-generation synchrotron radiation facility. In SPring-8, the radiation ranging from soft X-ray (300 eV) to hard X-ray region (300 keV) is available. However, a disadvantage of synchrotron radiation facilities is their scale both in the size and the cost. SPring-8 is an accelerator facility of 1436 m long electron storage ring whose scale would be a level of to be constructed only a few in a country. On the other hand, a compact photon source by means of reflecting laser photons off high energy electron beams (laser-Compton scheme) has advantageous to synchrotron radiation and has been developed extensively in these years. Fig. 1.1 shows schematic of laser-Compton scattering. The laser-Compton scheme has several advantages over the synchrotron radiation facilities. First, it is capable to generate high energy photons with relatively low energy electrons compared to synchrotron radiation. For example, in the laser-Compton scheme, O(10 MeV) photon can be generated with the O(1 GeV) electron while the synchrotron radiation facility requires O(100 GeV) to generate the same energy. Second, the energy of photons depends on scattering angle thus we can obtain quasi-monochromatic photons by cutting out photons scattered in a small angle. Third, polarization of photons are easily controlled by controlling polarization of

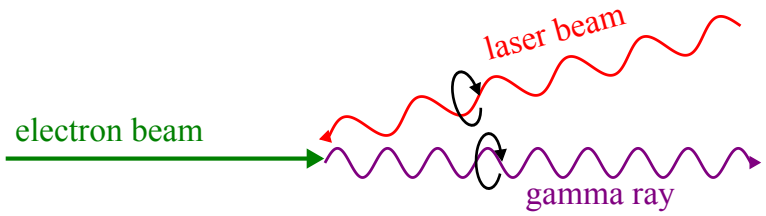

Figure 1.1: Laser-Compton scattering.

the laser photons.

The key issue for the laser-Compton scheme is to generate intense photon beams required by practical applications. A straightforward way to solve the problem is using a high power laser system to increase efficiency of laser-Compton scattering. However this Brute Force method would spoil an advantage of laser-Compton scattering, i.e., compactness. Other scheme to increase the intensity of the laser beam is to accumulate laser pulses in an optical resonant cavity in which laser pulses are coherently stacked so that the intensity is effectively increased. In addition, laser beam is focused at the laser-electron interaction point to increase the luminosity. The development of an optical cavity is main issue of this thesis.

1.2 Generation of gamma rays at the ATF

The purpose of the study is producing polarized positrons for the ILC by laser-Compton scattering. We have developed a high energy photon generation system using an optical resonant cavity at the KEK-ATF electron ring [5, 6]. The energy of the ATF electron beam is 1.28 GeV, with which we could make a photon beam of O(10 MeV) by the laser-Compton scattering. In the previous studies, we achieved the finesse of 1800 and the waist size of 30 µm in σ at the focal point of the laser beam with the 2-mirror Fabry-Perot cavity and succeeded to generate photons by laser-Compton scattering [7, 8]. However, the intensity needs further improvement to meet the requirement for the ILC polarized positron source. In terms of optical cavities, it is difficult to improve the finesse and focusing of the laser beam simultaneously with the 2-mirror Fabry-Perot cavity. Therefore, we developed a 4-mirror ring cavity to achieve high finesse and smaller waist size simultaneously. The 4-mirror cavity has advantage such as; the smaller laser beam waist is achievable with a confocal optics, thus the cavity has high tolerance for the misalignment of optical components. However, it is found that the laser beam profile in the cavity is astigmatic and is not ideal for laser-electron interaction when all 4 mirrors are placed in the same plane [9], we designed a cavity with 3 dimensional (3D) mirror configuration to avoid the astigmatic profile.

The 3D 4-mirror cavity consists of the mirrors of higher reflectivity than 2-mirror cavity to improve the finesse. The cavity achieved the finesse of 4000 with the vertical laser beam spot size of 13 ± 1 µm in σ at the laser-electron interaction point. We installed the cavity in the ATF in summer of 2011 and have performed gamma rays generation experiments by laser-Compton scattering. As a result, we have observed 2.7×10^8 photons per second with average energy of 24 MeV, and

demonstrated improvement of intensity of gamma rays.

1.3 About this thesis

In this thesis, studies of the 3D 4-mirror optical cavity for intense photon sources by laser-Compton scattering are presented. Chapter 2 introduces the International Linear Collider, e.g. purpose of the ILC, significance of polarized positron beams and positron sources. Chapter 3 describes the theoretical backgrounds of the laser-Compton scheme; energy of the Compton gamma rays, estimation of the luminosity, propagation of the laser beam and pulsed laser stacking in the optical cavities. Chapter 4 describes the design of the 3D 4-mirror cavity for the gamma ray generation experiment; advantages the 3D 4-mirror cavity, polarization dependence, general parameters of the cavity and feedback system. Chapter 5 investigates performance of the cavity; the finesse, stored power, laser beam profile and thermal effect in the cavity. Chapter 6 explains the gamma ray generation experiment; about the KEK-ATF, optical setup, gamma-rays detector and data acquisition system. Chapter 7 describes the results of the experiments; the number of gamma rays, and comparison of data measurement with a calculation. Chapter 8 is the conclusion of this thesis.

Chapter 2

International Linear Collider

2.1 The ILC

In July 2012, the evidence of a new particle with Higgs Boson-like properties was presented by the Large Hadron Collider (LHC) experiments at CERN [10, 11]. The particle is at a mass of 125 GeV. Precision measurements of properties are needed to identify the Higgs-like particle, and the International Linear Collider (ILC) would be an ideal instrument for that study. The ILC is a 31 km long linear electron-positron collider. It will explore the undiscovered phenomena in elementary particle physics and mysteries of the birth of the universe. It is designed as [12]:

- A continuous center-of-mass (CM) energy of 200–500 GeV (extendable to 1 TeV)
- A peak luminosity of $2 \times 10^{34}\,\mathrm{cm}^{-2}\,\mathrm{s}^{-1}$ at 500 GeV CM
- 80% electron polarization at the Interaction Point (IP)
- A relative energy stability and precision of $\leq 0.1\%$
- An option for 50 to 60% positron polarisation

The advantage of the ILC is high-precision measurement at TeV energy scale. The ILC experiments at the TeV scale are expected to solve the mysteries of elementary particle physics. For example, the origin of the symmetry breaking of the electroweak interactions, the nature of the dark matter in the universe, and the baryon-antibaryon asymmetry.

The ILC overview based on the Technical Design Report (TDR) is shown in Fig. 2.1. The primary parameters for 200, 250, 350 and 500 GeV CM operation are summarized in Table 2.1.

2.2 Significance of polarized positron beams

The polarized beam is a powerful tool for physics at the ILC. It enhances considerably signal rates and efficiently suppresses unwanted background processes [14].

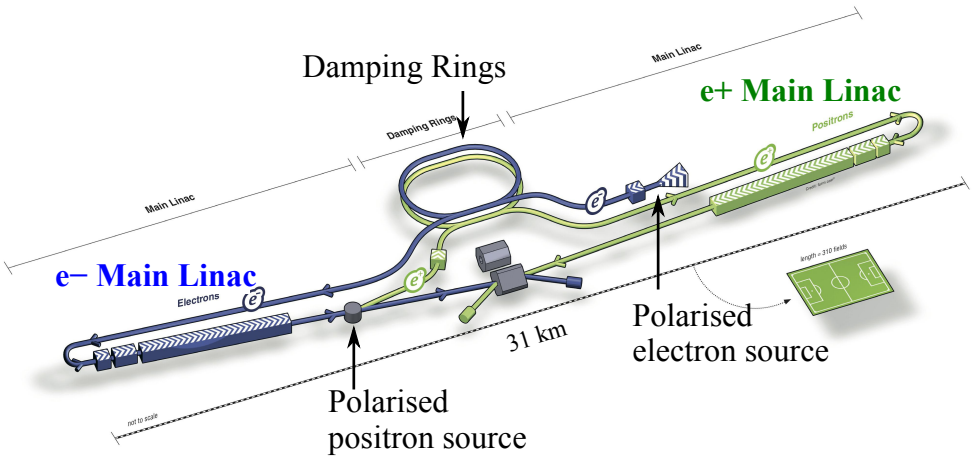

Figure 2.1: ILC overview [13].

Table 2.1: Summary of the 200–500 GeV baseline parameters for the ILC [12].

Center-of-mass energy	GeV	200	250	350	500
Bunch population	$\times 10^{10}$	2	2	2	2
Number of bunches		1312	1312	1312	1312
Linac bunch interval	ns	554	554	554	554
RMS bunch length	µm	300	300	300	300
Normalized H emittance at IP	µm	10	10	10	10
Normalized V emittance at IP	nm	35	35	35	35
RMS H beam size at IP	nm	904	729	684	474
RMS V beam size at IP	nm	7.8	7.7	5.9	5.9
Luminosity	$\times 10^{34}$ cm^{-2} s^{-1}	0.56	0.75	1.0	1.8

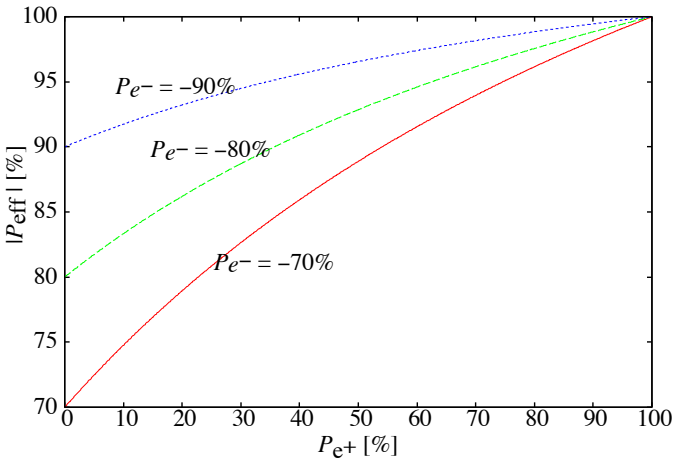

Figure 2.2: Effective polarization as a function of positron beam polarization.

The ILC is designed to provide the polarized electron beam using a DC gun equipped with a GaAs photocathode. The GaAs-GaAsP strained superlaticce layers photocatode provided the electron beam of 90% polarization with quantum efficiency of 0.5% [15]. In addition the polarized electron beam, it is desirable to use the polarized positron beam since it increases the effective polarization, which is defined as

$$P_{\mathbf{eff}} = \frac{P_{\mathbf{e}^-} - P_{\mathbf{e}^+}}{1 - P_{\mathbf{e}^+} P_{\mathbf{e}^-}} \tag{2.1}$$

where $P_{\mathbf{e}^-}$ is the polarization of the electron and $P_{\mathbf{e}^+}$ is the polarization of the positron. For example, 80% electron ($P_{\mathbf{e}^-} = 0.8$) and 60% positron polarization ($P_{\mathbf{e}^+} = -0.6$) yield the effective polarization of 95%. Fig. 2.2 shows the effective polarization as a function of positron beam polarization.

Polarized positrons are generated using polarized gamma rays. Polarized gamma rays are injected to a thin target and positrons are created via pair creation processes. At this time, positrons and electrons are polarized thanks to the helicity conservation in the QED interaction. When the gamma ray is left handed, the polarization of the electron and the positron is left handed in the high energy end of the positron.

2.3 Positron source for the ILC

The requirements for the positron source for the ILC are given in Table 2.2.

The baseline design of positron generation is the undulator scheme where the electron beams in the main linac beam travel through a long helical undulator and generate gamma rays. The gamma rays are impinged onto a thin metal target to generate positrons. In addition to the undulator-based scheme, two alternative positron sources, i.e. the conventional scheme and the laser-Compton scheme, are being developed. Both schemes have an advantage that the positron source is independent of the electron beam in the ILC main linac while the undulator scheme uses high energy the electron beams accelerated in the main linac.

Table 2.2: Nominal Positron Source Parameters [12].

Parameter	Value	Units
Positrons per bunch at IP	2×10^{10}	number
Bunches per pulse	1312	number
Pulse Repetition Rate	5	Hz

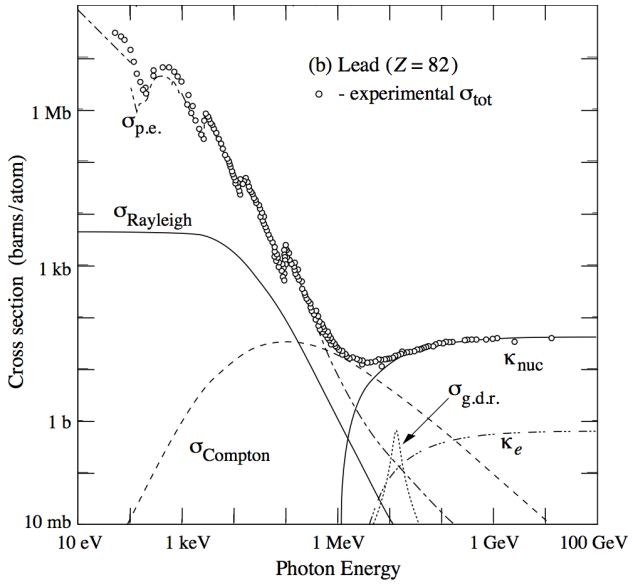

Figure 2.3: Photon total cross sections as a function of energy in lead [16].

2.3.1 Conventional scheme

Positron beams are generated via the pair-conversion of high-energy photons. In general, positrons for accelerators are generated via the electromagnetic shower in metal targets such as tungsten. In this scheme, a electron beam of a few GeV are impinged into the metal target and positrins generated via the electromagnetic shower are collected by a capture system consists of magnets and accelerating structure and sent to further acceleration systems. A disadvantage of the conventional scheme is that it is not capable to create the polarized positron beam.

2.3.2 Undulator scheme

The undulator scheme is the baseline design of the ILC. In this scheme, positrons are generated using gammma rays. Gamma rays are injected to the target made of titanium and positrons are created via pair creation processes. Fig. 2.3 shows total cross sections of photons lead. $\sigma_{p.e.}$ is the atomic photoelectric effect. k_{nuc} is the pair creation in the nuclear field. k_e is the pair creation in the electron field. In lead targets, the pair creation process is dominant above photon energy of $\sim 10\,\mathrm{MeV}$. Therefore, either the electron driven or the photon driven, photons of 10 MeV or more are required for effective generation of positrons in targets.

In the helical undulator, the incident electron moves spirally in the helical

Table 2.3: Parameters of ILC undulator [12].

Parameter	Value	Units
Undulator Period, λ_u	1.15	cm
Undulator Strength, K	0.92	
Undulator Type	Helical	
Undulator Length	147	m

coil. When an electron moves spirally by the magnetic field in an undulator, the fundamental energy of generated photon is [17];

$$E_1 = \frac{2\gamma^2 \hbar \omega_0}{1 + K^2} \tag{2.2}$$

where $\omega_0 = 2\pi\beta_z c/\lambda_u$, the circular frequency of the electron's helical orbit. K value of the undulator is defined as;

$$K = \frac{eB_0\lambda_u}{2\pi m_0 c} \tag{2.3}$$

Here λ_u is the undulator period. B_0 is the strength of magnetic field of center axis. ω_0 shows the orbital rotation angular frequency of the spiral motion.

The parameters of ILC undulator are given in Table 2.3. For $\lambda_u = 1.15\,\mathrm{cm}$, $K = 0.92$ and the electron beam energy $E_{\mathrm{beam}}(= m_0\gamma)$ of 150 GeV, the fundamental energy of photon beam, E_1, is 10.1 MeV. To provide gamma rays of O(10 MeV), the electron beams of more than 150 GeV must be fed into the undulator. It means that the undulator will be inserted in a part of the main linac of the ILC and will not be available until the completion of the linac.

2.3.3 Compton scheme

Another method to create gamma rays to generate positrons is the Compton scheme. Several configuration of the Compton scheme are studied to achieve the number of generation for ILC by laser-Compton scattering [18, 19]. One scheme is a Ring-Compton scheme. The Ring-Compton scheme uses a few GeV electron beam and laser stacking cavities in multiple laser–electron collision points to increase the photon intensity. Generated positrons are stored in a storage ring. Fig. 2.4 shows a schematic layout of the Ring-Compton scheme. One of the important issues with Ring-Compton scheme is a high-finesse laser-light stacking cavity. The scheme assume a cavity with enhancement factor of 10^4.

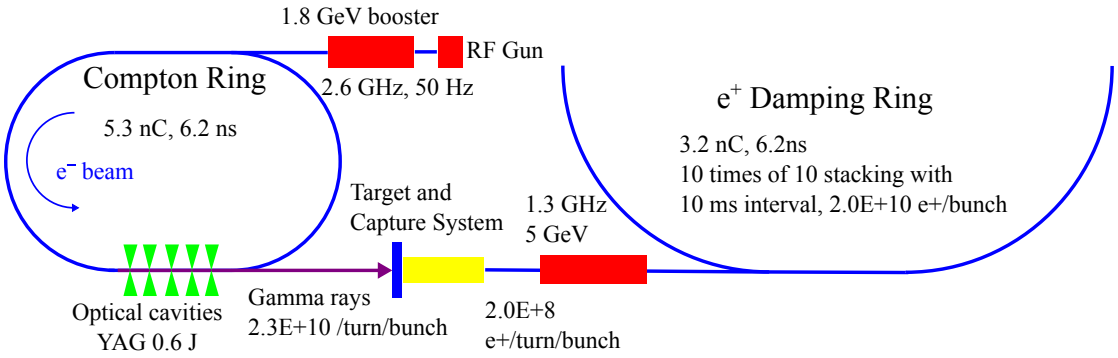

Figure 2.4: The conceptual design of the Ring-Compton scheme [20].

Chapter 3

Laser-Compton scattering using an optical cavity

3.1 Compton scattering

In laser-Compton scattering, energetic electrons undergo elastic collisions with low-energy laser photons and the electrons lose energy and the photons gain energy during the interaction [21]. In this section, we estimate the counting rate of high energy photons by laser-Compton scattering.

3.1.1 Energy of scattered photon

We now consider the laser-Compton scattering process in the electron-rest frame and the laboratory frame, as illustrated in Fig. 3.1. In the electron-rest frame, m_e is the electron rest mass, k_0^* is the energy of incident photon, k_s^* is the energy of the scattered photon, ϕ^* is the crossing angle, and θ^* is the scattering angle. From the relativistic kinematics, the energy of the scattered photon k_s^* is given by

$$k_s^* = \frac{m_e c^2 k_0^*}{m_e c^2 + k_0^*[1 - \cos(\phi^* - \theta^*)]} \tag{3.1}$$

where c is the light velocity.

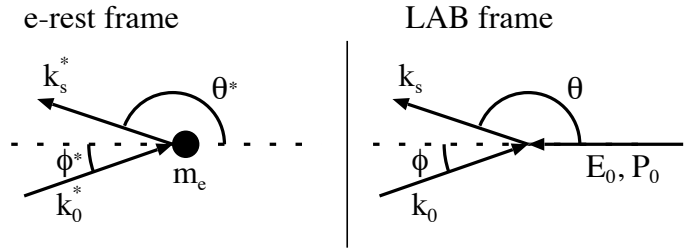

Figure 3.1: Schematics of Compton scattering in the electron-rest frame (left) and the laboratory frame (right).

Here, we consider the Lorentz transformation between the laboratory frame and the electron-rest frame which is characterized by the Lorentz factor

$$\gamma = \frac{E_0}{m_e} = \frac{1}{\sqrt{1-\beta^2}} \tag{3.2}$$

The kinematic variables in the electron-rest frame are given by

$$k_0^* = \gamma k_0(1 - \beta\cos\phi) \tag{3.3}$$

$$k_s^* = \gamma k_s(1 - \beta\cos\theta) \tag{3.4}$$

$$\sin\phi^* = \frac{\sin\phi}{\gamma(1-\beta\cos\phi)} \tag{3.5}$$

$$\cos\phi^* = \frac{-\beta + \cos\phi}{1-\beta\cos\phi} \tag{3.6}$$

$$\sin\theta^* = \frac{\sin\theta}{\gamma(1-\beta\cos\theta)} \tag{3.7}$$

$$\cos\theta^* = \frac{-\beta + \cos\theta}{1-\beta\cos\theta} \tag{3.8}$$

where k_0 is the energy of the incident photon, k_s is the energy of the scattered photon, ϕ is the crossing angle and θ is the scattered angle of the photon. The energy of scattered photon in the laboratory frame, is expressed as

$$k_s = \frac{E_0 k_0(1-\beta\cos\phi)}{E_0(1-\beta\cos\theta) + k_0[1-\cos(\phi-\theta)]} \tag{3.9}$$

Fig. 3.2 shows the calculated energy of scattered photons as a function of scattering angle. With current experimental condition of $E_0 = 1.28\,\mathrm{GeV}$, $k_0 = 1.165\,\mathrm{eV}$, $\phi = 14\,\mathrm{deg}$, the maximum photon energy is calculated to be 28.2 MeV at $\theta = \pi$, which is the direction of the electron beam.

3.1.2 Differential cross section

The differential cross section of Compton scattering in the electron-rest frame is given by Klein-Nishina formula [22]

$$\frac{d\sigma_C}{d\Omega^*} = \frac{r_0^2}{2}\left(\frac{k_s^*}{k_0^*}\right)^2\left[\frac{k_0^*}{k_s^*} + \frac{k_s^*}{k_0^*} - \sin^2(\theta^* - \phi^*)\right] \tag{3.10}$$

The expression can be converted to the laboratory frame as

$$\frac{d\sigma_C}{d\Omega} = \frac{d\sigma_C}{d\Omega^*}\frac{d\Omega^*}{d\Omega} = \frac{d\sigma_C}{d\Omega^*}\frac{\sin\theta^*}{\sin\theta}\frac{d\theta^*}{d\theta} \tag{3.11}$$

$$= \frac{d\sigma_C}{d\Omega^*}\frac{1}{\gamma^2(1-\beta\cos\theta)^2} \tag{3.12}$$

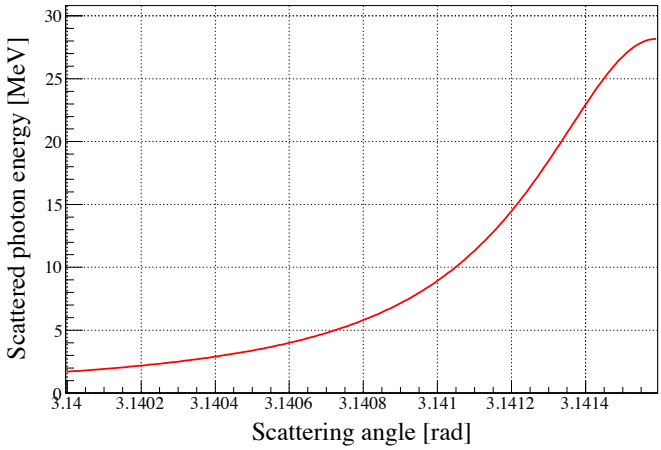

Figure 3.2: The energy of scattered photons as a function of scattering angle.

The integral of the differential cross section over $0 \leqq \theta \leqq \Theta$, with $d\Omega = 2\pi \sin\theta d\theta$, is

$$\sigma_C = \int_0^\Theta \frac{d\sigma_C}{d\Omega} 2\pi \sin\theta d\theta \tag{3.13}$$

The differential cross section with respect to the scattered photon energy is expressed as;

$$\frac{d\sigma_C}{dk_s} = \frac{d\sigma_C}{d\Omega}\frac{d\Omega}{dk_s} \tag{3.14}$$

$$= \frac{r_0^2}{2}\left(\frac{k_s^*}{k_0^*}\right)^2 \left[\frac{k_0^*}{k_s^*} + \frac{k_s^*}{k_0^*} - \sin^2(\theta^* - \phi^*)\right] \left(\frac{-2\pi}{\gamma^2(1-\beta\cos\theta)^2}\right) \frac{d\cos\theta}{dk_s} \tag{3.15}$$

Fig. 3.3 shows the differential cross section as a function of scattering angle. Most of photons are scattered in the forward direction of the electron beam ($\theta = \pi$). Fig. 3.4 shows the integrated cross section. Note that the aperture of the detector in the experiment is 0.26 mrad. Fig. 3.5 shows the differential cross section as a function of the scattered photon energy when helicities of laser photons are +1 (right-handed, R) [6]. The left-handed (L, helicity of −1) photons dominate in the energy close to the maximum energy of 28 MeV.

3.1.3 Estimation of the luminosity

The luminosity for Compton scattering is given by [23]

$$\mathscr{L} = \frac{f N_e N_l \cos(\phi/2)}{2\pi} \frac{1}{\sqrt{\sigma_{ye}^2 + \sigma_{yl}^2}\sqrt{(\sigma_{xe}^2 + \sigma_{xl}^2)\cos^2(\phi/2) + (\sigma_{ze}^2 + \sigma_{zl}^2)\sin^2(\phi/2)}} \tag{3.16}$$

where

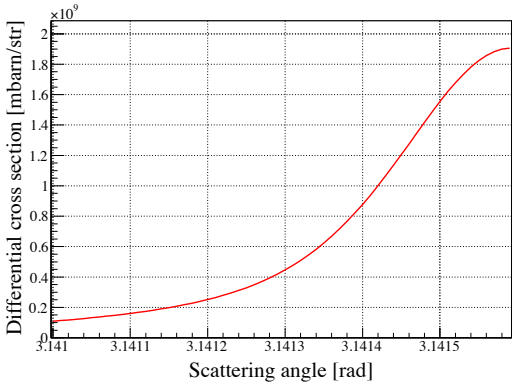

Figure 3.3: Differential cross section as a function of the scattering angle.

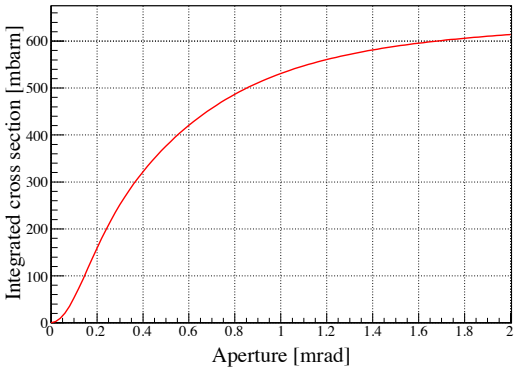

Figure 3.4: Integrated cross section within the aperture of the detector.

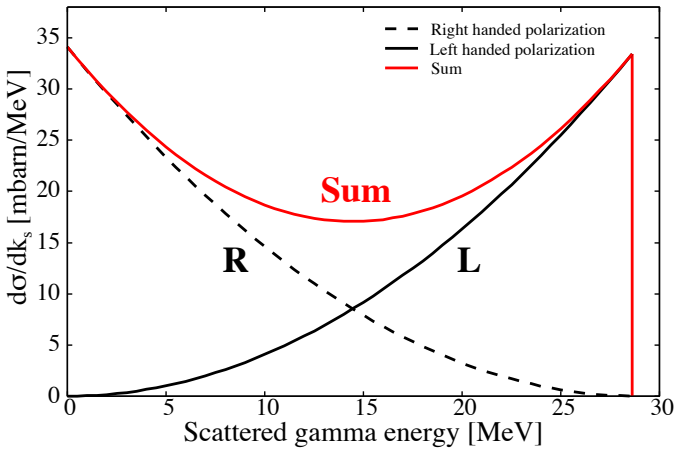

Figure 3.5: Differential cross section of the Compton scattering for right-handed polarized laser photons as a function of the scattered photon energy.

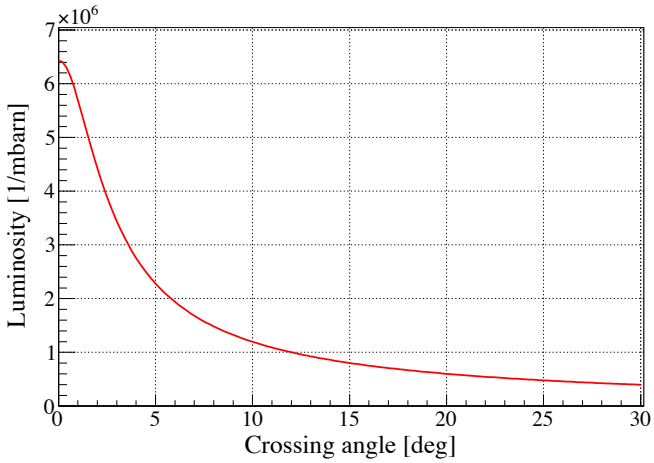

Figure 3.6: Crossing angle dependence on luminosity.

f: revolution frequency of the electron beam
N_e, N_l: number of particles in beam
ϕ: crossing angle

The number of events per unit time is expressed in the form

$$\frac{dN_\gamma}{dt} = \sigma_C \mathscr{L} \tag{3.17}$$

where σ_C is the total cross section. Fig. 3.6 shows a crossing angle dependence of the luminosity.

For the calculation, we used the following parameters

laser wave length: 1064 nm
laser power: 7 µJ / pulse
Integrated cross section (within the aperture of 0.26 mrad): 220 mbarn
electron beam intensity: 1.0×10^{10}

The expected counting rate is 1.9×10^8 photons per second.

3.2 Principle of laser beam

3.2.1 Gaussian beam

We consider the propagation of light which has transverse intensity distribution like;

$$f(x) = A \exp\left(-\frac{x^2}{2\sigma^2}\right) \tag{3.18}$$

The wave equation for the electric field in vacuum is;

$$\nabla^2 E(\boldsymbol{r}, t) = \frac{1}{c^2}\frac{\partial^2}{\partial t^2} E(\boldsymbol{r}, t) \tag{3.19}$$

A solution of Eq. (3.19) can be expressed by a form of variable separation as;

$$E(\boldsymbol{r}, t) = \mathcal{E}(\boldsymbol{r})e^{i\omega t} \tag{3.20}$$

The spatial part of the solution, $\mathcal{E}(\boldsymbol{r})$, satisfies Helmholtz equation;

$$\nabla^2\mathcal{E}(\boldsymbol{r}) + k^2\mathcal{E}(\boldsymbol{r}) = 0 \tag{3.21}$$

where

$$k^2 = \frac{\omega^2}{c^2} \tag{3.22}$$

A solution of of Eq. (3.21) propagating in z direction is expressed as;

$$\mathcal{E}(\boldsymbol{r}) = \mathcal{E}_0(\boldsymbol{r})e^{-ikz} \tag{3.23}$$

Since Eq. (3.23) must satisfy the Helmholtz equation;

$$\left(\frac{\partial^2}{\partial x^2} + \frac{\partial^2}{\partial y^2} + \frac{\partial^2}{\partial z^2}\right)\mathcal{E}_0(\boldsymbol{r})e^{-ikz} + k^2\mathcal{E}_0(\boldsymbol{r})e^{-ikz} = 0 \tag{3.24}$$

Eq. (3.24) can be rearranged as;

$$\left(\nabla_T^2 + \frac{\partial^2}{\partial z^2}\right)\mathcal{E}_0(\boldsymbol{r}) - 2ik\frac{\partial\mathcal{E}_0}{\partial z} = 0 \tag{3.25}$$

Here ∇_T^2 is;

$$\nabla_T^2 \equiv \frac{\partial^2}{\partial x^2} + \frac{\partial^2}{\partial y^2} \tag{3.26}$$

When the electric field changes slowly for the propagation direction and satisfy condition such that;

$$\lambda\left|\frac{\partial\mathcal{E}_0}{\partial z}\right| \ll |\mathcal{E}_0|, \quad \lambda\left|\frac{\partial^2\mathcal{E}_0}{\partial z^2}\right| \ll \left|\frac{\partial\mathcal{E}_0}{\partial z}\right| \tag{3.27}$$

Eq. (3.25) can be approximated in the form of paraxial ray equation

$$\left(\nabla_T^2 - 2ik\frac{\partial}{\partial z}\right)\mathcal{E}_0(\boldsymbol{r}) = 0 \tag{3.28}$$

and its solution is called the paraxial ray.

Putting a solution of Eq. (3.28) having the form;

$$\mathcal{E}_0(\boldsymbol{r}) = Ae^{-ip(z)}e^{-ik(x^2+y^2)/2q(z)} \tag{3.29}$$

Eq. (3.28) is written;

$$\begin{aligned}\nabla_T^2\mathcal{E}_0 - 2ik\frac{\partial\mathcal{E}_0}{\partial z} &= A\left[\frac{k^2}{q^2}(x^2+y^2)\left(\frac{\partial q}{\partial z} - 1\right) - 2k\left(\frac{\partial p}{\partial z} - \frac{i}{q}\right)\right]e^{-i\frac{k(x^2+y^2)}{2q(z)}}e^{-ip(z)} \\ &= 0\end{aligned} \tag{3.30}$$

In order to satisfy Eq. (3.30),

$$\frac{\partial q}{\partial z} = 1 \tag{3.31}$$

$$\frac{\partial p}{\partial z} = -\frac{i}{q} \tag{3.32}$$

A solution of Eq. (3.31) and (3.32) are;

$$q(z) = q_0 + z \tag{3.33}$$

$$p(z) = -i \ln \frac{q_0 + z}{q_0} \tag{3.34}$$

where $q_0 = q(0)$ and we assume $p(0) = 0$.

Because of the exponential part of Eq. (3.29) is similar to Gaussian distribution, let transverse distribution of intensity of Eq. (3.29) be;

$$I(\boldsymbol{r}) = |\mathcal{E}(\boldsymbol{r})|^2 \propto e^{-2\frac{x^2+y^2}{w^2(z)}} \tag{3.35}$$

w is the spot size of the laser beam. In general, q is imaginary and q_0 should be pure imaginary number at $z = 0$ so that Eq. (3.29) may satisfy Eq. (3.36).

$$\frac{1}{q_0} = -\frac{2i}{kw_0^2} = -\frac{i\lambda}{\pi w_0^2} \tag{3.36}$$

where

$$k = \frac{2\pi}{\lambda}, \quad w(0) = w_0 \tag{3.37}$$

When we substitute Eq. (3.34) and Eq. (3.36) for Eq. (3.29) as follows;

$$\mathcal{E}_0(\boldsymbol{r}) = A \exp\left[-\ln\left(1 + \frac{z}{q_0}\right)\right] \exp\left(-i\frac{k(x^2+y^2)}{2(q_0+z)}\right) \tag{3.38}$$

$$= A \exp\left[-\ln\left(1 - \frac{i\lambda z}{\pi w_0^2}\right)\right] \exp\left(-ik\frac{x^2+y^2}{2\left(\frac{\pi w_0^2}{i\lambda} + z\right)}\right) \tag{3.39}$$

$$= A\frac{1}{\sqrt{1+\frac{\lambda^2 z^2}{\pi^2 w_0^2}}} \exp\left\{\left[i \tan^{-1}\left(\frac{\lambda z}{\pi w_0^2}\right)\right]\right\} \times \exp\left\{-\frac{x^2+y^2}{w_0^2[1+(\frac{\lambda z}{\pi w_0^2})^2]} - \frac{ik(x^2+y^2)}{2z[1+(\frac{\pi w_0^2}{\lambda z})^2]}\right\} \tag{3.40}$$

$w^2(z)$, $R(z)$, $\psi(z)$ and z_R are calculated as;

$$w(z) = w_0 \left[1 + \left(\frac{\lambda z}{\pi w_0^2}\right)^2\right]^{\frac{1}{2}} = w_0\sqrt{1 + \left(\frac{z}{z_R}\right)^2} \tag{3.41}$$

$$R(z) = z\left[1 + \left(\frac{\pi w_0^2}{\lambda z}\right)^2\right] = z\left(1 + \frac{z_R^2}{z^2}\right) \tag{3.42}$$

$$\psi(z) = \tan^{-1}\left(\frac{\lambda z}{\pi w_0^2}\right) = \tan^{-1}\left(\frac{z}{z_R}\right) \tag{3.43}$$

$$z_R \equiv \frac{\pi w_0^2}{\lambda} \tag{3.44}$$

Finally, the electromagnetic field with Gaussian shape transverse profile in the form of Eq. (3.20) can be written as;

$$\begin{aligned} E(x,y,z,t) &= A\frac{w_0}{w(z)}e^{i\omega t}\exp\left[-i(kz - \psi(z)) - i\frac{k(x^2+y^2)}{2q(z)}\right] \\ &= A\frac{w_0}{w(z)}e^{i\omega t}\exp\left[-i(kz - \psi(z)) - (x^2+y^2)\left(\frac{1}{w^2(z)} + \frac{ik}{2R(z)}\right)\right] \end{aligned} \tag{3.45}$$

Eq. (3.45) shows the fundamental Gaussian beam. In general, the solution for Gaussian beam is written in the form of Hermite-Gaussian mode as;

$$\mathcal{E}_{l,m}(x,y,z) = \mathcal{E}_0\frac{w_0}{w(z)}H_l\left(\sqrt{2}\frac{x}{w(z)}\right)H_m\left(\sqrt{2}\frac{y}{w(z)}\right) \tag{3.46}$$

$$\times \exp\left[-ik\frac{x^2+y^2}{2q(z)} - ikz + i(l+m+1)\psi\right] \tag{3.47}$$

$$= \mathcal{E}_0\frac{w_0}{w(z)}H_l\left(\sqrt{2}\frac{x}{w(z)}\right)H_m\left(\sqrt{2}\frac{y}{w(z)}\right) \tag{3.48}$$

$$\times \exp\left[-\frac{x^2+y^2}{w^2(z)} - ik\frac{x^2+y^2}{2R(z)} - ikz + i(l+m+1)\psi\right] \tag{3.49}$$

where H_l and H_m are Hermite polynomial of l_{th} and m_{th} and the higher mode Gaussian beam with l and m are written as TEM_{lm} (Transverse Electro-Magnetic). Transverse profiles of Hermite-Gaussian mode are shown in Fig. 3.7.

$w(z)$ and $R(z)$ are the spot size and the curvature radius of the equiphase surface at z. Gouy phase, $\psi(z)$, is an additional phase shift of the wave when it passes through the focal point as plotted in Fig. 3.8. z_R, named as Rayleigh range, is a region where the beam is focused around its focal point. The spot size $w(z)$ in the far field coming from a waist is given by

$$w(z) \approx \frac{w_0 z}{z_R} = \frac{\lambda z}{\pi w_0} \quad (z \gg z_R) \tag{3.50}$$

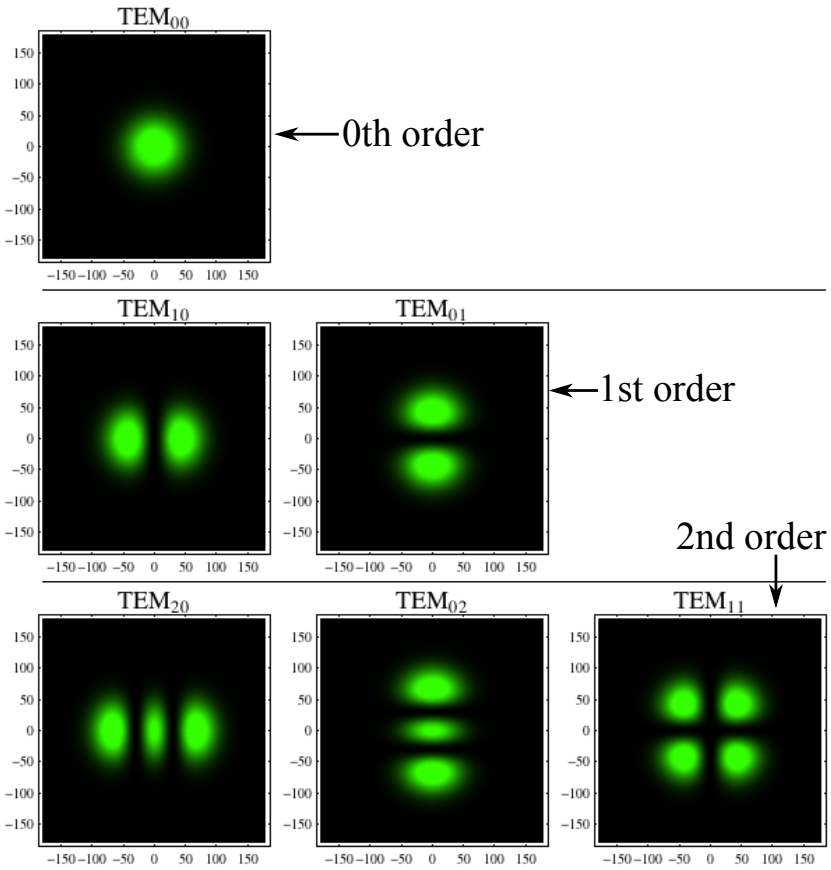

Figure 3.7: Transverse profile of several modes. TEM_{00} is the fundamental mode. These TEM_{mn} modes are classified according to the order $(m+n)$.

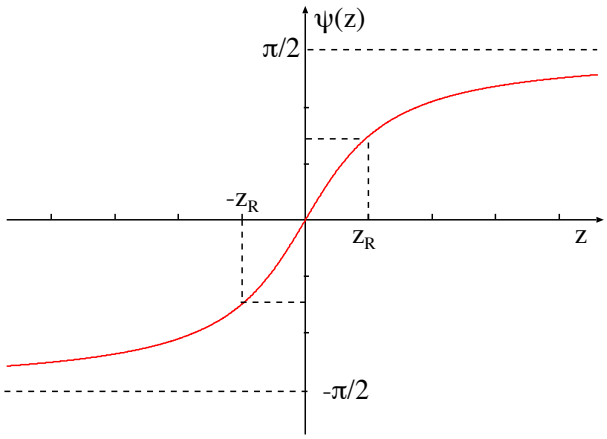

Figure 3.8: Gouy phase shift through the waist region of a Gaussian beam.

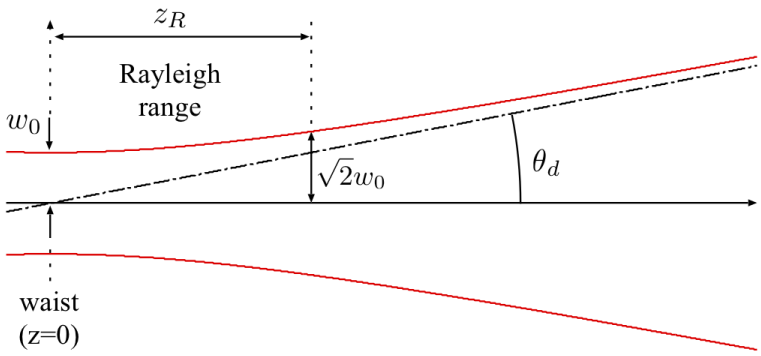

Figure 3.9: A laser beam spreads away from its waist.

In the far field, $w(z)$ increases linearly with z, and the angle of a beam divergence θ_d, as shown in Fig. 3.9, by

$$\theta_d = \frac{\lambda}{\pi w_0} \tag{3.51}$$

$R(z)$ and $w(z)$ at any plane z are derived from the $q(z)$ by the definition that

$$\frac{1}{q(z)} = \frac{1}{R(z)} - i\frac{\lambda}{\pi w^2(z)} \tag{3.52}$$

Here after, $q(z)$ is referred as Gaussian beam parameter.

3.2.2 ABCD law

Optical rays

Propagation of light can be described by a transverse displacement $r(z)$ and a slope $r'(z) = dr/dz$ where z is the axis of propagation and r is the transverse coordinate. The $r'(z) = \tan\theta \approx \sin\theta \approx \theta$ when the slope is small.

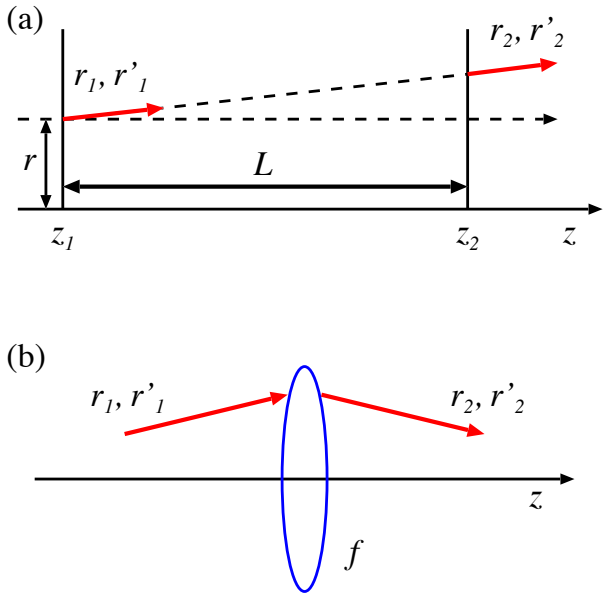

Figure 3.10: Optical ray transformation.

If a ray propagates in free space from z_1 to $z_2 = z_1 + L$, as shown in Fig. 3.10(a), transfer of the ray from z_1 to z_2 is described as [24];

$$r(z_2) = r(z_1) + L dr(z_1)/dz \tag{3.53}$$
$$dr(z_2)/dz = dr(z_1)/dz \tag{3.54}$$

Suppose the ray passes through a thin lens with a focal length of f as shown in Fig. 3.10(b).

$$r(z_2) = r(z_1) \tag{3.55}$$
$$dr(z_2)/dz = -(1/f)r(z_1) + dr(z_1)/dz \tag{3.56}$$

In general, transformation of an optical ray passing through optical elements can be written in the form as

$$\boldsymbol{r_2} \equiv \begin{pmatrix} r_2 \\ r_2' \end{pmatrix} = \begin{pmatrix} A & B \\ C & D \end{pmatrix} \times \begin{pmatrix} r_1 \\ r_1' \end{pmatrix} \equiv M\boldsymbol{r_1} \tag{3.57}$$

where M is a ray matrix, or an ABCD matrix, for the optical element. The ray matrices for typical optical elements are summarized in Table 3.1.

The ABCD low for Gaussian beam

The propagation of Gaussian beam is also described by the ABCD matrix.

When Gaussian beam with the beam parameter q_1 (see Eq. (3.52)) passing through an optical element of $\begin{pmatrix} A_1 & B_1 \\ C_1 & D_1 \end{pmatrix}$, the beam parameter q_1, becomes q_2 as;

$$q_2 = \frac{A_1 q_1 + B_1}{C_1 q_1 + D_1} \tag{3.58}$$

Table 3.1: Ray matrices for each optical elements [25].

(a) "Free space" region, length L

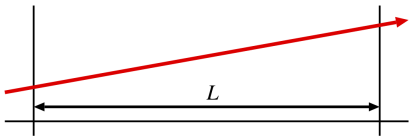

$$\begin{pmatrix} 1 & L \\ 0 & 1 \end{pmatrix}$$

(b) Thin lens, focal length f
$f > 0$ for converging lens

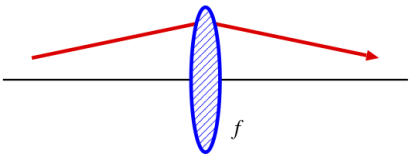

$$\begin{pmatrix} 1 & 0 \\ -1/f & 1 \end{pmatrix}$$

(c) Curved mirror, radius ρ
ρ > 0 for concave mirror

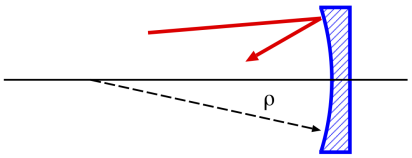

$$\begin{pmatrix} 1 & 0 \\ -2/\rho & 1 \end{pmatrix}$$

(d) Curved dielectric interface
ρ > 0 for concave surface

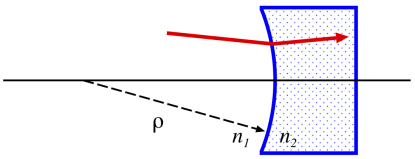

$$\begin{pmatrix} 1 & 0 \\ \frac{n_2 - n_1}{n_2 \rho} & \frac{n_1}{n_2} \end{pmatrix}$$

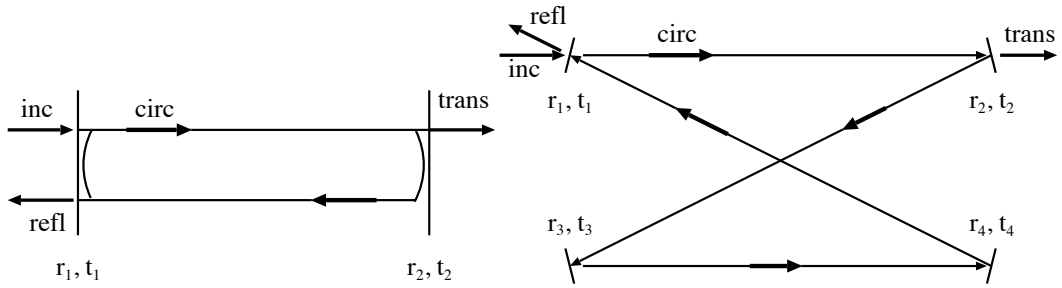

Figure 3.11: Stored power.

Since the transfer matrices are multiplicative, a Gaussian beam parameter q passing through multiple optical elements can be;

$$q_3 = \frac{A_2 q_2 + B_2}{C_2 q_2 + D_2} = \frac{A_3 q_1 + B_3}{C_3 q_1 + D_3} \tag{3.59}$$

where $\begin{pmatrix} A_3 & B_3 \\ C_3 & D_3 \end{pmatrix}$ is;

$$\begin{pmatrix} A_3 & B_3 \\ C_3 & D_3 \end{pmatrix} = \begin{pmatrix} A_2 & B_2 \\ C_2 & D_2 \end{pmatrix} \begin{pmatrix} A_1 & B_1 \\ C_1 & D_1 \end{pmatrix} \tag{3.60}$$

Thus, the beam parameters passing through optical elements are calculated with the ABCD law and is used for the design of the optical setup for the experiments.

3.3 Principle of an optical cavity

3.3.1 Principle of power enhancement

Here, we describe power enhancement by an optical cavity. The power reflectance, R, and the power transmittance, T, of a mirror are defined as the ratio of the reflected or transmitted power to those of the incident laser beam. The amplitude reflectance and transmittance are defined as $r = \sqrt{R}$ and $t = \sqrt{T}$, respectively.

When a laser beam is injected into the optical cavity, a part of the beam enters into the cavity through the coupling mirror as schematically illustrated in Fig. 3.11. The amplitude transmittance, t_{cav}, amplitude reflectance, r_{cav}, and amplitude of

the waves inside the cavity, $s_{\rm cav}$, are the sum of all waves;

$$t_{\rm cav} = \frac{E_{\rm trans}}{E_{\rm inc}} = t_1 t_2[1 + r_1 r_2 (r_3 r_4) e^{i\theta} + (r_1 r_2 (r_3 r_4) e^{i\theta})^2 + \cdots] = \frac{t_1 t_2}{1 - r_1 r_2 (r_3 r_4) e^{i\theta}} \tag{3.61}$$

$$r_{\rm cav} = \frac{E_{\rm refl}}{E_{\rm inc}} = r_1 - t_1 r_2 (r_3 r_4) t_1 e^{i\theta}[1 + r_1 r_2 (r_3 r_4) e^{i\theta} + (r_1 r_2 (r_3 r_4) e^{i\theta})^2 + \cdots] = r_1 - \frac{t_1 r_2 (r_3 r_4) t_1 e^{i\theta}}{1 - r_1 r_2 (r_3 r_4) e^{i\theta}} \tag{3.62}$$

$$s_{\rm cav} = \frac{E_{\rm circ}}{E_{\rm inc}} = t_1[1 + r_1 r_2 (r_3 r_4) e^{i\theta} + (r_1 r_2 (r_3 r_4) e^{i\theta})^2 + \cdots] = \frac{t_1}{1 - r_1 r_2 (r_3 r_4) e^{i\theta}} \tag{3.63}$$

where θ is the phase advance during one round trip inside the cavity. t_i and r_i are the amplitude transmittance and reflectance of the mirror M_i.

The power transmittance, the power reflectance and the power enhancement factor of the cavity ($T_{\rm cav}$, $R_{\rm cav}$ and $S_{\rm cav}$, respectively) are obtained by squaring amplitudes as;

$$T_{\rm cav} = |t_{\rm cav}|^2 = \frac{T_1 T_2}{(1-R)^2 + 4R \sin^2 \frac{\theta}{2}} \tag{3.64}$$

$$R_{\rm cav} = |r_{\rm cav}|^2 = (R_1 + T_1) - \frac{T_1 (1 - R^2 - T_1 \frac{R^2}{R_1})}{(1-R)^2 + 4R \sin^2 \frac{\theta}{2}} \tag{3.65}$$

$$S_{\rm cav} = |s_{\rm cav}|^2 = \frac{T_1}{(1-R)^2 + 4R \sin^2 \frac{\theta}{2}} \tag{3.66}$$

where R is the effective reflectivity;

$$R = \begin{cases} \sqrt{R_1 R_2} & \text{(2-mirror cavity)} \\ \sqrt{R_1 R_2 R_3 R_4} & \text{(4-mirror cavity)} \end{cases} \tag{3.67}$$

The phase advance in one round trip, θ ($= 2\pi \frac{L}{\lambda}$), depends on the optical path length and the wavelength of the laser beam. θ dependence of intensity of the transmitted light is shown in Fig. 3.12, it becomes larger only when $\theta = 2n\pi$ (n:integer), and it is said the cavity is in resonance.

On resonance,

$$T_{\rm cav} = \frac{T_1 T_2}{(1-R)^2} \tag{3.68}$$

$$R_{\rm cav} = (R_1 + T_1) - \frac{T_1 (1 - R^2 - T_1 \frac{R^2}{R_1})}{(1-R)^2} \tag{3.69}$$

$$S_{\rm cav} = \frac{T_1}{(1-R)^2} \tag{3.70}$$

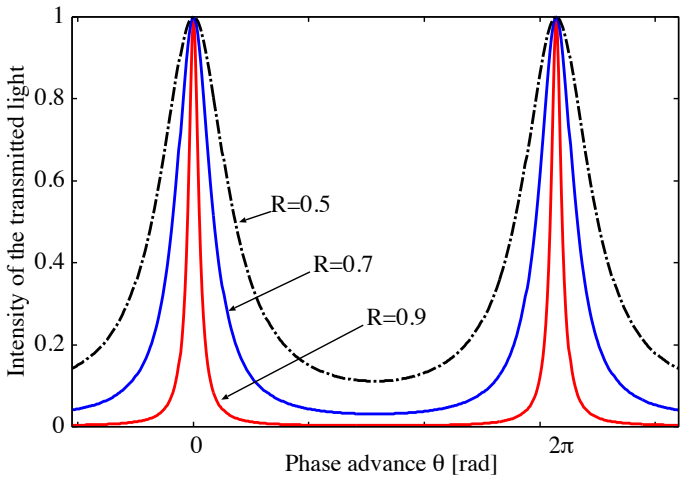

Figure 3.12: Airy function.

The intensity of the transmitted light as a function of the phase is called the Airy function. The FWHM of the peak of the Airy function is given by

$$\delta\theta = \frac{2(1-R)}{\sqrt{R}} \tag{3.71}$$

The separation of resonances, which corresponds to 2π phase advance, is called Free Spectral Range (FSR) in the frequency domain and denoted by $\Delta\nu$. It is determined by the total optical length L;

$$\Delta\nu = \frac{c}{L} \tag{3.72}$$

where c is the speed of light. The FWHM of Airy function is given by $\delta\theta$ in the phase; the corresponding quantity in the frequency domain is denoted by $\delta\nu$ and is given by $\delta\nu = (c/2\pi L)\delta\theta$. An important parameter of cavity called finesse, $\mathcal{F}$, is defined as the ratio of $\delta\nu$ and $\Delta\nu$;

$$\mathcal{F} \equiv \frac{\Delta\nu}{\delta\nu} = \frac{\pi\sqrt{R}}{1-R} \tag{3.73}$$

3.3.2 Resonance of a Gaussian beam in an optical cavity

Because of the Gouy phase shift (ψ: in Eq.3.43), the resonance condition discussed in previous section needs to be modified in the case of the Gaussian beam. The phase advance in the one round-trip should be an integer multiple of 2π to satisfy the resonance condition. The Gouy phase depends both on the order of the transverse mode $(l+m)$ and the beam waist (w_0). Hence, various transverse resonances may be realized at different cavity length depending on the order of the mode. If we measure the transmitted light from the cavity when scanning the its length, we observe various modes with different orders at different cavity lengths. It is illustrated in Fig. 3.13.

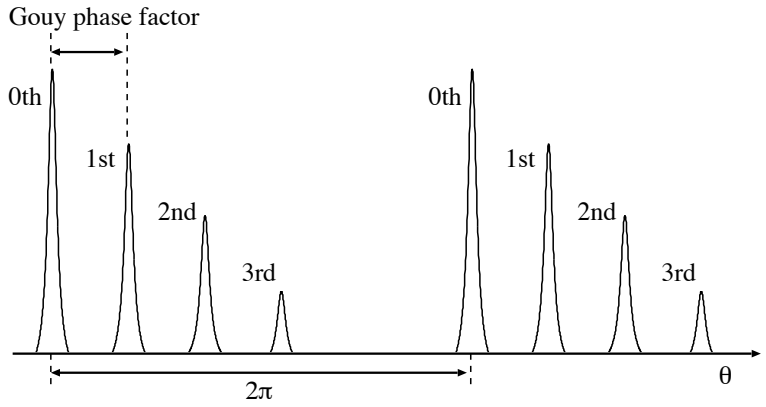

Figure 3.13: Resonance peaks of various transverse modes. The cavity length which satisfies the resonance condition depends on the order $(l+m)$ of the modes. These peaks can be observed when scanning the length of the cavity.

3.3.3 Pulse stacking to the optical cavity

Because the electron beam from accelerators has bunch structure, it is more efficient to use the pulsed laser for increasing the laser intensity that contributes to the collision with the electrons.

Mode-locked pulse laser

A mode-locked pulsed laser oscillator is adopted as a seed laser for the pulse stacking cavity. Inside the mode-locked oscillator, a optical resonant cavity is equipped to generated sequence of laser pulses. There are many longitudinal modes in the oscillator cavity, provided that a gain bandwidth of the laser medium is wider than the separation of the resonance condition. The electric field, $E(t)$, in the laser oscillator cavity is written as;

$$E(t) = \sum_m E_m e^{i[(\omega_0 + m\Delta\omega)t + \phi_m]} \tag{3.74}$$

Separation of the angular frequency $\Delta\omega$ is defined to be;

$$\Delta\omega \equiv \omega_{n+1} - \omega_n = \frac{\pi c}{L_{laser}} \tag{3.75}$$

here L_{laser} is the cavity length in the oscillator. For simplicity E_m, ϕ_m are assumed to be a constant and independent of m. If N modes are excited in the oscillator cavity, Eq. (3.74) is written as;

$$\begin{aligned} E(t) &= NEe^{i(\omega_0 t+\phi)} \sum_{-(N-1)/2}^{(N-1)/2} e^{im\Delta\omega t} \\ &= NEe^{i(\omega_0 t+\phi)} \frac{\sin\left(N\Delta\omega t/2\right)}{\sin\left(\Delta\omega t/2\right)} \end{aligned} \tag{3.76}$$

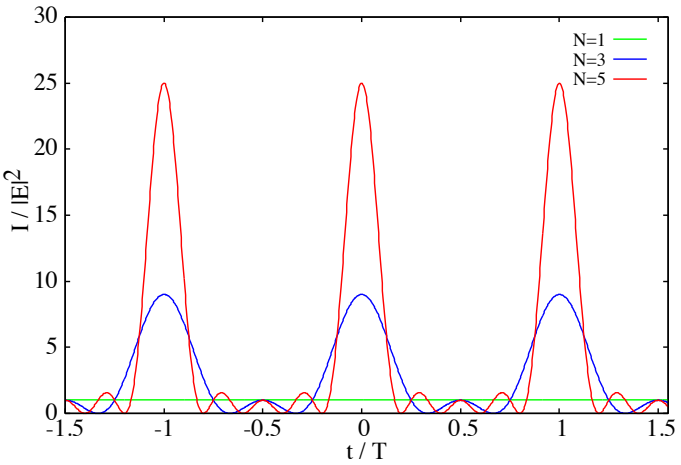

Figure 3.14: Time dependence of laser pulse intensity of mode locked laser. $T \equiv 2L_{\text{laser}}/c$

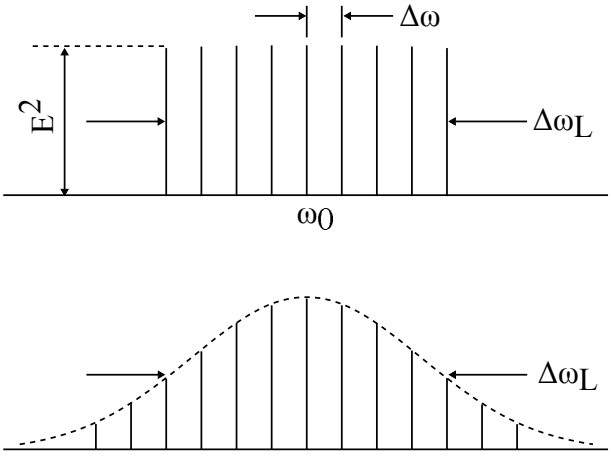

Figure 3.15: Mode amplitudes as a function of frequency for a mode-locked laser.

The intensity of laser beam $I(t)$ is;

$$I(t) = E(t)E^*(t) \propto \frac{\sin^2(N\Delta\omega t/2)}{\sin^2(\Delta\omega t/2)} \tag{3.77}$$

The temporal profile of the laser $I(t)$ is a pulsed shape as shown in Fig. 3.14. The peak intensity the pulse is proportional to N^2.

The spectral envelope is expected to have a bell-shaped form as Fig. 3.15. $\Delta\omega_L$ is the bandwidth (FWHM). The duration of each pulse of the output beam is about equal to the inverse of the oscillation bandwidth $\Delta\omega_L$.

Pulse stacking

In general, the optical resonant cavities must satisfy conditions for the cavity length L_{cav} as;

$$L_{\text{cav}} = n\frac{\lambda}{2} \quad (n\text{: integer}) \tag{3.78}$$

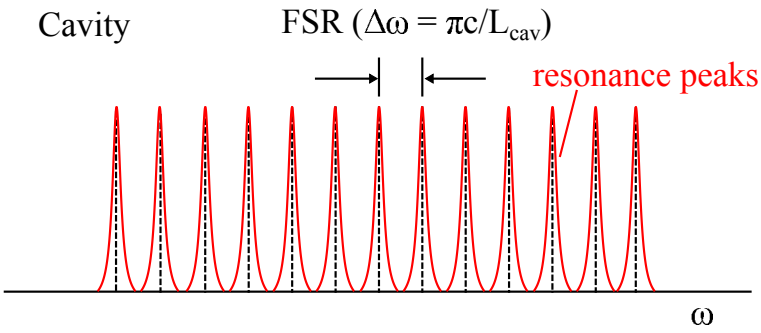

Figure 3.16: The resonance condition of the optical cavity in the frequency domain.

where round-trip optical path length $L_{\rm tot} = 2L_{\rm cav}$, n and λ are an arbitrary integer and the wave length of the laser respectively. An additional condition between the pulse stacking cavity and the cavity in the laser oscillator is required

$$L_{\rm cav} = mL_{\rm laser} \quad (m\,\text{: integer}) \tag{3.79}$$

to ensure all frequency component from the laser are resonated in the optical cavity. The resonance conditions for optical resonant cavity is illustrated in Fig. 3.16. The width of each resonance peaks depends on finesse of the optical cavity. When the mode separation of the laser $\Delta\omega$ is matched with FSR of the optical cavity, all longitudinal modes can be resonant in the cavity.

The intensity of transmitted light from the optical cavity as a function of the cavity length $L_{\rm cav}$ for finesse F =300, 4000, 10000 and 30000 is shown in Fig. 3.17. When the finesse increases, the difference of intensity between peak at center and next one becomes large. For $F = 10000$, the difference is about 50%.

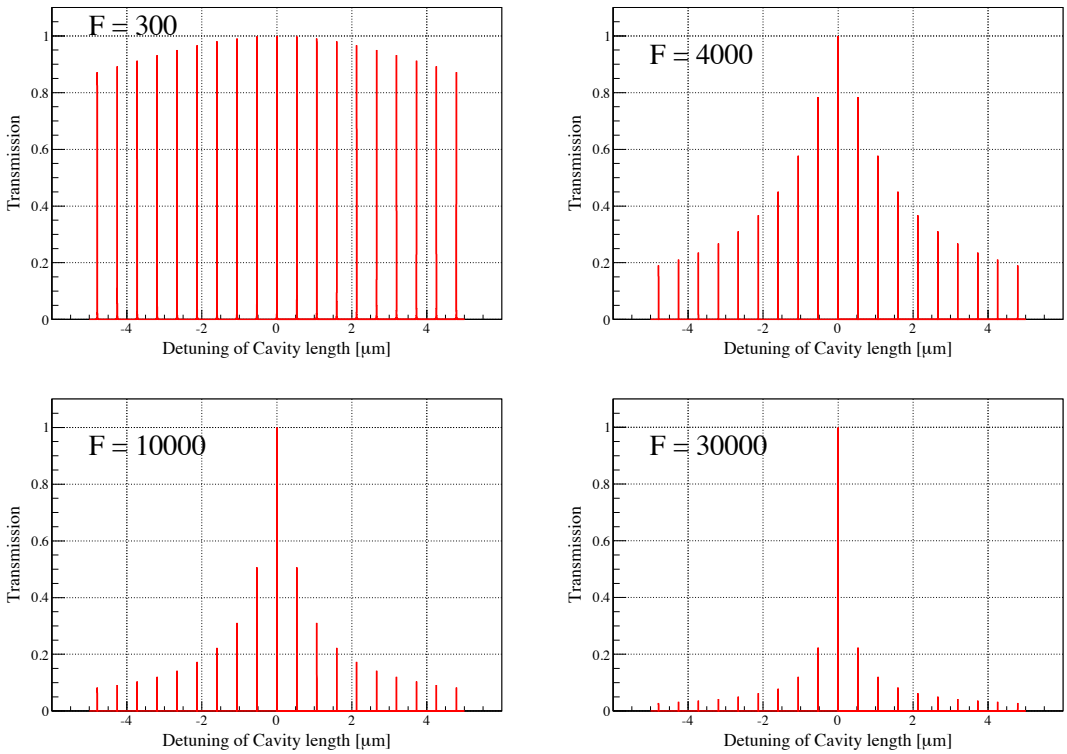

Figure 3.17: Transmitted power as a function of the cavity length.

Chapter 4

3D 4-mirror cavity

4.1 Property of the 3D 4-mirror cavity

4.1.1 Configuration of the cavity

The length of the round-trip optical path L of the resonant cavity must satisfy the relation $L = n\lambda$, where n and λ are an arbitrary integer and the wave length of the laser, respectively. To reduce the laser beam waist in a 2-mirror Fabry-Perot cavity, it has to be a concentric type, i.e., the curvature radius of mirrors, ρ, must be as close as to the half of the distance between the mirrors, D. The result is that the 2-mirror cavity is unstable against the misalignment of mirrors as illustrated in Fig.4.1(a) and (c). In a 4-mirror cavity consisting of two plane mirrors and two concave mirrors, it is possible to configure mirrors such that virtually parallel laser beams can be incident upon concave mirrors (see Fig. 4.1(b) and (d)). Thus one can get smaller beam waist in the 4-mirror cavity with confocal optics ($\rho \sim D$), which is more tolerant of misalignment of mirrors than concentric optics.

In the case of a planar 4-mirror cavity, where all 4 mirrors of the 4-mirror cavity are placed in the same plane (the tangential plane), the effective focal length in the plane f_t, and in the plane perpendicular to the tangential plane (the sagittal plane) f_s, is different (see Fig. 4.2(a)) [26]. This causes astigmatism at the focal point between the two concave mirrors:

$$f_t = \frac{\rho}{2}\cos\alpha \tag{4.1}$$

$$f_s = \frac{\rho}{2\cos\alpha} \tag{4.2}$$

Because of the astigmatism, the laser beam profile inside the planar 4-mirror cavity is an ellipse and is not suitable for maximizing the laser-Compton scattering efficiency.

A solution to avoid the astigmatism is to make f_t and f_s equal by twisting the optical path in the cavity, i.e., making a 3D 4-mirror cavity. Fig. 4.2 shows a schematic of a planar and a 3D cavity. Calculated waist sizes of the laser beam around the laser–electron interaction point for a planar and for a 3D 4-mirror cavity are shown in Fig. 4.3(a) and (b), respectively. In the calculation, it is assumed

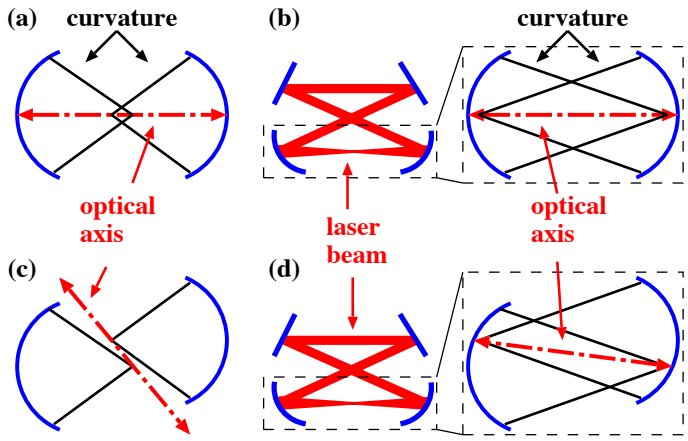

Figure 4.1: The illustration of optical configuration of 2 mirror and 4 mirror cavities. The concentric configuration for the 2 mirror case (a) and confocal configuration (b). The effects of misalignment for 2 mirror case (c) and 4 mirror case (d).

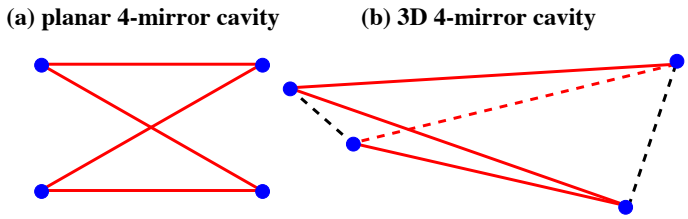

Figure 4.2: The schematic of mirror configuration for planar (a) and 3D 4-mirror (b) cavities.

that the distance between concave mirrors is the same for both configuration. In a 3D 4-mirror cavity, laser beam profile is rounder at the laser–electron interaction point compared to a planar cavity. Therefore we adopted Fig. 4.3(b) configuration. Details of the design and the laser beam profile in the 3D 4-mirror cavity are described in Section 4.2. The general discussion on stability of various four-mirror cavities is found in Ref. [9].

4.1.2 Polarization dependence

Since the laser light travels a twisted path in the 3D 4-mirror cavity, the optical state in the cavity acquires geometric phase during the propagation. This causes a rotation of the polarization axis for linearly polarized states or an additional phase for circularly polarized states. Fig. 4.4 shows the geometric phase caused by reflection at mirror M_{i-1} and M_i [27]. Let $\vec{n}_i$ be normal vector to the mirror M_i. The vector $\vec{a}_i$ can be defined as

$$\vec{a}_i = \frac{\vec{n}_i \times \vec{k}_i}{|\vec{n}_i \times \vec{k}_i|} \tag{4.3}$$

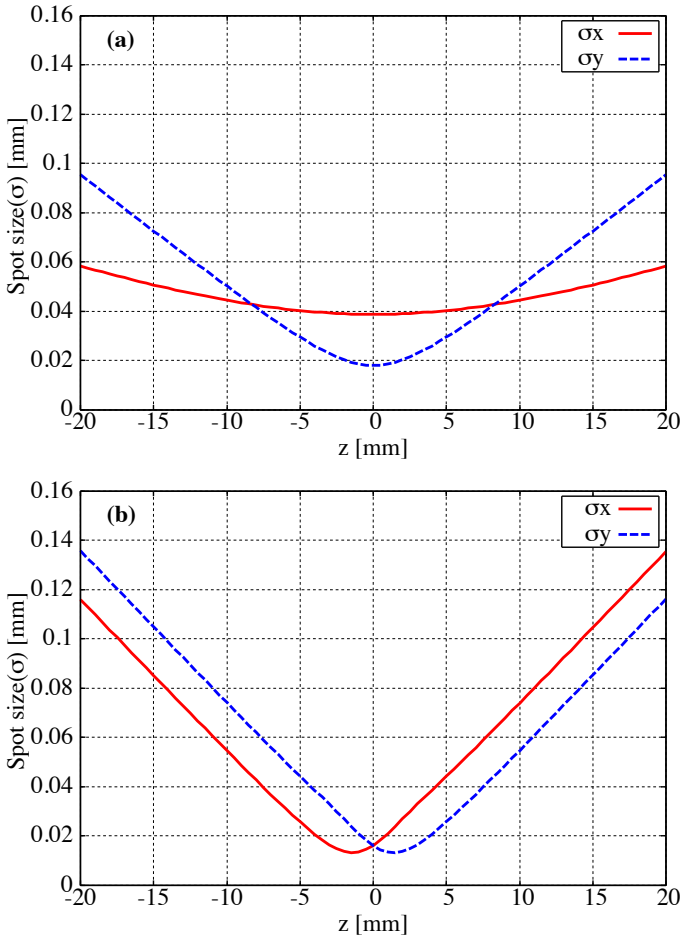

Figure 4.3: (a) The spot size of laser beam (σ) of a planar cavity. $z = 0$ corresponds to the designed laser–electron interaction point. (b) The spot size of laser beam (σ) of the 3D 4-mirror cavity. At $z = 0$ is, laser beam profile is rounder compared to the planar cavity at $z = 0$.

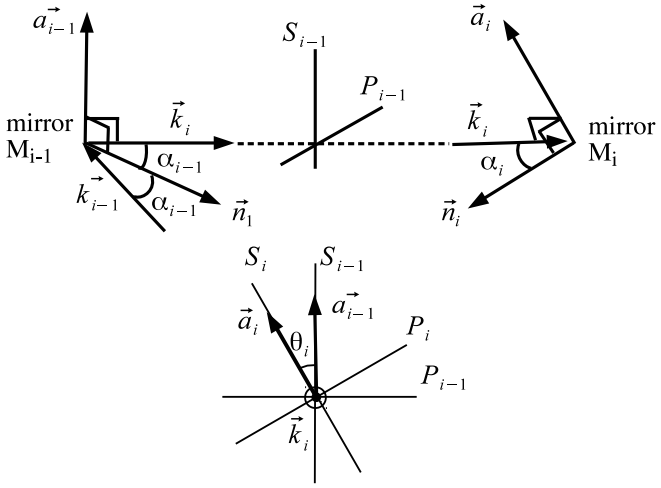

Figure 4.4: Principle of the calculation of geometric phase by the mirror reflections [27]. k_i is wave vector of the laser light, $\vec{n}_i$ is normal vector to the mirror M_i, and θ_i is the geometric phase.

where k_i being wave vector of the laser light. Then the geometric phase at reflection on mirrors M_{i-1} and M_i is

$$\cos\theta_i = \vec{a}_i \cdot \vec{a}_{i-1} \tag{4.4}$$

The geometric phase for a round trip of the cavity, $\sum\theta_i$, is 6.31 rad for current design described in Section 4.2.

The effect of the geometric phase in the 3D 4-mirror cavity for the linearly polarized laser beam is that the direction of polarization rotates around the axis of propagation in the cavity. Therefore the 3D 4-mirror cavity does not resonate with linearly polarized laser beams. On the other hand, the effect on the circularly polarized laser beam is a constant phase shift of the optical state which corresponds to a shift of the length of the optical path, i.e., length of the cavity. It should be noted that the sign of the phase shift is opposite for the left and right polarization. Thus the 3D 4-mirror optical cavity only resonates separately with the left or right circularly polarized laser beam at different optical path paths.

4.2 Design of the 3D 4-mirror cavity

4.2.1 General parameters

The schematic of the mirror configuration of the 3D 4-mirror cavity is shown in Fig. 4.5. The distance between each mirror is 420 mm and the round trip optical path of the cavity, L, is 1680 mm which is chosen to match the bunch separation of the ATF electron beam. The distances of M_1-M_3 and M_2-M_4 are 70 mm and the all incident angles, α_i, are 4.8°. In Fig. 4.5, M_1 and M_2 are flat mirrors while M_3 and M_4 are concave mirrors. The curvature of the concave mirrors is 420 mm. We used the dielectric multi-layer mirrors provided by REO (Research Electro-Optics,

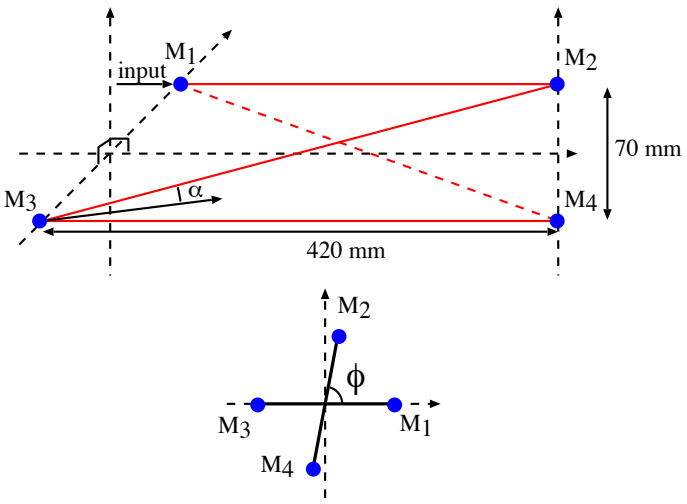

Figure 4.5: Schematic of the 3D 4-mirror cavity. M_1 is the plane mirror where the laser beam is injected. ϕ represents the twisting angle of the cavity. $\phi = 90°$ in the original design.

Inc.). The specifications of mirrors are summarized in Table 4.1. The reflectivity of coupling mirror M_1 (which the laser beam is injected into) is 99.9% while the reflectivity of M_2, M_3 and M_4 is 99.99%. The finesse $\mathcal{F}$ given by Eq. (3.73) is calculated to be 4830.

4.2.2 Calculation of the laser propagation in the cavity

Propagation of the laser light along the optical path (z-axis) is, in general, expressed in terms of transverse coordinates x, y and angular divergences $\theta_x = \partial x/\partial z$, $\theta_y = \partial y/\partial z$. With the paraxial approximation ($\theta \ll 1$), propagation of the laser can be expressed as

$$\begin{pmatrix} x' \\ y' \\ \theta'_x \\ \theta'_y \end{pmatrix} = \begin{pmatrix} A_{xx} & A_{xy} & B_{xx} & B_{xy} \\ A_{yx} & A_{yy} & B_{yx} & B_{yy} \\ C_{xx} & C_{xy} & D_{xx} & D_{xy} \\ C_{yx} & C_{yy} & D_{yx} & D_{yy} \end{pmatrix} \begin{pmatrix} x \\ y \\ \theta_x \\ \theta_y \end{pmatrix} = M_t \begin{pmatrix} x \\ y \\ \theta_x \\ \theta_y \end{pmatrix} \tag{4.5}$$

$$\begin{pmatrix} A & B \\ C & D \end{pmatrix} \equiv \begin{pmatrix} A_{xx} & A_{xy} & B_{xx} & B_{xy} \\ A_{yx} & A_{yy} & B_{yx} & B_{yy} \\ C_{xx} & C_{xy} & D_{xx} & D_{xy} \\ C_{yx} & C_{yy} & D_{yx} & D_{yy} \end{pmatrix} \tag{4.6}$$

where M_t is a transfer matrix to express propagation of the laser via an optical path or a component. The transfer matrix for a free space over distance l can be expressed as

$$D(l) = \begin{pmatrix} 1 & 0 & l & 0 \\ 0 & 1 & 0 & l \\ 0 & 0 & 1 & 0 \\ 0 & 0 & 0 & 1 \end{pmatrix} \tag{4.7}$$

Table 4.1: Specification of mirrors for the 3D 4-mirror cavity.

Description	**Value**
Substrate Material	Fused Silica
Diameter	25.4 mm
Scratch-Dig	10-5
Reflectivity	
M_1	99.9%
M_2, M_3 and M_4	99.99%
Transmittance	
M_1	0.08%
M_2, M_3 and M_4	0.007%

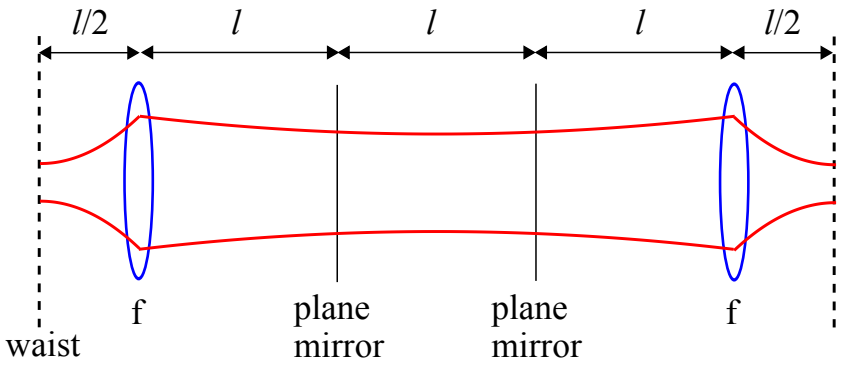

Figure 4.6: Lens-guide structure equivalent to the 3D 4-mirror cavity.

The transformation through an astigmatic thin lens is given by

$$F(f_1, f_2) = \begin{pmatrix} 1 & 0 & 0 & 0 \\ 0 & 1 & 0 & 0 \\ -1/f_1 & 0 & 1 & 0 \\ 0 & -1/f_2 & 0 & 1 \end{pmatrix} \tag{4.8}$$

The effect of the geometric phase can be incorporated by a rotation matrix as

$$R(\theta) = \begin{pmatrix} \cos\theta & \sin\theta & 0 & 0 \\ -\sin\theta & \cos\theta & 0 & 0 \\ 0 & 0 & \cos\theta & \sin\theta \\ 0 & 0 & -\sin\theta & \cos\theta \end{pmatrix} \tag{4.9}$$

where θ is the geometric phase acquired through the propagation.

For calculating laser beam propagation in the cavity it is convenient to transform the optical cavity into the lens-guide structure of Fig. 4.6. The transfer matrix to describe propagation of the laser beam for a round trip of the 3D 4-mirror cavity is in the form

$$M_t = D(l/2)F(f_{t3}, f_{s3})R(\theta_3)R(\theta_2)R(\theta_1) \\ D(3l)F(f_{t4}, f_{s4})R(\theta_4)D(l/2) \tag{4.10}$$

where l is the distance between the mirrors (420 mm for current design). The transfer matrix starts and ends at the center of the two concave mirrors because the laser beam profile at this point (laser–electron IP) is of interest in the laser-Compton experiments. The matrix M_t has two eigenvalues which represent the round-trip Gouy phase [24]. It reflects the fact that the laser beam profile in the cavity is ellipse and has two eigen axes corresponding to major and minor ones.

For the general Gaussian beams, the complex radius of curvature tensor Q can be used in the 4×4 ABCD law [28, 29].

$$Q^{-1} = \begin{pmatrix} 1/q_x & 1/q \\ 1/q & 1/q_y \end{pmatrix} \tag{4.11}$$

When Gaussian beam propagation through a optical element of $\begin{pmatrix} A & B \\ C & D \end{pmatrix}$ given by Eq. (4.6), Q_1^{-1} becomes Q_2^{-1} as

$$Q_2^{-1} = (C + D \cdot Q_1^{-1}) \cdot [(A + B \cdot Q_1^{-1})]^{-1} \tag{4.12}$$

For the optical cavity, the q-parameter should be the same after a round trip to keep resonance. The eigenmode of the optical cavity is obtained by solving an equation $Q_2^{-1} = Q_1^{-1}$.

$$\frac{1}{q_i(z)} = \frac{1}{R_i(z)} - i\frac{\lambda}{\pi w_i^2(z)}, \quad i = x,\, y \tag{4.13}$$

$$\frac{1}{q(z)} = \frac{1}{R(z)} - i\frac{\lambda}{\pi w^2(z)} \tag{4.14}$$

In general contours of intensity and phase of the beam are ellipse as shown in Fig. 4.7. Here θ_w and θ_R are

$$\tan(2\theta_w) = \frac{2/w^2}{1/w_y^2 - 1/w_x^2} \tag{4.15}$$

$$\tan(2\theta_R) = \frac{2/R}{1/R_y - 1/R_x} \tag{4.16}$$

Major axis w_1 and minor axis w_2 are given by

$$w_1^2 = \left(\frac{\sin^2\theta_w}{w_x^2} + \frac{\cos^2\theta_w}{w_y^2} + 2\frac{\sin\theta_w\cos\theta_w}{w^2}\right)^{-1} \tag{4.17}$$

$$w_2^2 = \left(\frac{\cos^2\theta_w}{w_x^2} + \frac{\sin^2\theta_w}{w_y^2} - 2\frac{\sin\theta_w\cos\theta_w}{w^2}\right)^{-1} \tag{4.18}$$

Fig. 4.8 shows the laser beam profile in a plane closed to the laser-electron interaction point.

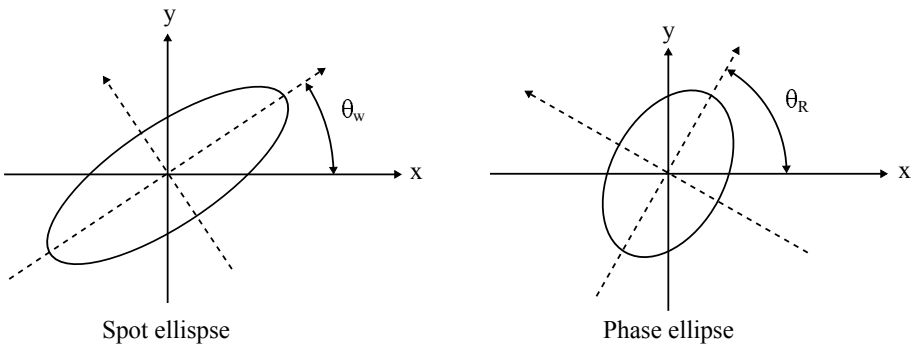

Figure 4.7: Spot ellipse and phase ellipse [30].

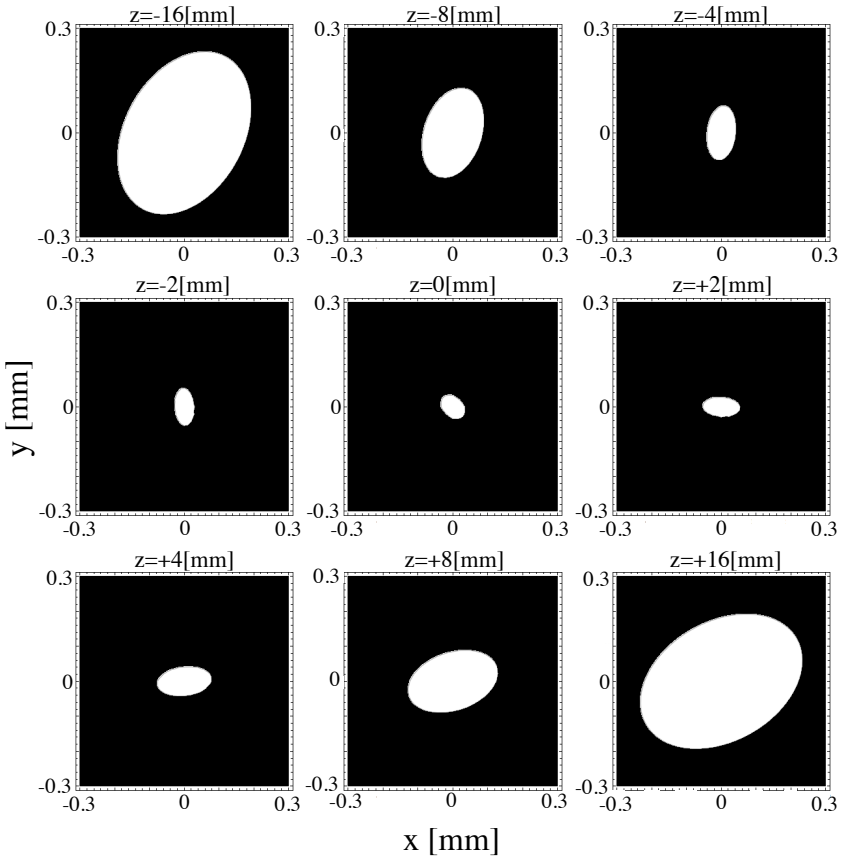

Figure 4.8: Laser beam profile of the 3D cavity in a plane closed to the laser-electron interaction point ($z = 0$). The z-axis is the cavity optical path.

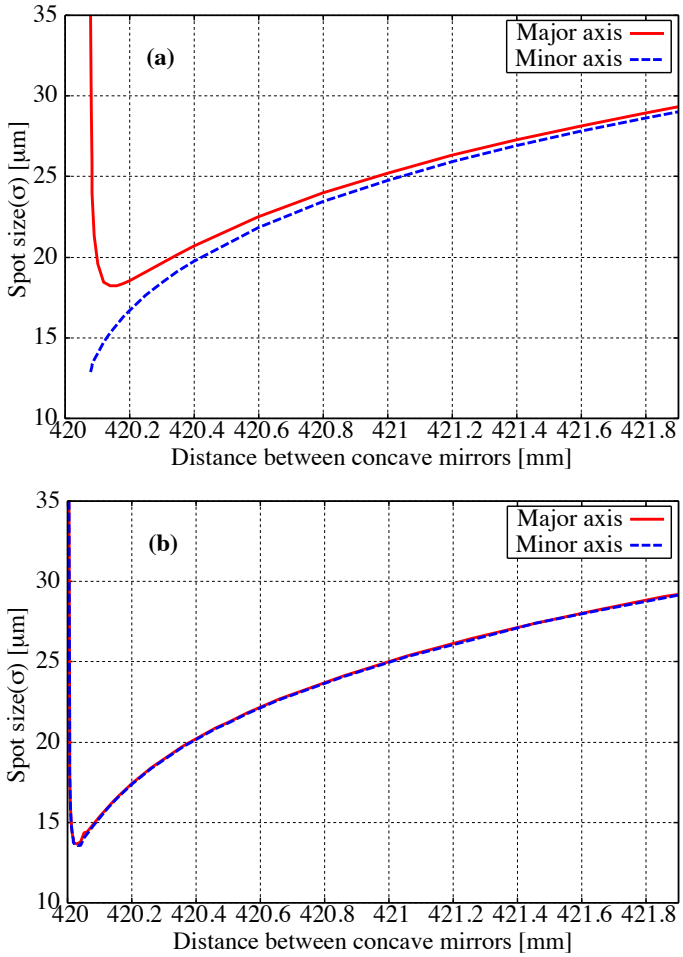

Figure 4.9: The spot size of laser beam in major axis and in minor axis at the collision point as function of the distance between concave mirrors. (a)$\phi = 90°$, (b)$\phi = 91.2°$.

Due to the three dimensional configuration of the path, the elliptical laser beam profile in the cavity rotates during propagation [31, 32]. We optimized the configuration of mirrors of the cavity to maximize the efficiency of laser–electron interaction based on the calculation with the transfer matrix (Eq. (4.10)). The calculated waist size of the laser beam at the laser-electron interaction point is shown in Fig. 4.9 as a function of the distance between two concave mirrors while keeping total length of the optical path constant. Fig. 4.10 shows the laser beam spot sizes in its major and minor axis along the propagation in the cavity. We found that the laser beam profile is elliptical in shape and is not optimized with the original design ($\phi = 90°$ in Fig. 4.5) as shown in Fig. 4.9(a) and 4.10(a). We chose that $\phi = 91.2°$ to obtain stable resonant condition and rounder profile with a smaller laser beam waist at the laser-electron interaction point. The designed waist size is 15 μm (σ) at the interaction point.

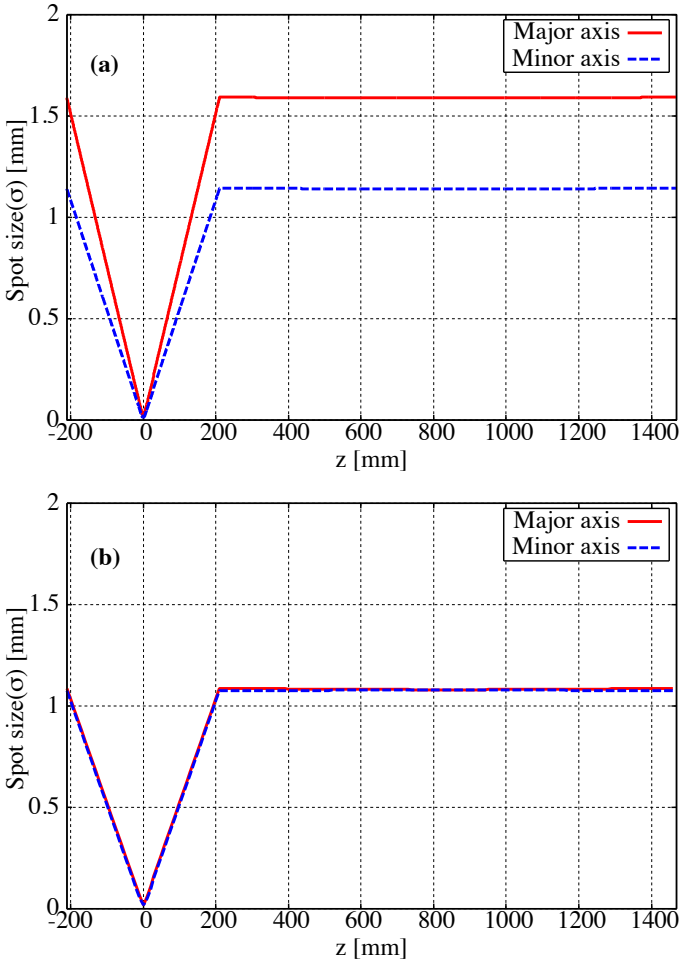

Figure 4.10: The spot size of laser beam in major axis and in minor axis along the propagation in the cavity. (a) $\phi = 90°$, (b) $\phi = 91.2°$.

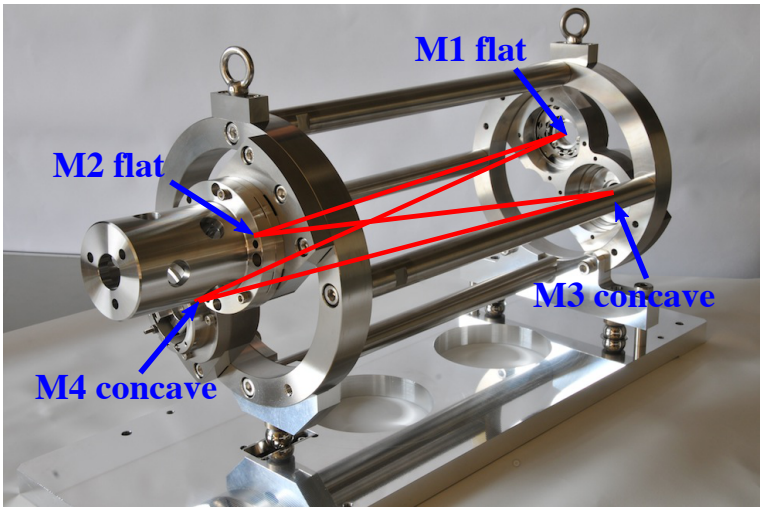

Figure 4.11: The 3D 4-mirror cavity.

4.2.3 Structure of mirror holder

The picture and drawing of the constructed 3D 4-mirror cavity are shown in Fig. 4.11 and Fig. 4.12. The mirror holders of M_1 and M_4 have two directional tilting mechanisms for initial alignment of mirrors. We adopted a gimbal mount for the mirror holders of the cavity by which the mirrors pivot on the center of mirror's front surface as shown in Fig. 4.13. Piezo actuators were attached to the mirror M_2 and M_3 via a leaf spring as shown in Fig. 4.14. The length of piezo actuators is 15 mm and 70 mm for M_3 and M_2, respectively.

4.2.4 The feedback control system

To accumulate laser pulses in the cavity and continuously make collisions of laser pulses with electron bunches, the optical path, L, of the cavity must be kept at the resonance condition ($L = n\lambda$) with a precision of $dL \ll \lambda/\text{enhancement} \sim 10^{-9}$ m and the timing of laser pulses and electron bunches must be synchronized within about 10 ps. The shorter piezo actuator of the optical cavity is used to synchronize the laser pulses with the electron pulses. The longer one is used for slow feedback, i.e., to adjust the length of the optical path to the circumference of ATF ring due to seasonal variation of ambient temperature. As the resonance condition affects the synchronization and vice versa, the system is not stable if we control these conditions independently. Therefore we constructed a closed loop feedback system consisting of the resonance and synchronization signal as shown in Fig. 4.15. In the feedback loop, the resonance signal from the optical cavity was fed to the mode-locked laser, while the synchronization signal was fed into the shorter piezo actuator of the optical resonant cavity. Because resonance feedback needs relatively faster response than timing synchronization, the piezo actuator inside the laser oscillator is used to keep the cavity on resonance.

We adopted a new scheme for the feedback control system, which utilized the polarization property of the 3D 4-mirror cavity [33]. The optical setup of the

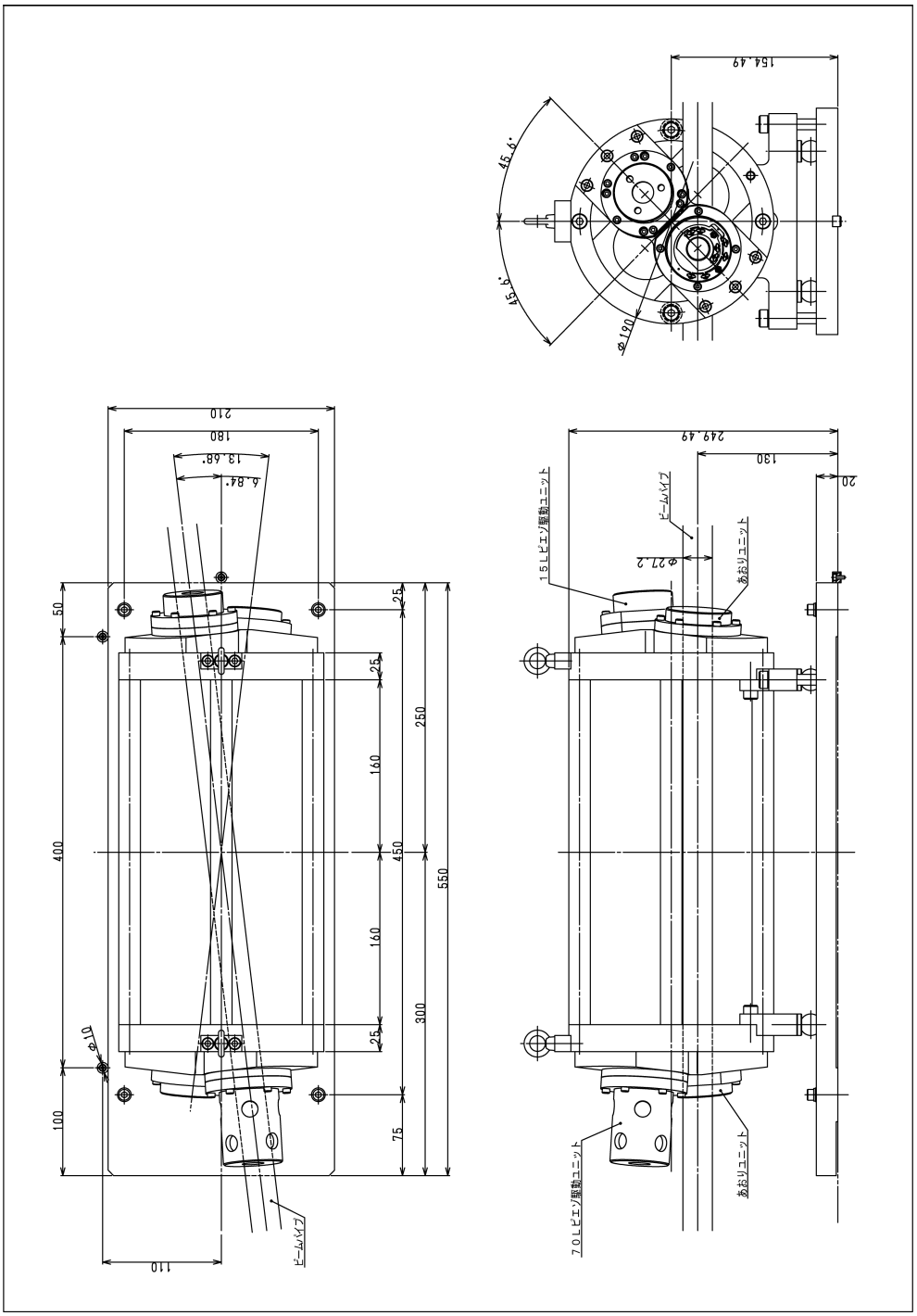

Figure 4.12: Drawing of the 3D 4-mirror cavity.

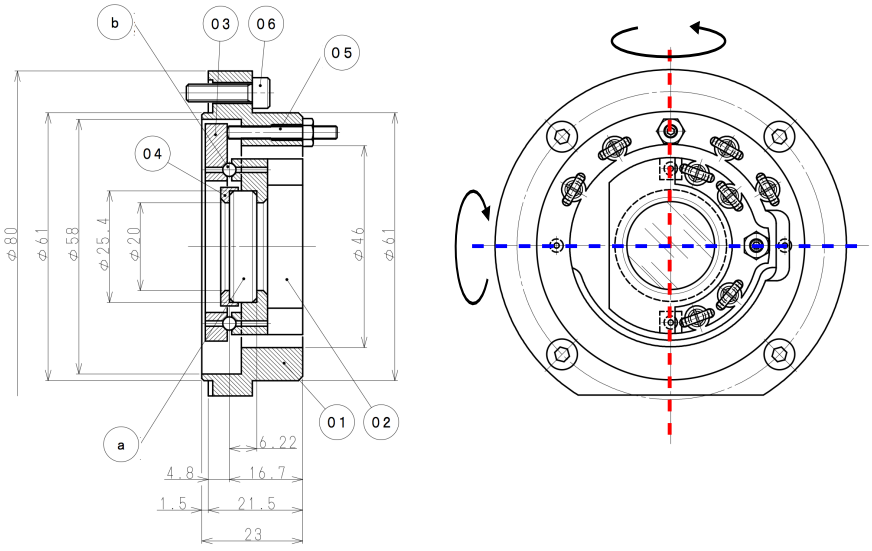

Figure 4.13: Gimbal mirror mount.

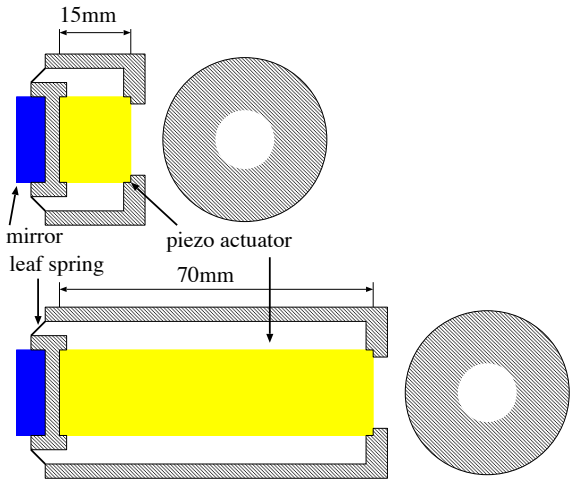

Figure 4.14: Close view of mirror attachment with the piezo actuator. Two mirrors are attached to the piezo actuator via the leaf spring. The piezo actuator is cylindrical with a hole to let a laser beam go through.

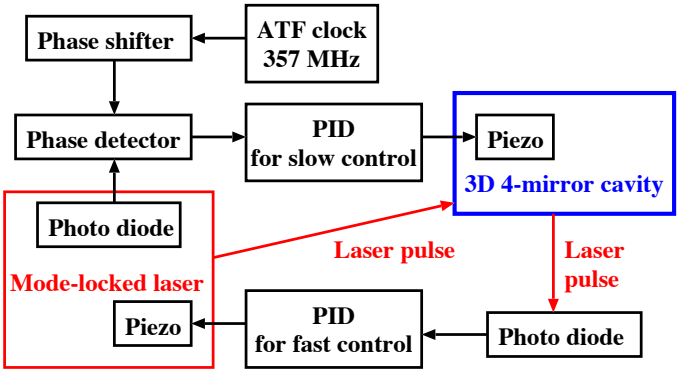

Figure 4.15: The scheme of the feedback system for laser-Compton scattering.

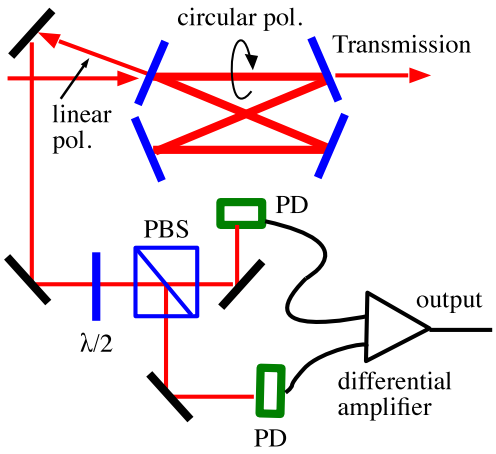

Figure 4.16: The optical setup for the feedback system.

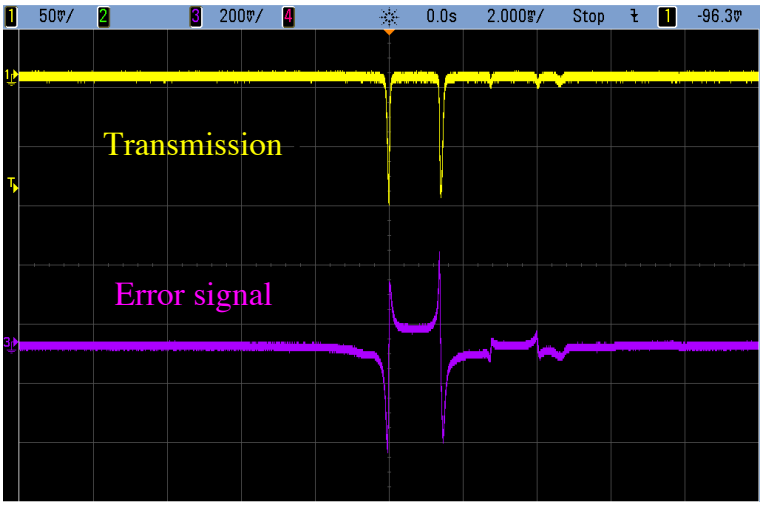

Figure 4.17: The transmission and the error signal for the feedback system utilizing the polarization property of the 3D 4-mirror cavity.

feedback system is shown in Fig. 4.16. In the system, a linearly polarized laser beam is injected into the cavity. As described in previous section, only circularly polarized component is fed into the cavity due to the geometric phase. The phase of the circular component depends on the resonance condition of the cavity and is eventually changes the direction of the linear polarization of reflected light from the coupling mirror. The direction of the polarization can be monitored using a Polarized Beam Splitter (PBS) and is used as the "error signal" of the feedback system. A typical error signal and intensity of the corresponding transmitted light, which is proportional to the stored laser power in the cavity, are shown in Fig. 4.17. The figure, obtained by scanning the optical path of the cavity showed that the error signal is essentially the differentiation of the stored intensity.

Chapter 5

Performance of the cavity

5.1 Measurement of mirror transmittance

The transmittance of mirrors is an important parameter to estimate the stored laser power in the cavity. The transmittance was measured by comparing the incident laser power to and transmitted laser power from the mirror. Table 5.1 shows the result of measurements. The specification of transmittance of mirrors provided by the manufacturer (REO) are shown in Fig. 5.1. The measured transmittance of M_1 is slightly lower than the specification while that of M_2 is consistent. On the other hand, it is difficult to measure the reflectivity of mirrors directly, thus it is estimated from the finesse of the optical cavity as described in next section.

Table 5.1: The transmittance measurement of mirrors.

Mirror	**Transmittance**
Input coupling mirror (M_1)	0.074%
Output mirror (M_2)	0.008%

5.2 Measurement of the finesse

Fig. 5.2 and Fig. 5.3 show intensity of the transmitted light from M_4 while changing the length of the optical path L. A clear peak in the strength of the transmitted light was observed at where the cavity resonated with incoming laser pulses. The finesse of the cavity was calculated by the ratio of Free Spectral Range (FSR) and FWHM width of the resonance and was

$$F = \frac{\mathrm{FSR}}{\mathrm{FWHM}} = 4040 \pm 420 \tag{5.1}$$

Since the typical width of the resonance was small as 270 pm, the measurement was vulnerable with the external disturbances and fluctuated for each measurement. As a result, the finesse measured using this method had about a 10% error.

We also measured the finesse by the decay time of the stored laser power. Fig. 5.4 shows the setup for measurement of the decay time. A Pockels cell is

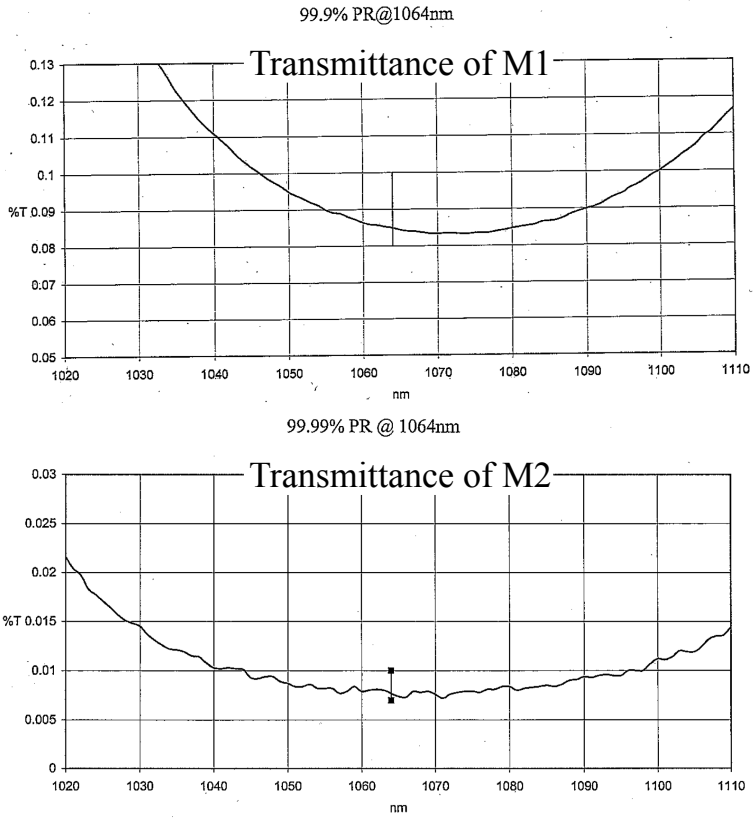

Figure 5.1: The specification of mirror transmittance measured by REO.

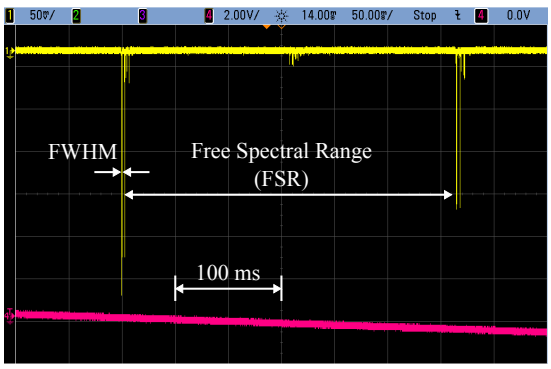

Figure 5.2: The resonance peaks obtained by scanning the optical path of the cavity.

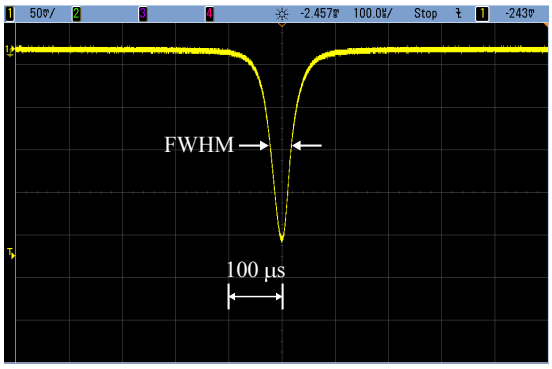

Figure 5.3: The resonance peak of fundamental mode.

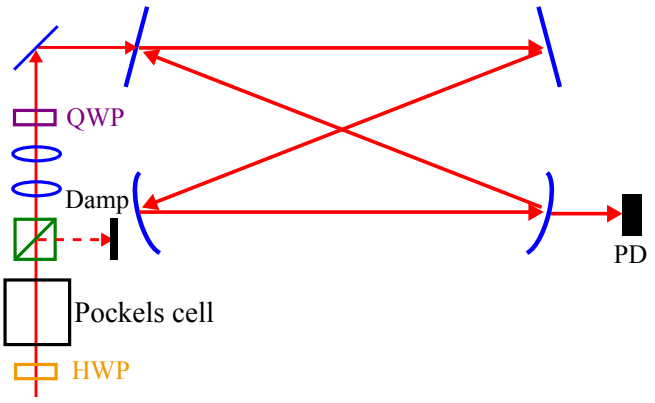

Figure 5.4: Setup of the measurement of the decay time of the laser power in the cavity.

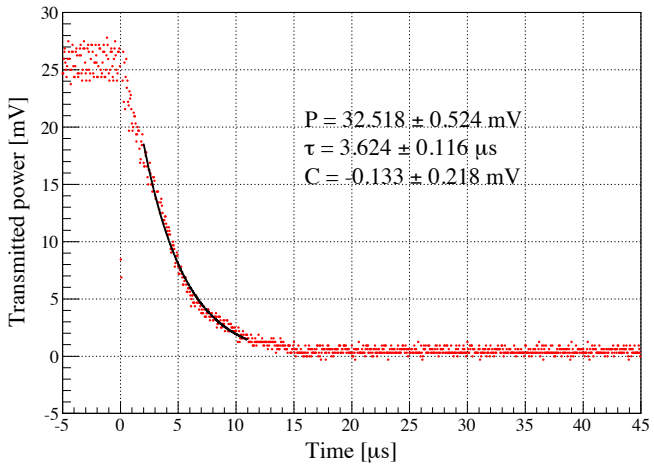

Figure 5.5: The measured result of the decay time. The black line is the fitted curve with $P(t) = P\exp(-t/\tau) + C$, where P is the initial laser power, τ is the decay time and C is the offset. The decay time obtained by fitting is $\tau = 3.6 \pm 0.1\,\mu\text{s}$.

equipped to cut off injection of the laser light sufficiently faster than the decay time. The result is shown in Fig. 5.5. The time dependence was fitted with the function $P(t) = P\exp(-t/\tau) + C$ with P, τ and C being free parameters. The finesse is calculated as $F = 2\pi c\tau/L$, where c is the light velocity in vacuum. The measured decay time was $3.6 \pm 0.1\,\mu\text{s}$ which corresponded to the finesse of 4040 ± 110. The results of measurements are summarized in Table 5.2 with the design value. The two measurements were consistent each other but were smaller than the one expected from the reflectivity of mirrors. It appeared that effective reflectivity $R = \sqrt{R_1R_2R_3R_4}$ was down to 99.922%, possibly by contamination, while it was expected to be 99.935% from the specification of mirrors.

Table 5.2: The finesse of the 3D 4-mirror cavity.

Method	**Finesse**
Design	4830
Decay time method	4040±110
Ratio of FSR and FWHM	4040±420

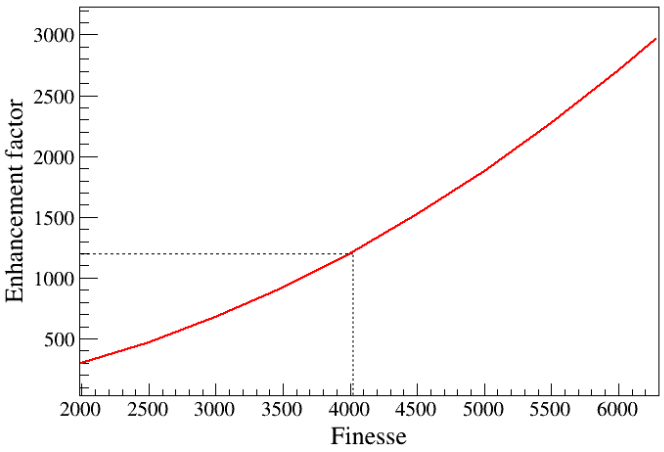

Figure 5.6: Enhancement factor vs finesse. The transmittance of mirror M1 was assumed to be 0.074%.

5.3 Stored power in the cavity

The enhancement factor of the laser power in the optical cavity on resonance is estimated to be

$$\frac{P_s}{P_i} = \frac{T_1}{(1-R)^2} \tag{5.2}$$

where P_i is the input power into the cavity and P_s is the stored power in the cavity. The effective reflectivity R was estimated to be 0.99922 by Eq. (3.67) with the measured finesse of 4000. The transmittance T_1 of the coupling mirror M_1 was independently measured to be 0.074%. Therefore, the power enhancement factor was estimated to be 1200. Fig. 5.6 shows the enhancement factor of the cavity as a function of finesse.

In order to understand the consistency between input into, stored in and output from the cavity, we measured power balance of the cavity. The result of a typical measurement is shown in Fig. 5.7. Here we measured the transmitted and the reflected power long enough after turning on the feedback system, because rapid decrease in power was observed in the initial moment after turning on the feedback system (See, Section 5.5 in detail). When the cavity was off resonance, all power was reflected at the coupling mirror M_1 and was measured to be 6.6 W. When the cavity is on resonance, a part of incoming laser beam was injected into the cavity and reflected power reduced to 5.4 W. Since the cavity is designed such

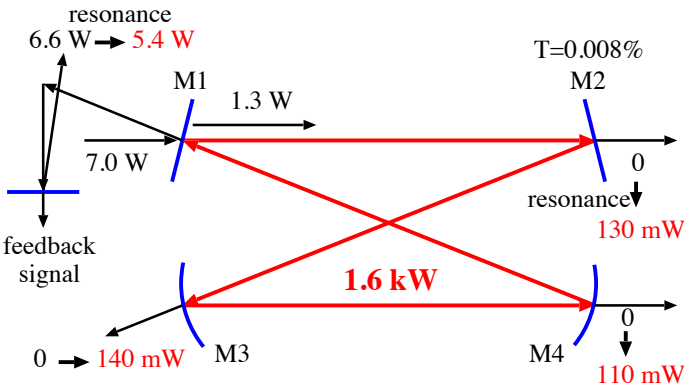

Figure 5.7: Measurement of power balance of the cavity. The input, stored and transmitted power for the case that cavity is on/off resonance are shown (See text in detail).

that the reflected power drops to zero at the resonance with the ideal condition[1], remaining reflected power at the resonance can be regarded as a deviation of the coupling from the ideal condition. Hence, from the reflected power at on and off resonance, the coupling was calculated to be $(6.6 - 5.4)/6.6 = 0.18$. It should be noted that the cavity can only resonates with a circular polarized state, the coupling efficiency is 0.5 at the maximum for linearly polarized laser beams. The transmitted power from M_2 was measured to be 130 mW and the transmittance of M_2, which was independently measured, was 0.008%. The stored power in the cavity was calculated to be $0.13/(8 \times 10^{-5}) = 1.6$ kW. On the other hand, the injected power into the cavity was calculated to be 1.3 W ($1.3 = 7.0 \times 0.18$) from the coupling efficiency and the power enhancement factor was estimated to be 1200 from Eq. (5.2). The stored power in the cavity was calculated to be $1.3 \times 1200 = 1.6$ kW, which was consistent with the estimate from the transmitted power and the transmittance of M_2.

Summation of the transmitted power from M_2, M_3 and M_4 was $(0.13 + 0.14 + 0.11) \sim 0.4$ W, while the injected power to the cavity was estimated to be 1.3 W. The difference of the two, $(1.3 - 0.4) \sim 0.9$ W, could be attributed to the power losses on the mirror. Assuming the same power loss ratio on each mirror, the power loss on each mirror was estimated as $(0.9/4/1600) \sim 100$ ppm.

5.4 An effect of misalignment

The transmitted laser beam profile from the cavity is shown in Fig. 5.8. An elliptical beam profile was observed. It indicates that the laser beam profile at the laser-electron interaction point is also an ellipse despite the fact that the cavity was designed to obtain a rounder profile as described in Section 4.2.2.

It is presumed that although configuration of mirrors were designed to make a round profile of the laser beam by setting the twisted angle $\phi = 91.2°$, the effective

[1]Here injection of circularly polarized light is assumed.

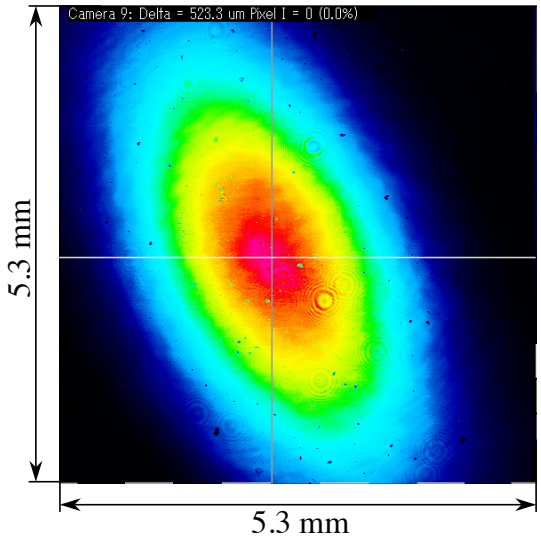

Figure 5.8: The transmitted laser beam profile from mirror M_2.

angle of the laser path ϕ_{eff} deviated from the designed value. For example, in Fig. 5.9, we show the change of ϕ_{eff} as a function of the distance of the position of laser beam on the M_3 from its center. Since the only mirror holders of M_1 and M_4 had a tilting mechanism to aligned mirrors, the angle ϕ_{eff} might not be equal to the design value of 91.2° and caused elliptical profile of the laser beam. Because a round beam was injected into the cavity, it could be a reason for the low coupling efficiency described in previous section.

5.5 Possible thermal effect to the cavity

Fig. 5.10 shows the transmitted and reflected power from M_1 as a function of time after turning on the feedback system. We observed that the stored power in the cavity decreased to about a half of the maximum after several seconds. Another observation was the difference of the laser beam profile at the resonance when scanning the length of the cavity and when turning on the feedback system as shown in Fig. 5.11. In Fig. 5.11(b), a distortion was observed in the profile, where the picture was taken after rapid decrease of the transmitted and reflected power shown in Fig. 5.10. Since the decrease in the transmitted power and the distortion of the laser beam profile were not observed when the stored power in the cavity was low, it is suspected that heat load due to the power loss on the mirrors distorted the shape of mirrors which may be an additional reason reason for the small coupling efficiency.

5.6 Estimation of the beam waist

The waist sizes of the laser beam were estimated by extrapolating the measured profile of the transmitted light from M_2 (Fig. 5.11(b)) with the transfer matrix described in Section 4.2.2. Fig. 5.12 shows the optical structure from the IP

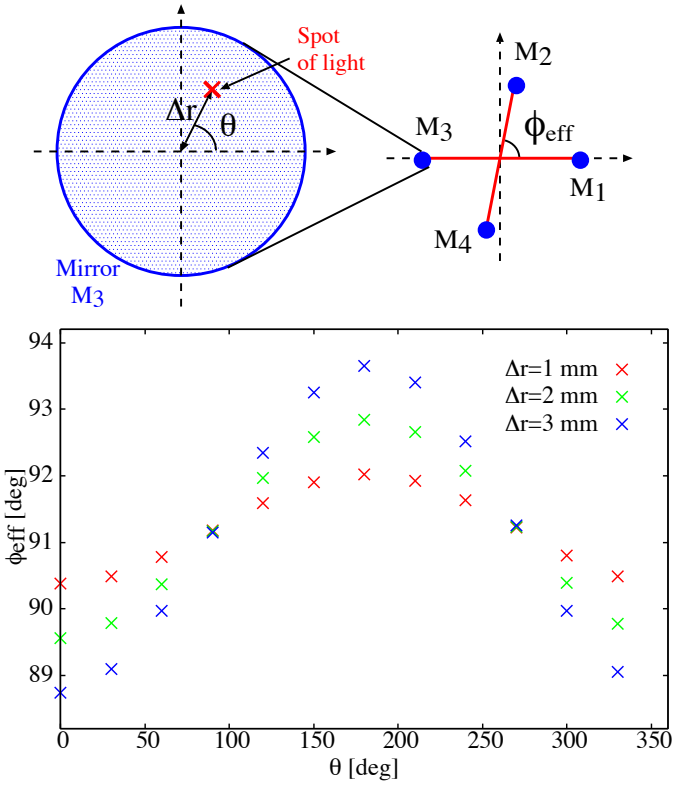

Figure 5.9: The change of ϕ_{eff} as a function of the misalignment of the laser beam from the center of M_3.

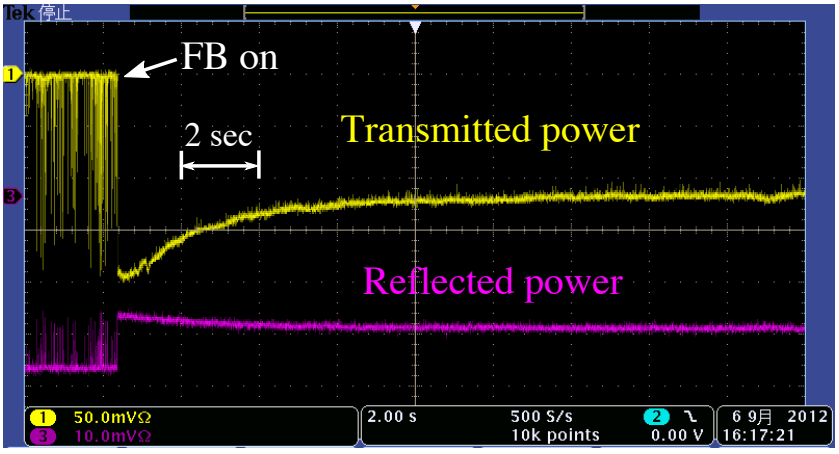

Figure 5.10: The observation of stored power reduction after turning on the feedback system.

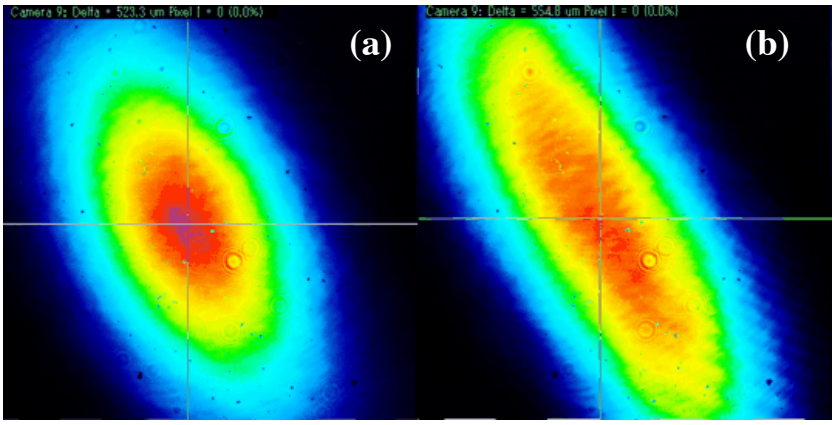

Figure 5.11: (a) The transmitted laser beam profile from mirror M_2 when scanning the length of optical path (same as Fig. 5.8) and (b) the cavity is on resonance.

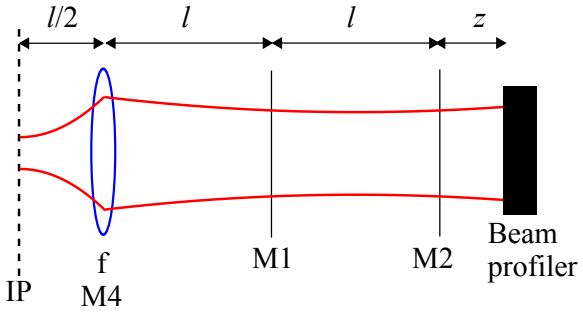

Figure 5.12: Lens-guide structure to describe propagation from IP to outside of M_2.

to the beam profile monitor set outside of M_2. The transfer matrix to describe propagation of the laser beam from the monitor to the IP is

$$M_t = D(z)I_2I_1D(l)R(\theta_1)D(l)F(f_{t4}, f_{s4})R(\theta_4)D(l/2) \tag{5.3}$$

I_1 and I_2 represent the interface of mirror M_2;

$$I_2I_1 = \begin{pmatrix} 1 & 0 & 0 & 0 \\ 0 & 1 & 0 & 0 \\ 0 & 0 & n & 0 \\ 0 & 0 & 0 & n \end{pmatrix} \begin{pmatrix} 1 & 0 & 0 & 0 \\ 0 & 1 & 0 & 0 \\ 0 & 0 & \frac{1}{n} & 0 \\ 0 & 0 & 0 & \frac{1}{n} \end{pmatrix} \tag{5.4}$$

where n is the refractive index of mirror. An estimated laser profile at the IP is shown in Fig. 5.13. The laser beam spot size projected onto vertical axis is calculated to be 16 µm.

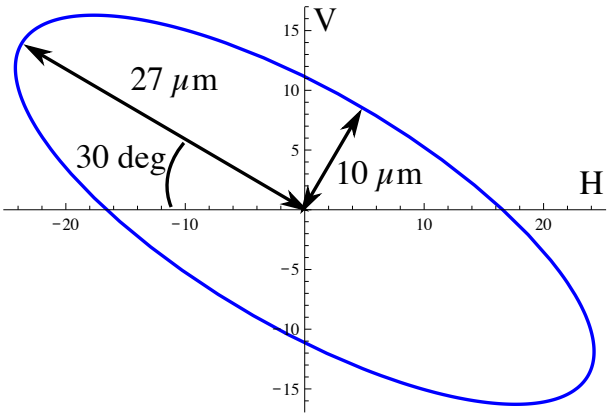

Figure 5.13: An estimated laser profile at the laser-electron interaction point.

Chapter 6

Experimental setup for gamma ray generation

We performed the experiments for gamma ray generation by collision of electron beams and laser pulses accumulated in the 3D 4-mirror cavity. The optical cavity was installed in the KEK-ATF damping ring (ATF-DR). A detector system was set up for gamma-ray detection. In this chapter, we describe the experimental setup.

6.1 KEK-ATF

The laser-Compton experiments were performed at the Accelerator Test Facility (ATF) in High Energy Accelerator Research Organization (KEK) [34]. The ATF is a facility to develop an ultra-low emittance electron beam required for the ILC. Fig. 6.1 shows the ATF layout.

The electron source is an RF gun with CsTe cathode driven by a mode-locked UV laser. The electron beam is accelerated to 1.28 GeV by the linear accelerator with RF cavity of 2856 MHz. After accelerated to 1.28 GeV, the electron beam is injected to the Damping Ring (DR). RF frequency of the DR is 714 MHz and the

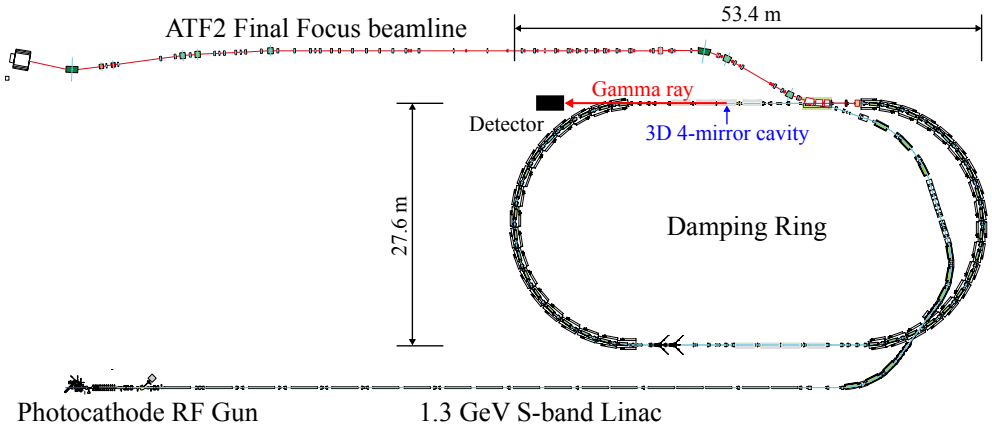

Figure 6.1: Schematic drawing of the ATF.

Table 6.1: Parameters of ATF damping ring.

Description	**Value**
Electron energy	1.28 GeV
Beam intensity	1×10^{10} e / bunch
Bunch spacing	5.6 ns
Circumference	138.6 m
RF frequency	714 MHz
Harmonic number	330
Emittance (ϵ_x / ϵ_y)	1.1×10^{-9} / 12×10^{-12} m·rad
DR revolution	2.16 MHz

revolution rate is 2.16 MHz. After about 500,000 turns in the DR, the emittance of the beam is damped to desired level and is extracted to the extraction line. This operation is called the normal mode. In the normal mode, the electron beam is injected into the DR with repetition of several Hz (1.56 Hz in our experiment). In the laser-Compton experiment, the ATF is in the storage mode, where the electron beam is not extracted to extraction line and is kept circulating in the DR. After circulation the electron beam is dumped and new one is injected to the ring. A bunch in the ATF beam contains about 10^{10} electrons and the accelerator is operative up to 10 bunches per train with the bunch separation of 5.6 ns. The experiment was performed in single and 5 bunches per train. The main parameters of the electron beam in the ATF are summarized in Table 6.1.

6.2 Optical setup

6.2.1 Laser oscillator and optical component

We used a mode-locked pulsed laser (COUGAR, Time-Bandwidth Products) as a seed laser to the optical cavity. It uses Nd:VAN as the lasing crystal and the wavelength is 1064 nm. The repetition rate and average power are 357 MHz and 10 W respectively as summarized in Table 6.2. Since the round trip optical path length of the 3D 4-mirror cavity, two laser pulses circulate in the cavity. The ATF has 165 RF buckets separated 2.8 ns each an electron bunch will collide with a laser pulse stored in the cavity every turn at the laser-electron interaction point. Fig. 6.2 shows time structure of electron bunches and laser pulses.

Fig. 6.3 shows the layout of optical components on the optical table. It consisted of an optical isolator (ISO), a half-wave plate (HWP), a quarter-wave plate (QWP), a polarizing beam splitter (PBS). The Gaussian beam parameter must be matched with the parameter of resonant condition of the optical cavity to store laser pulses. Thus we tuned the laser beam match to the TEM_{00} mode of the cavity by the telescope which configured by convex lenses. Since the cavity only resonates with the left or right circularly polarized laser beam as described in Sec-

Table 6.2: Parameters of the laser system.

Description	**Value**
Laser wavelength	1064 nm
Laser frequency	357 MHz
Laser pulse width	11 ps (FWHM)
Laser power	10 W (28 nJ / pulse)
Crossing angle	14°

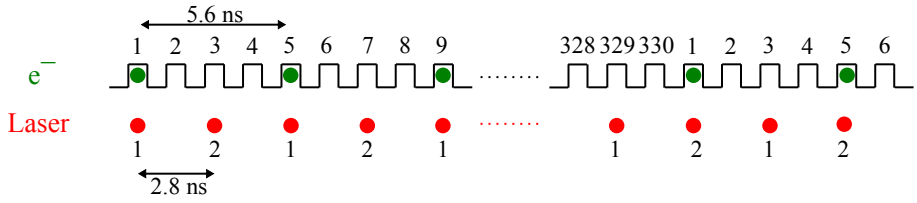

Figure 6.2: Time structure of electron bunches and laser pulses.

tion 4.1.2, the stored laser power ratio of left and right circularly polarization can be tuned using quarter-wave plate. During the gamma ray generation experiment, the ratio of left and right circularly polarization of injected laser beam was set to 2 : 1.

6.2.2 Vacuum chamber

The 3D 4-mirror cavity was placed in the vacuum chamber to keep the vacuum level in the electron beam pipe at tolerated level as shown in Fig. 6.4. The vacuum level of 10^{-6} Pa in the vacuum chamber is required by the ATF operation. A baking technique, which is usually used to improve vacuum level, is not applicable, because the high reflection mirrors and the piezo actuators are installed in the vacuum chamber. Especially, the piezo actuator could be damaged at temperature about 100°C. The vacuum chamber was continuously evacuated by two 100 l/min ion pumps. The pressure in the Compton chamber was kept at about 8×10^{-6} Pa.

The vacuum chamber was placed on an optical table. Fig. 6.5 shows the vacuum chamber in the ATF beam line. All components on the optical table were placed on the movable table. The position of the optical cavity (and the path of the laser) can be moved with the accuracy of 0.8 µm and 4.0 µm in vertical and horizontal direction respectively.

A water cooling system was attached at the top and bottom of the chamber for the purpose of compensating variation of the cavity length caused by a seasonal temperature change in the ATF environment. The water cooling plate is a copper plate with cooling water pipe. Fig. 6.6 shows the top view of the vacuum chamber.

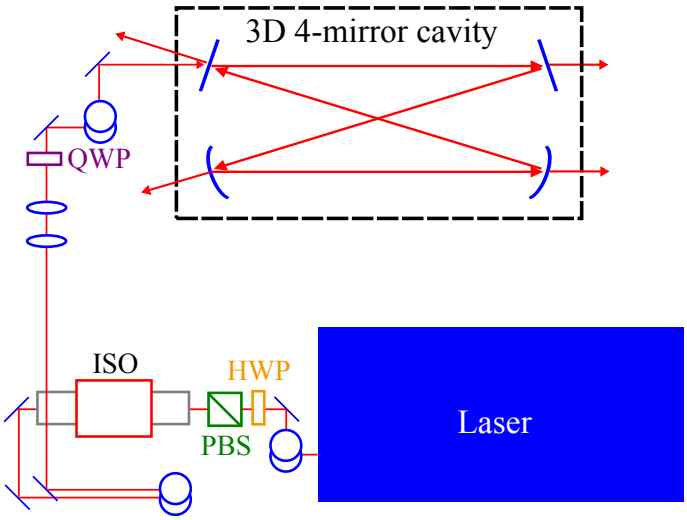

Figure 6.3: Schematic of laser optics.

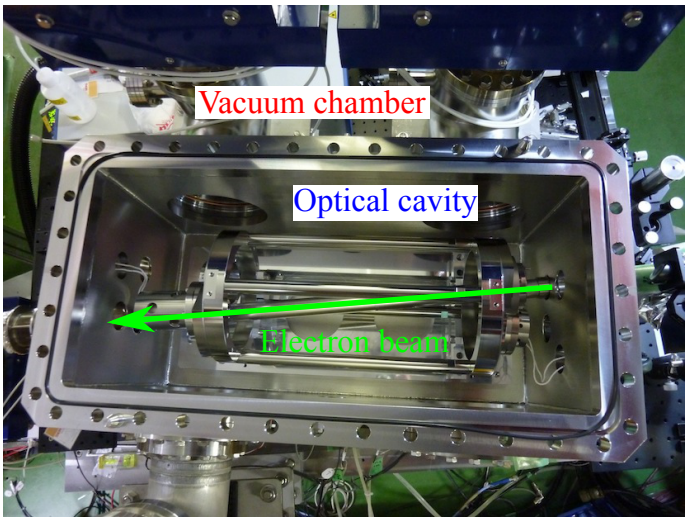

Figure 6.4: The optical cavity in the vacuum chamber.

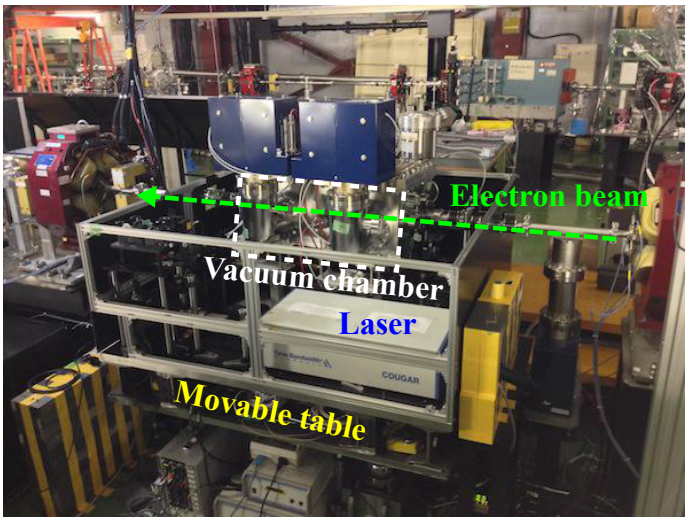

Figure 6.5: The optical cavity on the movable table.

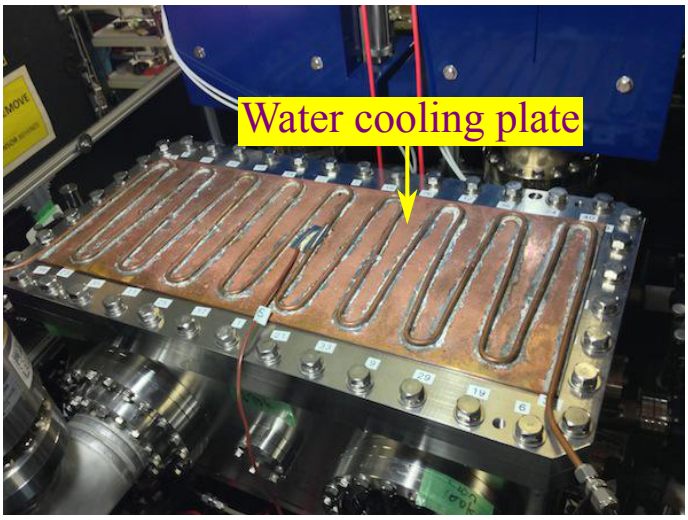

Figure 6.6: The top view of vacuum chamber.

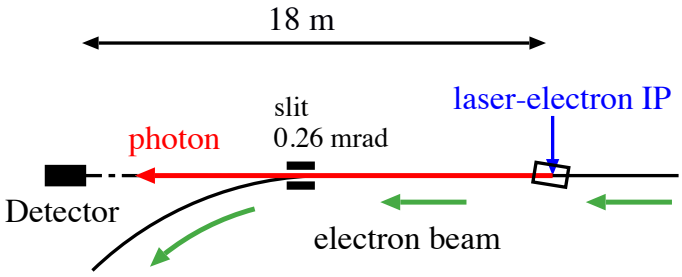

Figure 6.7: The schematic view of the cavity and the photon detector. The 3D 4-mirror cavity is installed in the north straight section of the ATF damping ring. The photon detector for photon detection is placed at 18 m downstream of the laser-electron interaction point.

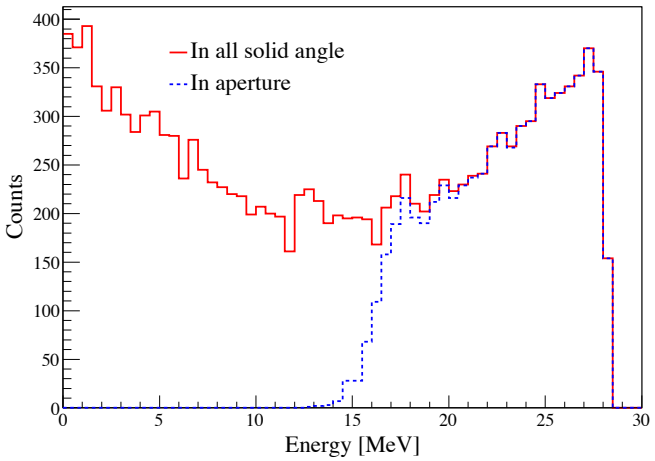

Figure 6.8: Energy distribution of generated gamma rays by the simulation code CAIN.

6.3 Detection system for gamma ray

The 3D 4-mirror cavity was installed in the north straight section of the ATF-DR. The gamma-ray detector was placed 18 m downstream of the laser-electron interaction point, as shown in Fig. 6.7. The crossing angle of the laser and the electron beams was 14°, which determined the maximum energy of the photon at 28 MeV. The energy of the photons in the detector acceptance is 19–28 MeV with the average of 24 MeV, which was limited by the slit of 0.26 mrad aperture placed between the laser-electron interaction point and the detector. Fig. 6.8 shows energy distribution of generated gamma rays by the simulation code CAIN [35].

6.3.1 Gamma-ray detector

Fig. 6.9 shows the configuration of the gamma-ray detector. We used two types of detector, i.e., a pure CsI detector and a BaF_2 in the experiments. A pure CsI detector is the main detector, it consists of a photomultiplier tube (PMT), a optical

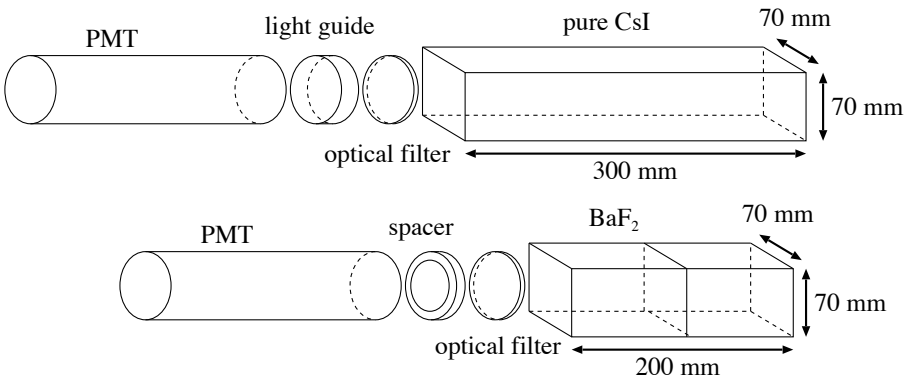

Figure 6.9: The configuration of gamma-ray detector..

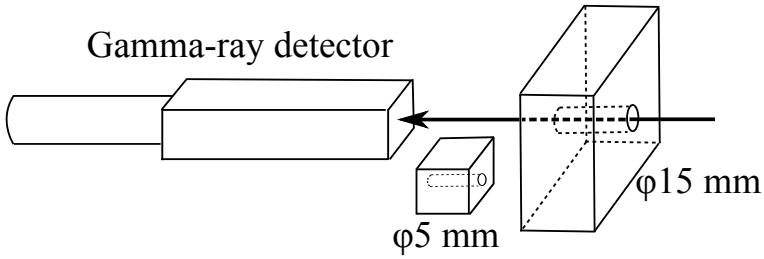

Figure 6.10: Scheme around gamma-ray detector.

filter, a light guide and a pure cesium iodide (CsI) crystal. The photomultiplier tube is R4275-02 (Hamamatsu Photonics K.K.) whose diameter of the photocathode of 46 mm. The pure CsI crystal is 70 mm wide, 70 mm high and 300 mm long. The pure CsI has luminescence of two decay components. The decay constant and wavelength of the peak yield for the faster decay component is 2–20 ns and 305 nm, while those for the slower decay component is 100–4000 ns and 450 nm respectively. The UV-pass filter was inserted between the CsI crystal and the photocathode of the PMT to block the slower component from the CsI. Thus the detector has capability to discriminate gamma ray from every turn in the ATF ring while gamma rays from a train (consisting of multiple bunches) piled up in the detector.

In front of the gamma-ray detector, two lead blocks were placed to reduce backgrounds as shown in Fig. 6.10. The lead block of far side from the detector has the hole of 15 mm in diameter. The lead block of near side of the detector has the hole of 5 mm in diameter and can be moved in transverse direction remotely while the 15 mm block was placed at fixed position throughout the experiment.

BaF_2 detector

The fast time response gamma-ray detector consists of a PMT, an optical band pass filter and barium fluoride (BaF_2) crystals. The PMT is H3378-51 based on R3377 (Hamamatsu Photonics K.K.) with diameter of the photocathode of 46 mm. The rise time of H3378-51 is about 0.7 ns with the nominal voltage 3.0 kV. BaF_2 crystal has two luminescence components [16, p. 345]. The decay constant and peak wavelength of the fast decay component is 0.9 ns and 220 nm while those of

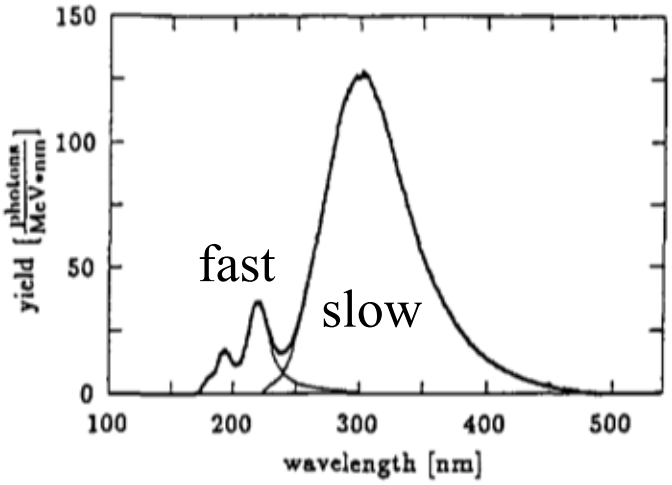

Figure 6.11: BaF_2 time resolved emission spectrum [36].

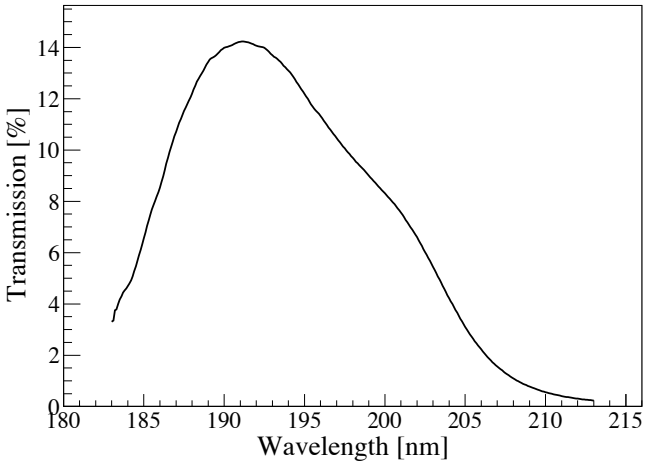

Figure 6.12: Transmission of optical bandpass filter for the BaF_2 detector. The bandwidth is 194 ± 8 nm.

the slow decay component is 630 ns and 300 nm respectively. The decay constant of the faster component is faster than the bunch spacing of in a train (5.6 ns). Fig. 6.11 shows time dependence of florescences of the BaF_2 crystal. We inserted an optical bandpass filter between BaF_2 crystal and PMT to cut out the slow component. The bandwidth of the filter is 194 ± 8 nm and the transmission of the filter is shown in Fig.6.12.

The waveform from the PMT was recorded using a digital oscilloscope DSO5054A (Agilent Technologies) which has the bandwidth of 500 MHz and maximum sampling rate 4 GSa/s. The oscilloscope was placed close to the BaF_2 to avoid attenuation of high frequency component in the signal during the transmission of in the cable.

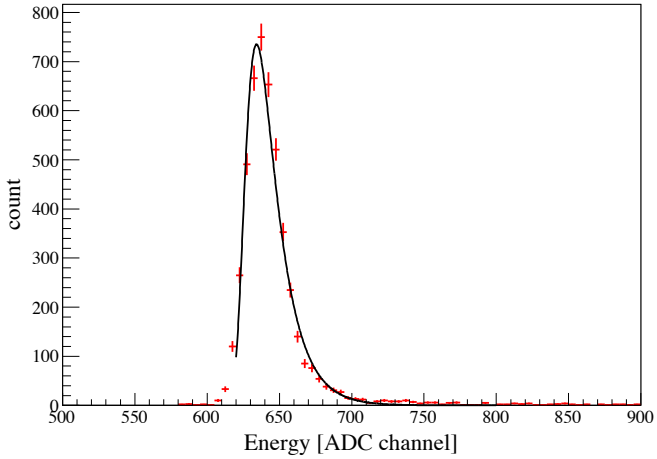

Figure 6.13: Energy deposit of cosmic ray in the CsI crystal.

6.3.2 Calibration of gamma-ray detector

Calibration of CsI detector

The CsI detector was calibrated by using the cosmic ray muons. The mean energy loss of a muon is $dE/dx = 5.6\,\mathrm{MeV}\,/\,\mathrm{cm}$ in a pure CsI [16]. Thus, energy deposit of a muon is 39.2 MeV when it passes through 70 mm in the pure CsI detector. A measured energy deposit of cosmic ray muons is shown in Fig. 6.13. The energy distribution was fitted by Landau distribution and the energy deposit of 39.2 MeV in the detector was defined to be 634.2 channel of the ADC by the fitting parameter. A pedestal of the ADC was 582.8 channel. The calibration factor was defined as

$$E\,[\mathrm{MeV}] = 0.7626 \times (\mathrm{ADC}\,[\mathrm{ch}] - 582.8) \tag{6.1}$$

Calibration of BaF_2 detector

The BaF_2 detector was also calibrated using cosmic ray. The mean energy loss of the cosmic ray muon is $6.5\,\mathrm{MeV}\,/\,\mathrm{cm}$ in BaF_2 [16]. Thus, the average energy deposit of a muon in the BaF_2 detector of 70 mm is 45.5 MeV. Fig. 6.14 shows a waveform from the BaF_2 detector with a cosmic ray. The calibration factor from the measured amplitude to the energy deposit in the detector was defined as $3.16\,\mathrm{MeV/mV}$.

6.3.3 Estimation of stored laser power

The stored laser power in the optical cavity can be obtained by the transmitted laser power and the transmittance of the mirror. The setup for the measurement of the transmitted laser power is shown in Fig. 6.15. The transmitted power from M_2 was measured by a laser power meter, and the transmitted power from M_4 was measured by a photo diode. A signal from of the photo diode is recorded by the ADC. A distribution of signals from the photo diode is shown in Fig. 6.16. Using

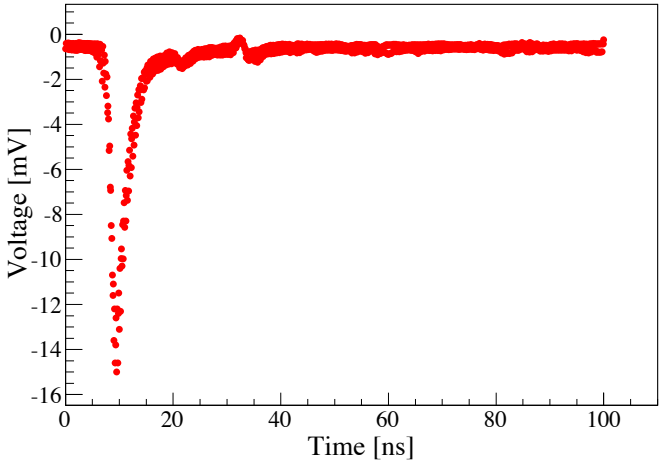

Figure 6.14: Waveform of cosmic ray in the BaF_2 crystal.

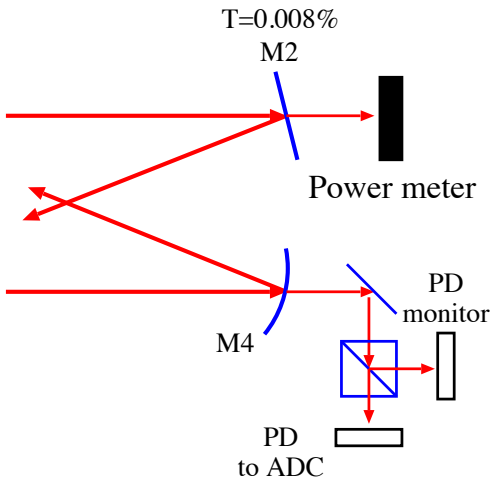

Figure 6.15: Calibration setup for transmitted power.

the transmittance of the M_2 of 0.008%, calibration factor from channel of the PD signal to the stored laser power in the optical cavity was determined as;

$$I\,[\mathrm{W}] = 0.02214 \times (\mathrm{ADC}\,[\mathrm{ch}] - 454.8)\frac{1}{0.08} \tag{6.2}$$

6.3.4 Calibration of laser pulse timing

We monitored the phase difference of the electron beam RF signal and the laser pulse signal as the laser pulse timing information. We used a sawtooth phase detector for feedback control system. When the phase difference of the electron beam RF signal and the laser pulse signal is $\Delta\phi$, one output from phase detector is $\arccos\Delta\phi$ and the other output is $\arcsin\Delta\phi$. The phase difference can be estimated from $\arccos\Delta\phi$ and $\arcsin\Delta\phi$. Two outputs are put into the ADC for recording the laser pulse timing. Fig. 6.20 shows the scatter plot of $\arccos\Delta\phi$ and $\arcsin\Delta\phi$

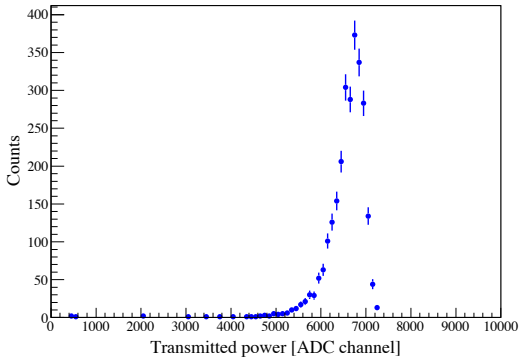

Figure 6.16: Distribution of transmitted power with keeping resonance.

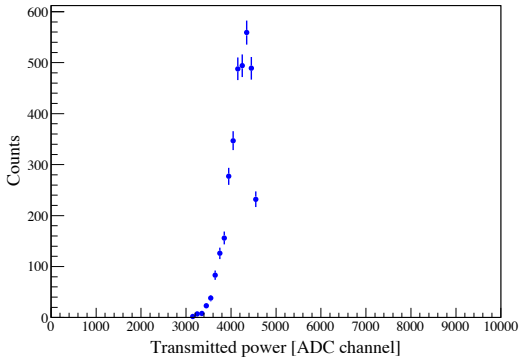

Figure 6.17: Distribution of transmitted power with keeping resonance.

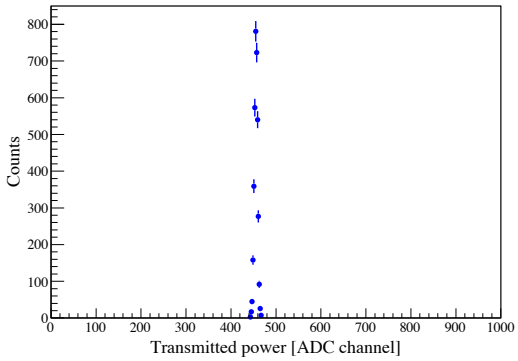

Figure 6.18: Distribution of transmitted power off feedback.

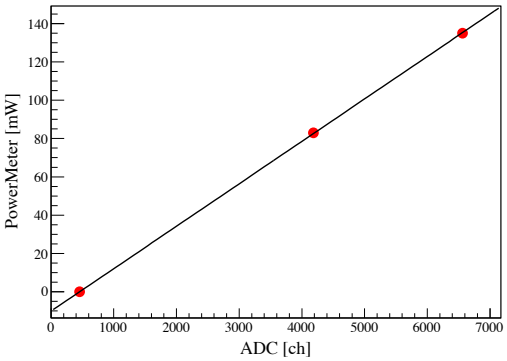

Figure 6.19: The measured value of laser power meter vs ADC.

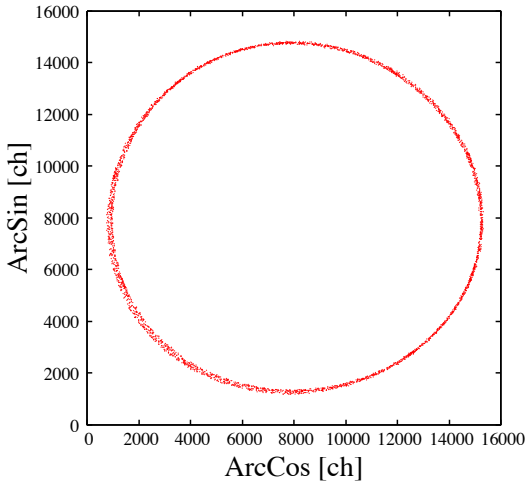

Figure 6.20: The scatter plot of $\arccos \Delta\phi$ and $\arcsin \Delta\phi$ as the laser pulse timing.

as the laser pulse timing. The center of the scatter plot was calculated $(x, y) = (7962, 7958)$. The laser pulse timing was calculated as;

$$\Delta\phi = \arctan\left(\frac{\arcsin \Delta\phi - 7958}{\arccos \Delta\phi - 7962}\right) \tag{6.3}$$

6.3.5 Data acquisition system

A schematic of the data acquisition system for the experiment is shown in Fig. 6.21. The data acquisition system is constructed based on the CAMAC standard. We used a 14-bit charge sensitive ADC (C009H) to record the strength of the signal. The ADC integrates the current to the input during the time window specified by a gate signal, and convert it to the digital information with 14-bit resolution. The gate signal for the ADC is created from the reference clock which is synchronized with the ATF-DR revolution of 2.16 MHz. At the same time with the gamma-ray data, the laser power in the optical resonant cavity and the phase difference of electron bunches and laser pulses are taken by the ADC. The electron beam current and position of the movable optical table are also recorded using the data control system of the ATF, Experimental Physics and Industrial Control System (EPICS) [37]. The entire system is capable of taking data with a rate of 200 Hz.

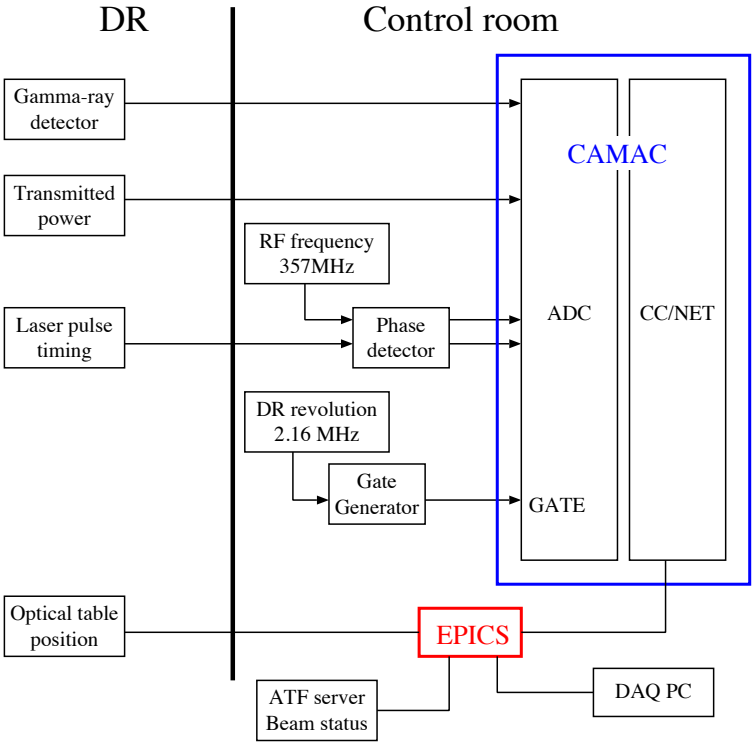

Figure 6.21: Data acquisition system

Chapter 7

Experimental results

7.1 Experimental procedure

The experiments were performed in single and 5 electron bunches per train. First we scanned the position of the optical table relative to the electron beam to find the optimum position between the lase pulses and the electron bunches by maximizing the counting rate of the laser-Compton scattering. At the same time, the timing of laser pulses relative to electron bunches was adjusted by changing relative phase between the ATF master oscillator and laser pulses. The electron beam current in the DR during taking was recorded using DCCT. Fig. 7.1 shows observed energy in the detector while changing the relative phase. The enhancement of the energy deposit was clearly observed at particular phase which indicated photons from laser-Compton scattering. After fixing the timing of laser pulses with electron bunches, we scanned the vertical and horizontal position of the optical table again to maximize the number of generated gamma rays.

7.1.1 Laser beam position scan

Fig. 7.2 and Fig. 7.3 show the observed photon intensity as a function of the position of the laser beam in vertical and horizontal direction with the single bunch operation. The number of photons is normalized by the stored laser power and the electron beam current. The positions of laser beam were set at where we observed the maximum counting rate. The width of the vertical position scan was 16.8 µm in σ, which was the convolution of the size of the laser beam and the electron beam in vertical direction. Since the vertical size of the electron beam was estimated to be 10 ± 1 µm from the measured beam parameter of the ATF during the experiment, the laser beam waist size in vertical direction was estimated to be $\sqrt{16.8^2 - 10^2} = 13$ µm, which is consistent with the estimation in Section 5.6.

7.1.2 Timing of laser pulse scan

Fig. 7.4 shows the number of photons as a function of laser pulse timing with the single bunch operation. The laser pulse timing was set the mean value of the Gaussian distribution to the time of the maximum counting rate. The width

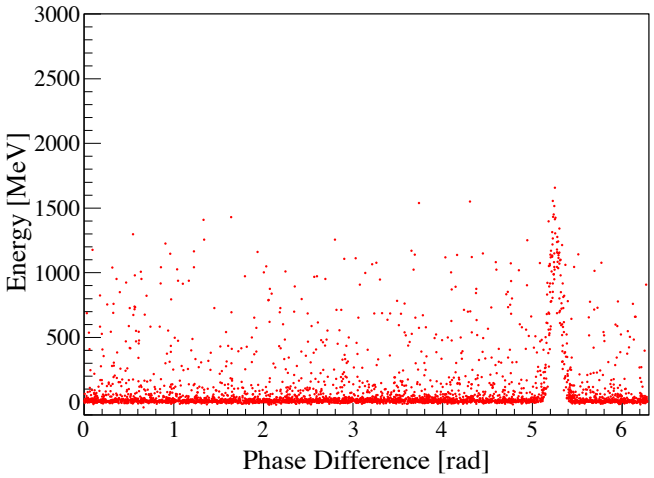

Figure 7.1: Compton signal versus phase difference between the ATF master clock and the laser oscillator. The enhancement of the energy deposit was observed at around 5.25 rad.

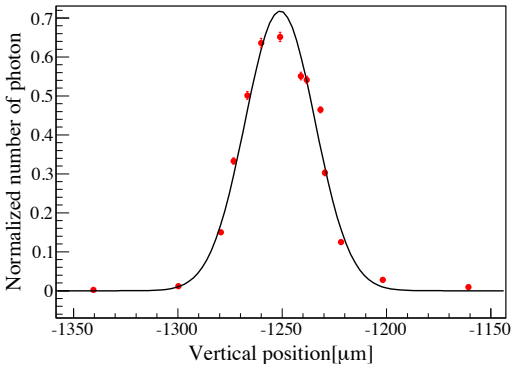

Figure 7.2: Vertical position scan with single bunch operation.

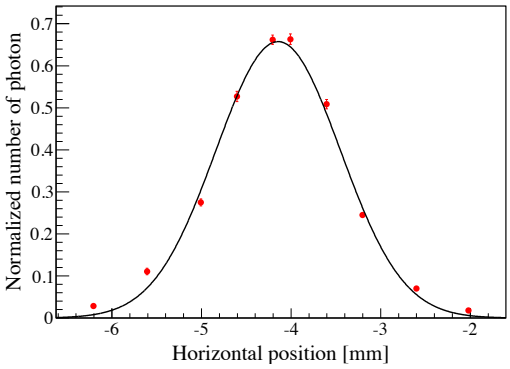

Figure 7.3: Horizontal position scan with single bunch operation.

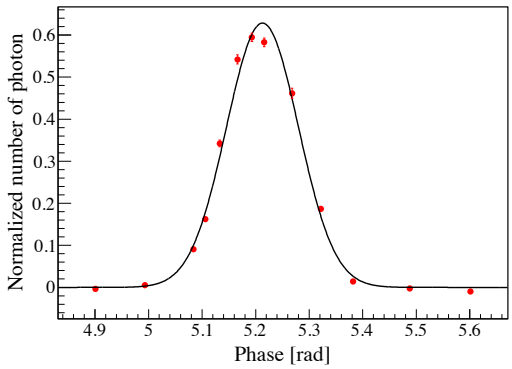

Figure 7.4: Timing of laser pulse scan with single bunch operation.

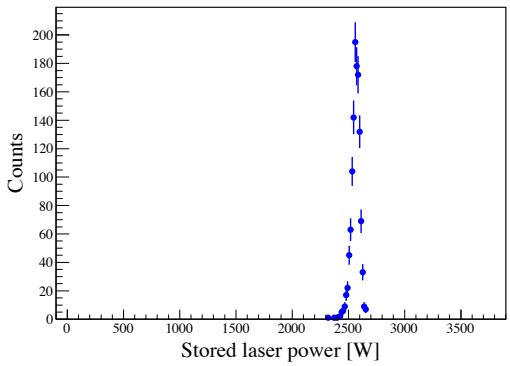

Figure 7.5: Distribution of stored laser power in the optical cavity.

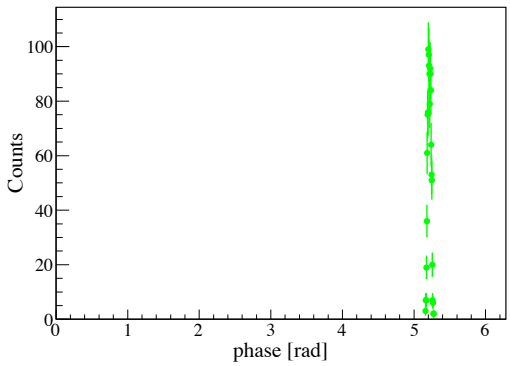

Figure 7.6: Distribution of the laser pulse timing.

of distribution was 0.0673 rad which corresponds to 30.0 ps in σ, which was the convolution of the longitudinal length of the laser pulse and electron bunch.

7.1.3 Measurement of the stored laser power

The stored laser power in the cavity during the experiment is shown in Fig. 7.5. It was 2.6 kW in average with the fluctuation of 37 W. From the width (FWHM) of the resonance of the cavity, the optical path was controlled with the precision of about 4 pm while its total length is 1.68 m. A distribution of laser pulse timing is shown in Fig. 7.6. The RMS timing jitter was estimated to be 9.7 ps. An effective length of the laser pulse was estimated to be $\sqrt{5^2 + 9.7^2} = 10.9$ ps, which is sufficiently smaller than the electron bunch length of 20 ps.

7.2 Number of gamma rays

Fig. 7.7 and Fig. 7.8 show the energy distribution observed by the photon detector with the single bunch and 5 bunch operation, respectively. In the single bunch operation, the average energy was 798 ± 6 MeV per collision. And in the 5 bunch operation, the average energy was 2970 ± 20 MeV per collision. Since the average

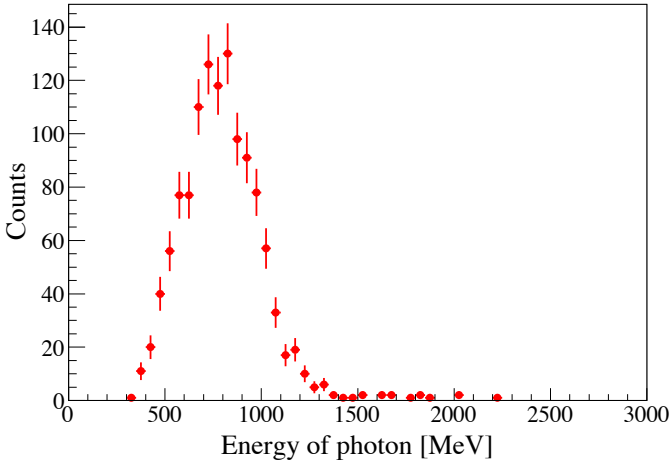

Figure 7.7: Energy distribution of observed photon in the detector with single bunch/train operation.

Table 7.1: Summary of experimental results and conditions.

Number of bunches	e^- current [mA]	Laser power [kW]	Number of photons [1/train]	Simulation [1/train]
1	2.3	2.5	33.3±0.3	33
5	8.1	2.6	123.8±0.8	123

energy of single photon in the detector is 24 MeV, the total energy corresponds to observation of 124 ± 1 photons per 5 bunches in the detector. Taking the revolution of the electron beam in the ATF ring into account, it corresponds to 2.7×10^8 photons per second. The results of the experiment are summarized in Table 7.1. The expected yield of photons, shown as "simulation" in the table, were calculated by the simulation code CAIN [35]. Parameters for the numerical simulation are summarized in Table 7.2. The waist sizes of the laser beam was estimated from measured profile of transmitted light from M_2 (Fig. 5.11(b)) and the transfer matrix described in Section 3.2. The expected yield of photons has a systematic error of 5% from the ambiguity of the estimate of laser waist sizes. The photon yield was consistent with the CAIN simulation for 1 and 5 bunches operation.

7.3 Bunch by bunch measurement

Since it is an important issue for the ILC positron source to generate multi-bunch gamma rays with stable intensity, we observed investigated the number of gamma rays in bunch by bunch basis using the BaF_2 detector.

Fig. 7.9 shows the typical intensity of each electron bunch. The waveforms were obtained the beam position monitor (BPM) installed in the ATF-DR.

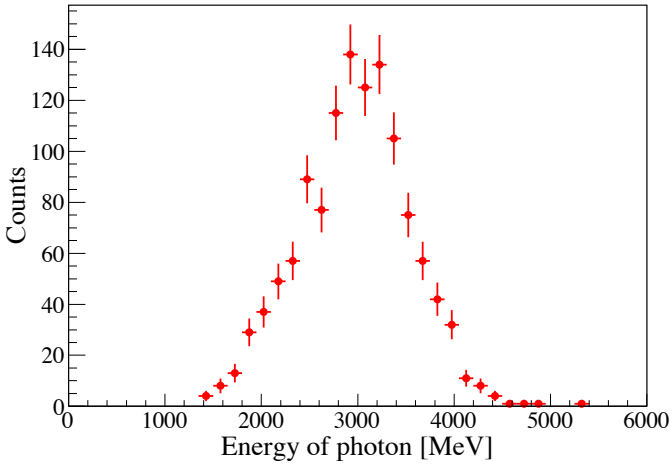

Figure 7.8: Energy distribution of observed photon in the detector with 5 bunches/train operation.

Table 7.2: Parameters of electron and laser beams.

Description	**Value**
Electron	
Beam intensity (1 bunch)	0.7×10^{10}
Beam intensity (5 bunches)	2.3×10^{10}
Beam size at IP (σ_x / σ_y)	110 / 9 µm
Bunch length (σ_z)	20 ps
Laser	
Spot size at IP (σ_{major} / σ_{minor})	27 / 10 µm
Pulse width (σ_z)	5 ps
Timing jitter of laser pulse	9–10 ps

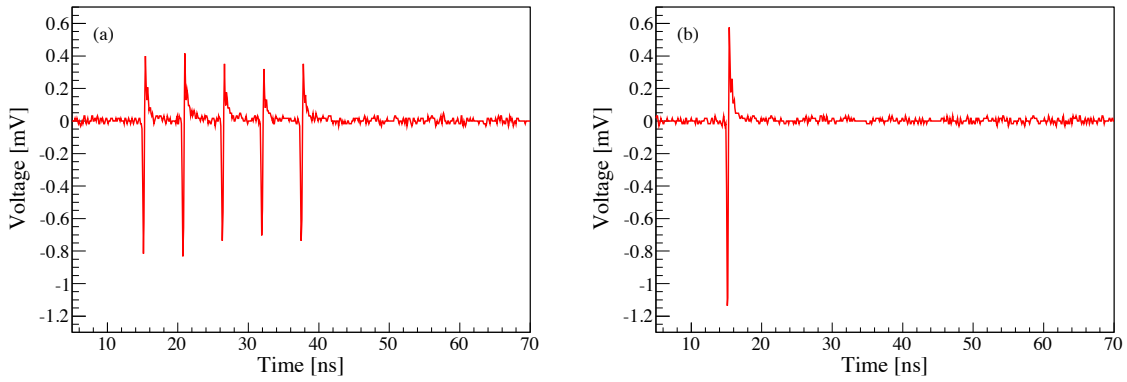

Figure 7.9: Typical intensity ratio of each electron bunch. (a) 5 bunches operation and (b) single bunch operation.

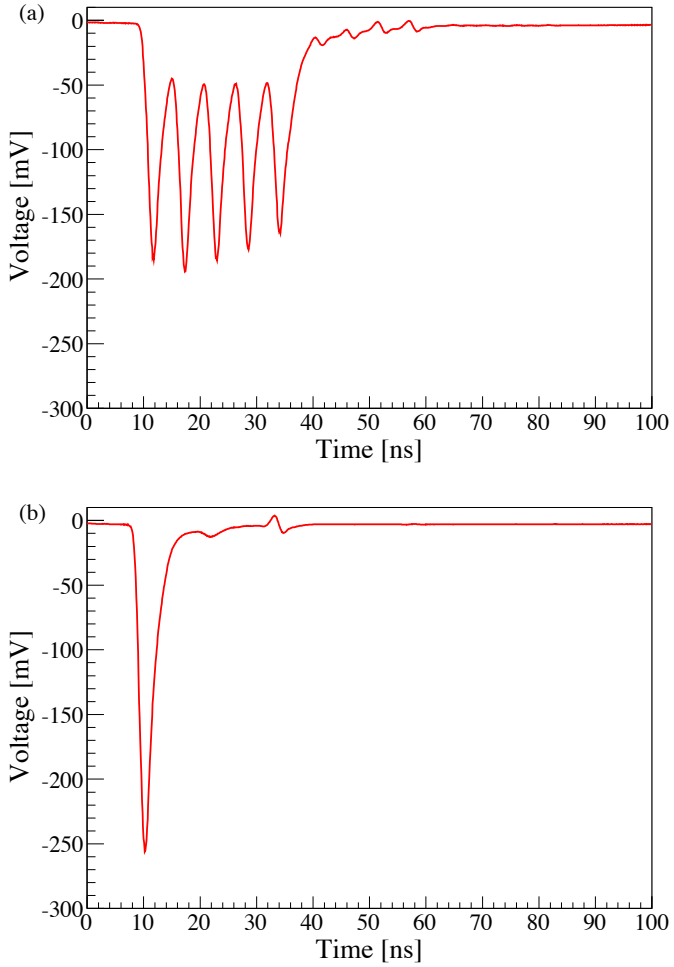

Figure 7.10: Typical waveform of gamma rays from each bunch in a train. (a) 5 bunches operation and (b) single bunch operation.

A typical waveform of gamma rays in the experiment are shown in Fig. 7.10, which are averages of 1000 collisions of laser pulses and a train of electron bunches. We clearly observed spikes of 5.6 ns separation in the waveform which corresponds to gamma ray from each bunch in a train. The amplitude of waveform can be converted into the energy in the BaF_2 detector using calibration factor of 3.16 MeV/mV. The number of gamma rays for 5 and single bunches operation were 117 photons/train and 33 photons/train, which are consistent with described in previous section.

Chapter 8

Conclusion

We studied gamma ray generation by laser-Compton scattering for as an R&D of the ILC polarized positron source. To increase the efficiency of laser-Compton scattering, we have studied the laser pulse stacking using a 3D 4-mirror optical resonant cavity. We installed the 3D 4-mirror cavity in the KEK-ATF and performed the experiment on gamma ray generation by laser-Compton scattering. The cavity consists of two flat mirrors and two concave mirrors. The reflectivity of the coupling mirror is 99.9% while those of the others are 99.99%. The average lase power of 2.6 kW was successfully accumulated in the cavity which corresponded to the power enhance factor of 1200. The fluctuation of stored power of 1.5% indicated that the length of the optical path in the system was controlled with the precision of about 4 pm. The laser beam spot sizes in its major and minor axis are estimated to be 27 µm and 10 µm respectively. The average of 124 ± 1 photons per collision was generated in the detector acceptance by laser-Compton scattering in the 5 bunch operation of the ATF. It corresponded to the photon intensity of 2.7×10^8 photons per second.

Toward the ILC positron source, the requirement of enhancement factor of a optical cavity for Compton scheme is approximately 10^4 which is about ten times higher than present status. We plan to replace mirrors of the cavity with higher reflectivity aiming at finesse of 30000 or more. The current performance of the feedback system has shown to be sufficiently stable for the finesse of more than one order of magnitude higher. However the thermal effect is a important issue for the mirrors because of the large stored power in the cavity. We will set up a system to investigate the loss of the mirror prior to the installation and also a clean environment to handle high reflectivity mirrors in the accelerator facility.

In conclusion, we successfully demonstrated the improvement of photon generation using the 3D 4-mirror cavity. We also first demonstrated a feedback scheme which utilized the polarization feature of the 3D 4 mirror cavity and succeeded to control the optical path of the system with the accuracy of 4pm. As for the development for the ILC positron source, more than order of improvement is reacquired but it is expected to be within the reach of future R&D using available high performance mirrors.

Acknowledgments

この論文を執筆するにあたり、多くの方々にご協力頂きました。ここに深くお礼申し上げます。

本研究の機会を与えてくださった広島大学 高エネルギー物理学研究室 高橋徹准教授、高エネルギー加速器研究機構 浦川順治教授、同 大森恒彦講師には温かいご指導を頂きました。感謝申し上げます。

三好修平氏、田中龍太氏、片岡裕美氏はコンプトングループのメンバーとして共に実験を行い、非常にお世話になりました。ありがとうございました。

本田洋介氏、清水洋孝氏、坂上和之氏、福田将史氏、荒木栄氏には共振器開発において様々な助言をいただきました。感謝致します。

I would like to thank LAL collaborators:Didier Jehanno-san, Nicolas Delerue-san, Iryna Chaikovska-san and others.

ATF の照沼信浩准教授、奥木敏行助教、内藤孝氏には ATF で実験を行う際にサポートして頂きました。さうび 高野幹夫氏にはレーザーの調整でお世話になりました。関東情報、アイワック、アシストエンジニアリングの皆様には現場作業をはじめいろいろな面で助けて頂きました。

広島大学 高エネルギー物理学研究室の飯沼昌隆助教や後輩の皆様にもサポートして頂きました。感謝致します。

最後に、これまで支えてくれた両親に感謝致します。

Bibliography

[1] C. Utfeld, S. R. Giblin, J. W. Taylor, J. A. Duffy, C. Shenton-Taylor, J. Laverock, S. B. Dugdale, M. Manno, C. Leighton, M. Itou, and Y. Sakurai. Bulk Spin Polarization of $Co_{(1-x)}Fe_x\mathbf{S}_2$. *Phys. Rev. Lett.*, 103:226403, 2009.

[2] A. Momose, S. Kawamoto, I. Koyama, Y. Hamaishi, K. Takai, and Y. Suzuki. Demonstration of X-Ray Talbot Interferometry. *Jpn. J. Appl. Phys.*, 42:L866, 2003.

[3] A. Bienenstock and H. Winick. Synchrotron radiation. In S. P. Parker, editor, *McGraw-Hill Encyclopedia of Physics*. McGraw-Hill, 1993.

[4] Spring-8 web site. `<http://www.spring8.or.jp/>`.

[5] M. Fukuda, T. Aoki, K. Dobashi, T. Hirose, T. Iimura, Y. Kurihara, T. Okugi, T. Omori, I. Sakai, J. Urakawa, and M. Washio. Polarimetry of short-pulse gamma rays produced through inverse compton scattering of circularly polarized laser beams. *Phys. Rev. Lett.*, 91:164801, Oct 2003.

[6] T. Omori, M. Fukuda, T. Hirose, Y. Kurihara, R. Kuroda, M. Nomura, A. Ohashi, T. Okugi, K. Sakaue, T. Saito, J. Urakawa, M. Washio, and I. Yamazaki. Efficient propagation of polarization from laser photons to positrons through compton scattering and electron-positron pair creation. *Phys. Rev. Lett.*, 96:114801, Mar 2006.

[7] S. Miyoshi, T. Akagi, S. Araki, Y. Funahashi, T. Hirose, Y. Honda, M. Kuriki, X. Li, T. Okugi, T. Omori, G. Pei, K. Sakaue, H. Shimizu, T. Takahashi, N. Terunuma, J. Urakawa, Y. Ushio, and M. Washio. Photon generation by laser-compton scattering at the kek-atf. *Nucl. Inst. Meth. A*, 623(1):576–578, 2010.

[8] S. Miyoshi. *Development of a Polarized Positron Source by laser Compton Scattering using an Optical Resonant Cavity.* PhD thesis, Hiroshima University, 2011.

[9] F. Zomer, Y. Fedala, N. Pavloff, V. Soskov, and A. Variola. Polarization induced instabilities in external four-mirror fabry-perot cavities. *Appl. Opt.*, 48:6651–6661, 2009.

[10] G. Aad et al. [ATLAS Collaboration]. Observation of a new particle in the search for the Standard Model Higgs boson with the ATLAS detector at the LHC. *Phys. Lett. B*, 716:1, 2012.

[11] S. Chatrchyan et al. [CMS Collaboration]. Observation of a new boson at a mass of 125 GeV with the CMS experiment at the LHC. *Phys. Lett. B*, 716:30, 2012.

[12] P. Burrows, J. Carwardine, E. Elsen, B. Foster, M. Harrison, H. Hayano, N. Phinney, M. Ross, N. Toge, N. Walker, A. Yamamoto, and K. Yokoya. ILC TDR Final DRAFT, 2012.

[13] Ilc newsline. `<http://newsline.linearcollider.org/>`.

[14] G. Moortgat-Pick et al. Polarized positrons and electrons at the linear collider. *Phys. Rep.*, 460:131–243, 2008.

[15] T. Nishitani, T. Nakanishi, M. Yamamoto, S. Okumi, F. Furuta, et al. Highly polarized electrons from GaAs–GaAsP and InGaAs–AlGaAs strained-layer superlattice photocathodes. *J. Appl. Phys.*, 97(9):094907, 2005.

[16] J. Beringer et al. (Particle Data Group). Review of particle physics. *Phys. Rev. D*, 86:010001, Jul 2012.

[17] B. M. Kincaid. A short-period helical wiggler as an improved source of synchrotron radiation. *J. Appl. Phys.*, 48(7):2684, 1977.

[18] S. Araki, Y. Higashi, Y. Honda, Y. Kurihara, M. Kuriki, et al. Conceptual design of a polarised positron source based on laser Compton scattering. *KEK Preprint 2005-60, CLIC Note 639*, 2005.

[19] M. Kuriki, S. Araki, Y. Higashi, Y. Honda, Y. Kurihara, et al. ILC Positron Source Based on Laser Compton. *AIP Conf. Proc.*, 980:92, 2008.

[20] M. Kuriki. Compton based e+ sources for ILC/CLIC. POSIPOL 2010, 2010.

[21] E. N. Hatch. Compton effect. In S. P. Parker, editor, *McGraw-Hill Encyclopedia of Physics*. McGraw-Hill, second edition, 1993.

[22] R. D. Evans. Compton Effect. In *Handbuch der Physik*, volume 34. Springer-Verlag, Berlin, 1958.

[23] T. Suzuki. General Formulas of Luminosity for Various Types of Colliding Beam Machines. KEK Preprint 76-3, 1976.

[24] A. E. Siegman. *LASERS*. University Science Books, 1986.

[25] A. Yariv and P. Yeh. *Photonics: Optical Electronics in Modern Communications*. Oxford University Press, sixth edition, 2006.

[26] F. A. Jenkins and H. E. White. *Fundamentals of Optics*. McGraw-Hill, fourth edition, 1976.

[27] W. W. Chow, J. Gea-Banacloche, L. M. Pedrotti, V. E. Sanders, W. Schleich, and M. O. Scully. The ring laser gyro. *Rev. Mod. Phys.*, 57:61–104, Jan 1985.

[28] J. Alda, S. Wang, and E. Bernabeu. Analytical expression for the complex radius of curvature tensor Q for generalized gaussian beams. *Optics Communications*, 80:350–352, 1991.

[29] D. Onciul. ABCD propagation law for misaligned general astigmatic Gaussian beams. *J. Opt.*, 23:163, 1992.

[30] J. A. Arnaud and H. Kogelnik. Gaussian Light Beams with General Astigmatism. *Appl. Opt.*, 8(8):1687–1693, Aug 1969.

[31] S. J. M. Habraken and G. Nienhuis. Modes of a twisted optical cavity. *Phys. Rev. A*, 75:033819, Mar 2007.

[32] A. Variola, F. Zomer, E. Bulyak, P. Gladkikh, V. Skomorokhov, T. Omori, and J. Urakawa. Luminosity optimization schemes in Compton experiments based on Fabry-Perot optical resonators. *Phys. Rev. ST Accel. Beams*, 14:031001, Mar 2011.

[33] Y. Honda, H. Shimizu, M. Fukuda, T. Omori, J. Urakawa, K. Sakaue, H. Sakai, and N. Sasao. Stabilization of a non-planar optical cavity using its polarization property. *Opt. Commun.*, 282(15):3108–3112, 2009.

[34] F. Hinode et al. ATF Accelerator Test Facility Design and Study Report. KEK Internal 95-4, 1995.

[35] K. Yokoya. User's manual of cain. `<http://lcdev.kek.jp/~yokoya/CAIN/Cain242/>`.

[36] T. A. DeVol, D. K. Wehe, and G. F. Knoll. Evaluation of wavelength shifters for spectral separation of barium fluoride emissions. *Nuclear Instruments and Methods in Physics Research Section A: Accelerators, Spectrometers, Detectors and Associated Equipment*, 348(1):156–162, 1994.

[37] Epics web site. `<http://www.aps.anl.gov/epics/>`.

公表論文

Development of a three dimensional four mirror optical cavity for laser-Compton scattering
T. Akagi, S. Araki, Y. Funahashi, Y. Honda, H. Kataoka, T. Kon, S. Miyoshi, T. Okugi, T. Omori, K. Sakaue, H. Shimizu, T. Takahashi, R. Tanaka, N. Terunuma, J. Urakawa, M. Washio and H. Yoshitama
Nuclear Instruments and Methods in Physics Research Section A **724,** 63-71 (2013).

Nuclear Instruments and Methods in Physics Research A 724 (2013) 63–71

Contents lists available at SciVerse ScienceDirect

Nuclear Instruments and Methods in Physics Research A

journal homepage: www.elsevier.com/locate/nima

Development of a three dimensional four mirror optical cavity for laser-Compton scattering

T. Akagi [a,*], S. Araki [b], Y. Funahashi [b], Y. Honda [b], H. Kataoka [d], T. Kon [d], S. Miyoshi [a], T. Okugi [b], T. Omori [b], K. Sakaue [c], H. Shimizu [b], T. Takahashi [a], R. Tanaka [a], N. Terunuma [b], J. Urakawa [b], M. Washio [c], H. Yoshitama [a]

[a] Graduate School of Advanced Sciences of Matter, Hiroshima University, Higashi-Hiroshima, Hiroshima 739-8530, Japan
[b] High Energy Accelerator Research Organization (KEK), Oho 1-1, Tsukuba, Ibaraki 305-0801, Japan
[c] Research Institute for Science and Engineering, Waseda University, Okubo 3-4-1, Shinjuku-ku, Tokyo 169-8555, Japan
[d] Graduate School of Science and Technology, Seikei University, Musashino-shi, Tokyo 180-8633, Japan

ARTICLE INFO

Article history:
Received 24 January 2013
Received in revised form
10 April 2013
Accepted 23 April 2013
Available online 30 April 2013

Keywords:
Compton
Optical cavity
Non-planar cavity
Pulse laser stacking
ILC
Polarized positron source

ABSTRACT

This paper describes a design and performance of a three-dimensional 4-mirror optical cavity for development of intense photon sources by laser-Compton scattering. We achieved the finesse of 4000 and average power of 2.6 kW in the cavity with the vertical laser beam spot size of 13 ± 1 μm in σ at the laser–electron interaction point. As a result, we observed 124 ± 1 photons with average energy of 24 MeV per beam crossing, which corresponds to the generation of 2.7×10^8 photons per second.

1. Introduction

Photon sources operating by means of reflecting laser photons off high energy electron beams (here after laser-Compton scattering or scheme) attract us due to their compactness, quasi-monochromaticity, polarizability etc. and are expected to be applied in fields such as high energy physics, biological science, material science and medical science. The advantages of the laser-Compton scheme are to generate high energy photons with relatively low energy electrons compared to the synchrotron radiation and to generate/control polarized photons. For example, O(10 MeV) photon can be generated with the O(1 GeV) electron by laser-Compton scattering. By utilizing these features, a compact photon source based on laser-Compton scattering can be achieved. However making intense photons for practical applications is a key issue for this scheme. A straightforward way to make intense photon sources is using a high power laser system to increase efficiency of laser-Compton scattering. However this brute force method would spoil an advantage of laser-Compton scattering, i.e., compactness. Another scheme to increase the intensity of the laser beam is to accumulate laser pulses in an optical resonant cavity in which laser pulses are coherently stacked so that the intensity is effectively increased. For this purpose, we developed a high energy photon generation system using an optical resonant cavity at the KEK-ATF electron ring aiming to develop a polarized positron source for the International Linear Collider (ILC) [1,2].

In previous studies, we achieved a finesse of 1800 with a waist size of 30 μm in σ at the focal point with the 2-mirror Fabry-Perot cavity and succeeded in generating photons by laser-Compton scattering [3,4]. However, the photon intensity needs further enhancement to meet the requirement of the ILC positron source. In terms of optical cavities, it is difficult to improve the finesse and focusing of the laser beam simultaneously with a 2-mirror Fabry-Perot cavity (see Section 2). Therefore, we developed a 4-mirror ring cavity to achieve higher finesse and smaller waist size simultaneously. In addition, we found that the laser beam profile in the cavity is astigmatic and is not ideal for laser–electron interaction when all 4 mirrors are placed in the same plane [5]. We designed a cavity with 3 dimensional (3D) mirror configuration to avoid the astigmatic profile.

In this paper, we describe features of the 3D 4-mirror cavity in Section 2. Section 3 is devoted to the design of the cavity. The

* Corresponding author. Tel./fax: +81 82 424 7037.
E-mail address: tomoya-akagi@hiroshima-u.ac.jp (T. Akagi).

0168-9002/$ - see front matter © 2013 Elsevier B.V. All rights reserved.
http://dx.doi.org/10.1016/j.nima.2013.04.066

performance of the cavity and results of laser-Compton experiments are described in Sections 4 and 5, respectively.

2. Property of the 3D 4-mirror cavity

In general, the length of the round-trip optical path L of the resonant cavity must satisfy the relation $L=n\lambda$, where n and λ are an arbitrary integer and the wave length of the laser, respectively. To reduce the laser beam waist in a 2-mirror Fabry-Perot cavity, it has to be a concentric type, i.e., the curvature radius of mirrors, ρ, must be as close as reasonable to the half of the distance between the mirrors, D. The result is that the 2-mirror cavity is unstable against the misalignment of mirrors as illustrated in Fig. 1(a) and (c). In a 4-mirror cavity consisting of two plane mirrors and two concave mirrors, it is possible to configure mirrors such that virtually parallel laser beams can be incident upon concave mirrors (see Fig. 1(b) and (d)). Thus one can get a smaller beam waist in the 4-mirror cavity with confocal optics (ρ~D), which is more tolerant of misalignment of mirrors than concentric optics.

In the case of a planar 4-mirror cavity, where all 4 mirrors of the 4-mirror cavity are placed in the same plane (the tangential plane), the effective focal length in the plane f_t, and in the plane perpendicular to the tangential plane (the sagittal plane) f_s, is different (see Fig. 2(a)) [6]. This causes astigmatism at the focal point between the two concave mirrors:

$$f_t=\frac{\rho}{2}\cos\alpha \tag{1}$$

$$f_s=\frac{\rho}{2\cos\alpha}. \tag{2}$$

Because of the astigmatism, the laser beam profile inside the planar 4-mirror cavity is an ellipse and is not suitable for maximizing the laser-Compton scattering efficiency.

A solution to avoid the astigmatism is to make f_t and f_s equal by twisting the optical path in the cavity, i.e., making a 3D 4-mirror cavity. Fig. 2 shows a schematic of a planar and a 3D cavity.

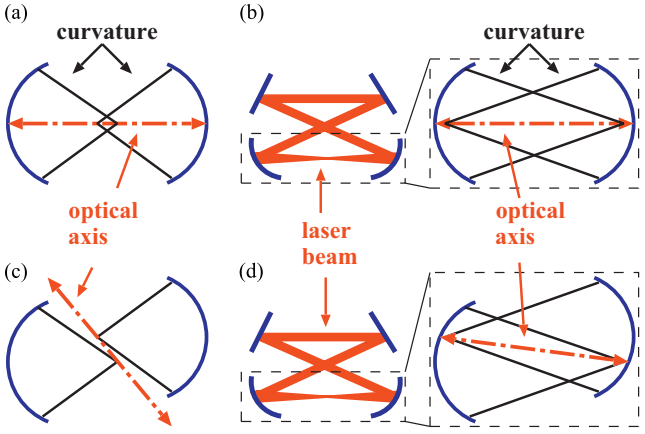

Fig. 1. The illustration of optical configuration of 2 mirror and 4 mirror cavities. The concentric configuration for the 2 mirror case (a) and confocal configuration (b). The effects of misalignment for 2 mirror case (c) and 4 mirror case (d).

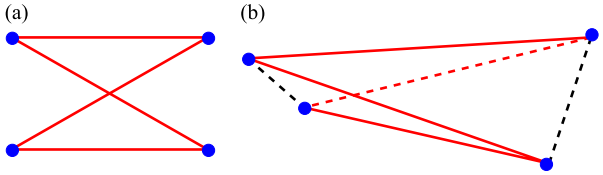

Fig. 2. The schematic of mirror configuration for planar (a) and 3D 4-mirror (b) cavities.

Calculated waist sizes of the laser beam around the laser–electron interaction point for a planar and for a 3D 4-mirror cavity are shown in Fig. 3(a) and (b), respectively. In the calculation, it is assumed that the distance between concave mirrors is the same for both configuration. In a 3D 4-mirror cavity, laser beam profile is rounder at the laser–electron interaction point compared to a planar cavity. Therefore we adopted Fig. 3(b) configuration. Details of the design and the laser beam profile in the 3D 4-mirror cavity are described in Section 3. The general discussion on stability of various four-mirror cavities is found in Ref. [5].

2.1. Polarization dependence of the 3D 4-mirror cavity

Since the laser light travels a twisted path in the 3D 4-mirror cavity, the optical state in the cavity acquires a geometric phase during the propagation. This causes a rotation of the polarization axis for linearly polarized states or an additional phase for circularly polarized states. Fig. 4 shows the geometric phase caused by reflection at mirror M_{i-1} and M_i [7]. Let $\vec{n}_i$ be normal vector to the mirror M_i. The vector $\vec{a}_i$ can be defined as

$$\vec{a}_i=\frac{\vec{n}_i\times\vec{k}_i}{|\vec{n}_i\times\vec{k}_i|} \tag{3}$$

where k_i being wave vector of the laser light. Then the geometric phase at reflection on mirrors M_{i-1} and M_i is

$$\cos\theta_i=\vec{a}_i\cdot\vec{a}_{i-1}. \tag{4}$$

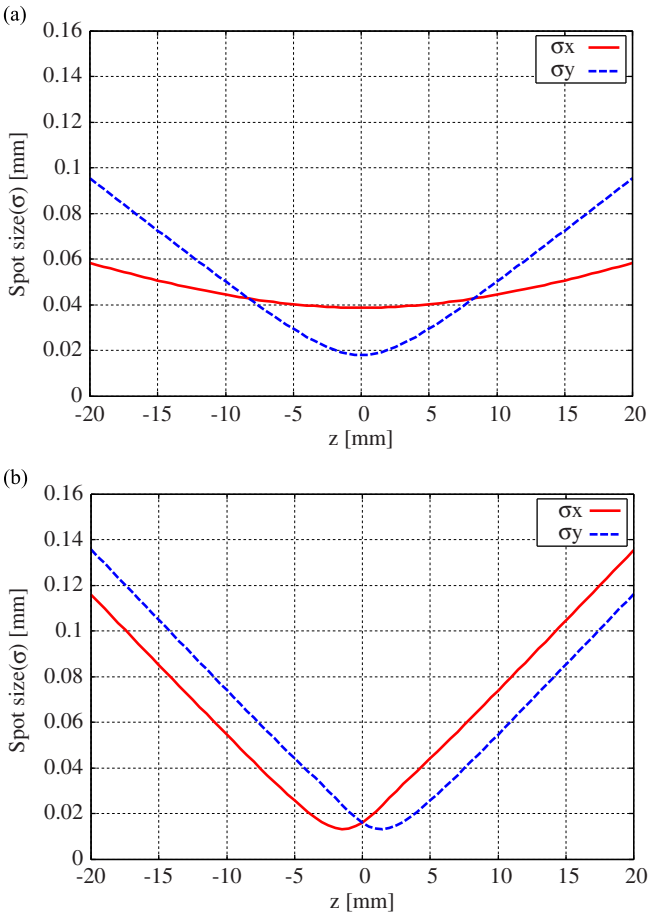

Fig. 3. (a) The spot size of laser beam (σ) of a planar cavity. $z=0$ corresponds to the designed laser–electron interaction point. (b) The spot size of laser beam (σ) of the 3D 4-mirror cavity. At $z=0$ is, laser beam profile is rounder compared to the planar cavity at $z=0$.

The geometric phase for a round trip of the cavity is, $\sum\theta_i$, which is 6.31 rad for current design described in Section 3.

The effect of the geometric phase in the 3D 4-mirror cavity for the linearly polarized laser beam is that the direction of polarization shifts each round trip in the cavity. Therefore the 3D 4-mirror cavity does not resonate with linearly polarized laser beams. On the other hand, the effect on the circularly polarized laser beam is a constant phase shift of the optical state which corresponds to a shift of the length of the optical path, i.e., length of the cavity. It should be noted that the sign of the phase shift is opposite for the left and right polarization. Thus the 3D 4-mirror optical cavity only resonates separately with the left or right circularly polarized laser beam at different optical path lengths.

3. Design of the 3D 4-mirror cavity

3.1. General parameters

The schematic of the mirror configuration of the 3D 4-mirror cavity is shown in Fig. 5. The distance between each mirror is 420 mm and the round trip optical path of the cavity, L, is 1680 mm which is chosen to match the bunch separation of the ATF electron beam. The distances of M_1–M_3 and M_2–M_4 are 70 mm and the all incident angles, α_i, are 4.8°. In Fig. 5, M_1 and M_2 are flat mirrors while M_3 and M_4 are concave mirrors. The curvature of the concave mirrors is 420 mm. We used the dielectric multi-layer mirrors provided by REO (Research Electro-Optics, Inc.). The specifications of mirrors are summarized in Table 1. The reflectivity of coupling mirror M_1 (which the laser beam is injected into) is 99.9% while the reflectivity of M_2, M_3 and M_4 is 99.99%. The finesse

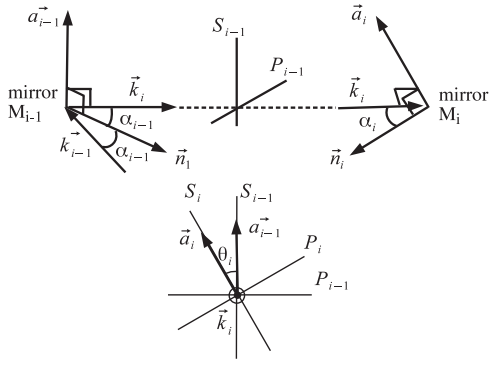

Fig. 4. Principle of the calculation of geometric phase by the mirror reflections [7]. k_i is wave vector of the laser light, $\vec{n}_i$ is normal vector to the mirror M_i, and θ_i is the geometric phase. Details are described in Section 2.1.

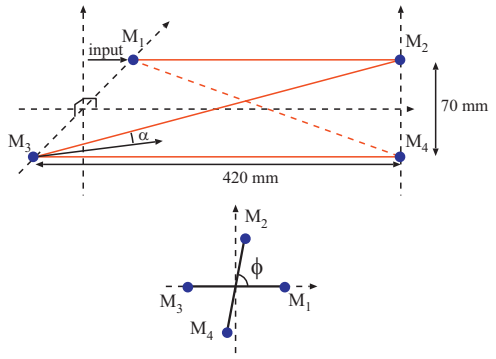

Fig. 5. Schematic of the 3D 4-mirror cavity. M_1 is the plane mirror where the laser beam is injected. ϕ represents the twisting angle of the cavity. $\phi = 90°$ in the original design.

Table 1
Specification of mirrors for the 3D 4-mirror cavity.

Description	Value
Substrate material	Fused silica
Diameter	25.4 mm
Scratch-dig	10–5
Reflectivity	
M_1	99.9%
M_2, M_3 and M_4	99.99%
Transmittance	
M_1	0.08%
M_2, M_3 and M_4	0.007%

F of the cavity is expressed as

$$F = \frac{\pi\sqrt{R}}{1-R} \tag{5}$$

where $R\ (=\sqrt{R_1R_2R_3R_4})$ is the effective reflectivity per round-trip. The finesse is calculated to be 4830.

3.2. Calculation of the laser propagation in the cavity

Propagation of the laser light along the optical path (z-axis) is, in general, expressed in terms of transverse coordinates x, y and angular divergences $\theta_x = \partial x/\partial z$, $\theta_y = \partial y/\partial z$. With the paraxial approximation ($\theta \ll 1$), propagation of the laser can be expressed as

$$\begin{pmatrix} x' \\ y' \\ \theta'_x \\ \theta'_y \end{pmatrix} = M_t \begin{pmatrix} x \\ y \\ \theta_x \\ \theta_y \end{pmatrix} \tag{6}$$

where M_t is a transfer matrix to express propagation of the laser via an optical path or a component. The transfer matrix for a free space over distance l can be expressed as

$$D(l) = \begin{pmatrix} 1 & 0 & l & 0 \\ 0 & 1 & 0 & l \\ 0 & 0 & 1 & 0 \\ 0 & 0 & 0 & 1 \end{pmatrix}. \tag{7}$$

The transformation through an astigmatic thin lens is given by

$$F(f_1, f_2) = \begin{pmatrix} 1 & 0 & 0 & 0 \\ 0 & 1 & 0 & 0 \\ -1/f_1 & 0 & 1 & 0 \\ 0 & -1/f_2 & 0 & 1 \end{pmatrix}. \tag{8}$$

The effect of the geometric phase can be incorporated by a rotation matrix as

$$R(\theta) = \begin{pmatrix} \cos\theta & \sin\theta & 0 & 0 \\ -\sin\theta & \cos\theta & 0 & 0 \\ 0 & 0 & \cos\theta & \sin\theta \\ 0 & 0 & -\sin\theta & \cos\theta \end{pmatrix} \tag{9}$$

where θ is the geometric phase acquired through the propagation. The transfer matrix to describe propagation of the laser beam for a round trip of the 3D 4-mirror cavity is in the form

$$\begin{aligned} M_t = {} & D(l/2)F(f_{t3}, f_{s3})R(\theta_3)R(\theta_2)R(\theta_1) \\ & D(3l)F(f_{t4}, f_{s4})R(\theta_4)D(l/2) \end{aligned} \tag{10}$$

where l is the distance between the mirrors (420 mm for current design). The transfer matrix starts and ends at the center of the two concave mirrors because the laser beam profile at this point (laser–electron IP) is of interest in the laser-Compton experiments. The matrix M_t has two eigenvalues which represent the round-trip

Gouy phase [8]. It reflects the fact that the laser beam profile in the cavity is an ellipse and has two eigen axes corresponding to major and minor ones.

Due to the three dimensional configuration of the path, the elliptical laser beam profile in the cavity rotates during propagation [9,10]. We optimized the configuration of mirrors of the cavity to maximize the efficiency of laser–electron interaction based on the calculation with the transfer matrix (Eq. (10)). The result of the calculation of the laser beam waist size at the laser–electron interaction point is shown in Fig. 6 as a function of the distance between two concave mirrors while keeping total length of the optical path constant. Fig. 7 shows the laser beam spot sizes in its major and minor axis along the propagation in the cavity. We found that the laser beam profile is elliptical in shape and is not optimized with the original design ($\phi = 90^\circ$ in Fig. 5) as shown in Fig. 6(a) and 7(a). We chose $\phi = 91.2^\circ$ to obtain stable resonant condition and a rounder profile with a smaller laser beam waist at the laser–electron interaction point. The design waist size is 15 μm (σ) at the interaction point.

3.3. The feedback control system

The picture of the constructed 3D 4-mirror cavity is shown in Fig. 8. The mirror holders of M_1 and M_4 have two directional tilting mechanisms for initial alignment of mirrors. Piezo actuators were attached to the mirror M_2 and M_3 via a leaf spring as shown in Fig. 9. The length of piezo actuators is 15 mm and 70 mm for M_3 and M_2, respectively.

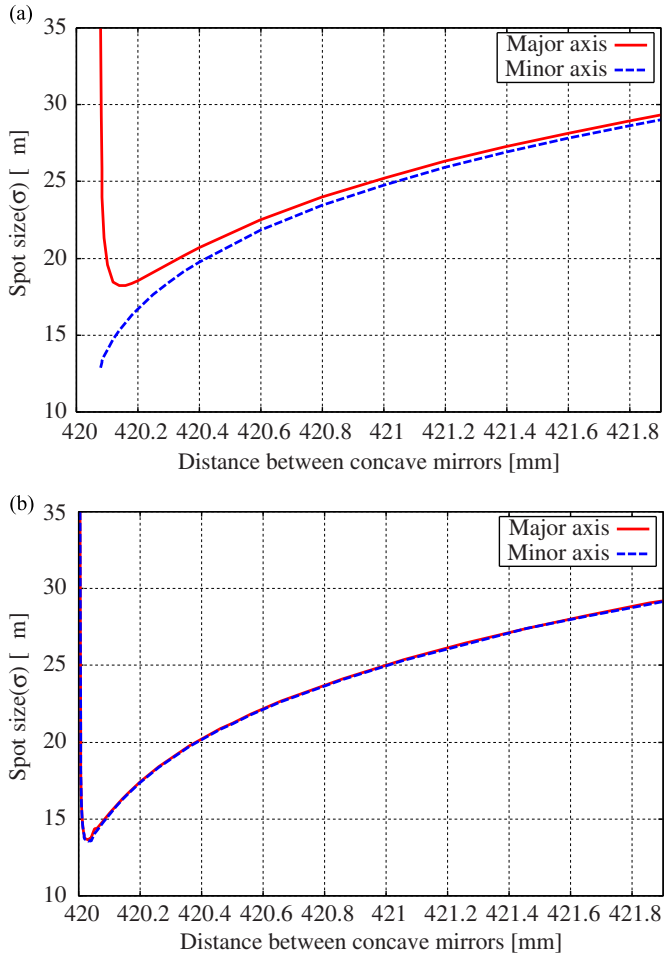

Fig. 6. The spot size of laser beam in major axis and in minor axis at the collision point as function of the distance between concave mirrors. (a) $\phi = 90^\circ$ and (b) $\phi = 91.2^\circ$.

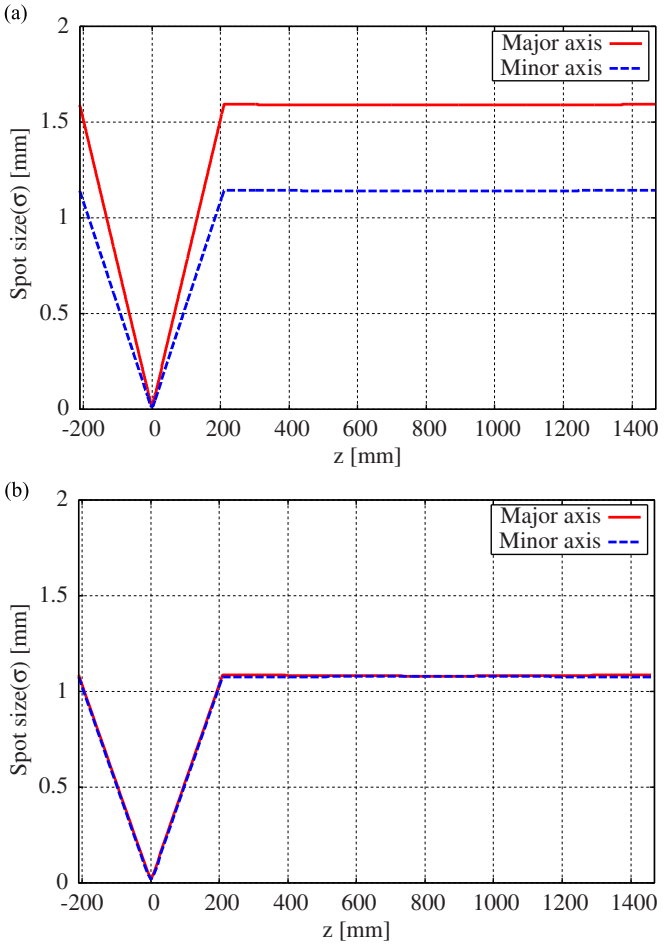

Fig. 7. The spot size of laser beam in major axis and in minor axis along the propagation in the cavity. (a) $\phi = 90^\circ$ and (b) $\phi = 91.2^\circ$.

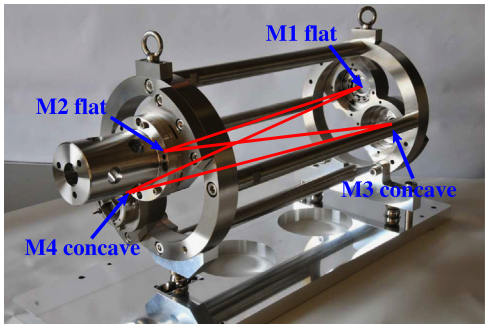

Fig. 8. The 3D 4-mirror cavity.

To accumulate laser pulses in the cavity and continuously make collisions of laser pulses with electron bunches, the optical path, L, of the cavity must be kept at the resonance condition ($L = n\lambda$) with a precision of $dL \ll \lambda/\text{enhancement} \sim 10^{-9}$ m and the timing of laser pulses and electron bunches must be synchronized within about 10 ps. The shorter piezo actuator of the optical cavity is used to synchronize the laser pulses with the electron pulses. The longer one is used for slow feedback, i.e., to adjust the length of the optical path to the circumference of ATF ring due to seasonal variation of ambient temperature. As the resonance condition

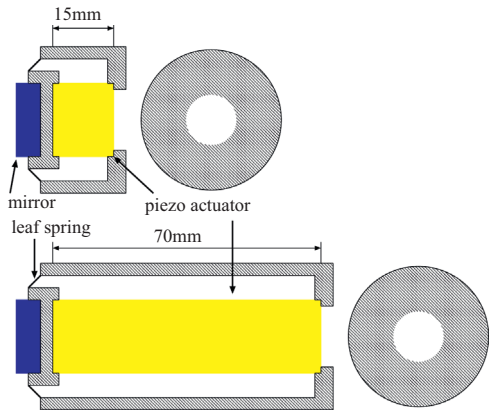

Fig. 9. Close view of mirror attachment with the piezo actuator. Two mirrors are attached to the piezo actuator via the leaf spring. The piezo actuator is cylindrical with a hole to let a laser beam go through.

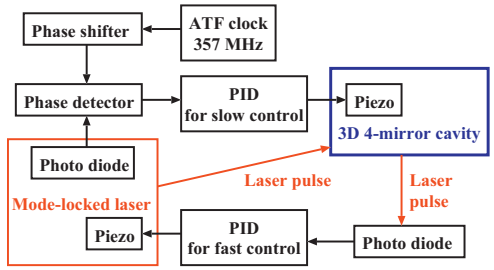

Fig. 10. The scheme of the feedback system for laser-Compton scattering.

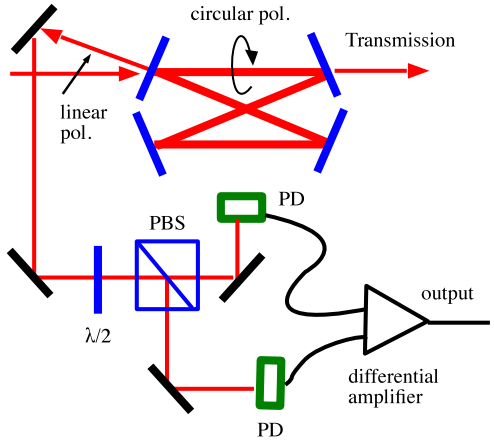

Fig. 11. The optical setup for the feedback system.

affects the synchronization and vice versa, the system could not be stable if we controlled these two conditions independently. Therefore we constructed a closed loop feedback system consisting of the resonance and synchronization signal as shown in Fig. 10. In the feedback loop, the resonance signal from the optical cavity was fed to the mode-locked laser, while the synchronization signal was fed into the shorter piezo actuator of the optical resonant cavity. Because resonance feedback needs relatively faster response than timing synchronization. Therefore, the piezo actuator inside the laser oscillator is used to keep the cavity on resonance.

We adopted a new scheme for the feedback control system, which utilized the polarization property of the 3D 4-mirror cavity [11]. The optical setup of the feedback system is shown in Fig. 11. In the system, a linearly polarized laser beam is injected into the cavity. As described in previous section, only the circularly

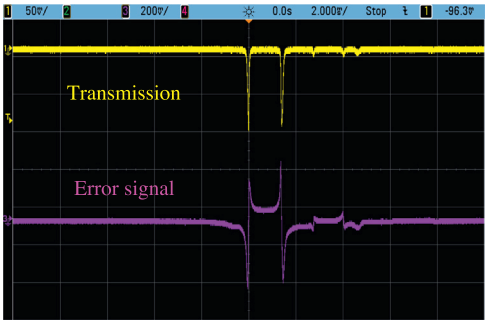

Fig. 12. The transmission and the error signal for the feedback system utilizing the polarization property of the 3D 4-mirror cavity.

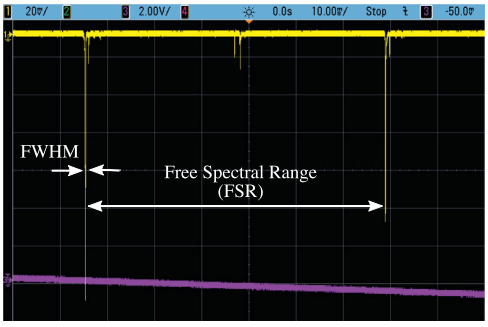

Fig. 13. The resonance peaks obtained by scanning the optical path of the cavity.

polarized component was fed into the cavity due to the geometric phase. The phase of the circular component depends on the resonance condition of the cavity and it eventually changes the direction of the linear polarization of reflected light from the coupling mirror. The direction of the polarization can be easily monitored using a Polarized Beam Splitter (PBS) and is used as the "error signal" of the feedback system. A typical error signal and intensity of the corresponding transmitted light, which is proportional to the stored laser power in the cavity, are shown in Fig. 12. The figure is obtained by scanning the optical path of the cavity. It is seen that the error signal is essentially the differentiation of the stored intensity.

4. Performance of the cavity and discussion

4.1. Finesse

Fig. 13 shows intensity of the transmitted light from M_4 while changing the length of the optical path L. A clear peak in the transmitted light was observed at the point where the cavity resonated with the incoming laser pulses. The finesse of the cavity could be measured by the ratio of Free Spectral Range (FSR) and FWHM width of the resonance and was

$$F = \frac{\mathrm{FSR}}{\mathrm{FWHM}} = 4040 \pm 420. \tag{11}$$

Since the typical width of the resonance was as small as 270 pm, the measurement was vulnerable with the external disturbances and fluctuated for each measurement. As a result, the finesse measured using this method had about a 10% error.

We also measured the finesse by the decay time of the stored laser power. Fig. 14 shows a measurement of the transmitted power in time after the laser injection was switched off by a Pockels cell. The time dependence was fitted with the function $P(t) = P\exp(-t/\tau) + C$ with P, τ and C being free parameters. The

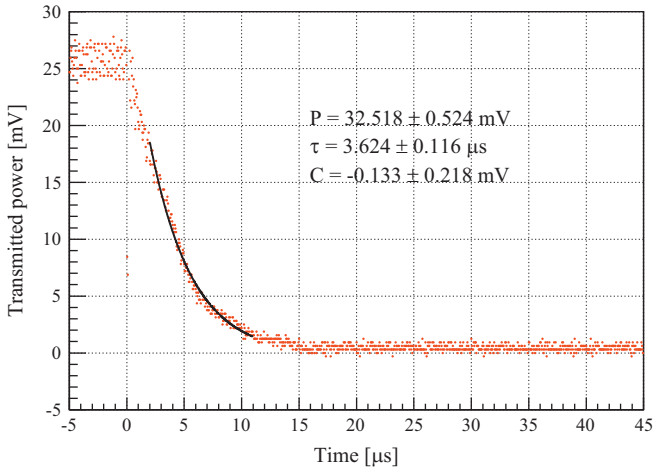

Fig. 14. The measurement of the decay time of the laser power in the cavity. The black line is the fitted curve with $P(t)=P\exp(-t/\tau)+C$, where P is the initial laser power, τ is the decay time and C is the offset. The decay time obtained by fitting is $\tau=3.6\pm0.1$ μs.

Table 2
The finesse of the 3D 4-mirror cavity.

Method	Finesse
Design	4830
Decay time method	4040 ± 110
Ratio of FSR and FWHM	4040 ± 420

finesse can be calculated as $F=2\pi c\tau/L$, where c is the light velocity in vacuum. The measured decay time was 3.6 ± 0.1 μs which corresponded to the finesse of 4000 ± 110. The results of finesse measurements are summarized in Table 2 with the design value. The two measurements were consistent each other but are smaller than the one expected from the reflectivity of mirrors. It appeared that effective reflectivity $R=\sqrt{R_1R_2R_3R_4}$ was down to 99.922%, possibly by a contamination, while it was expected to be 99.935% from the specification of mirrors.

4.2. Stored laser power in the cavity

The enhancement factor of the laser power in the optical cavity at resonance is estimated to be

$$\frac{P_s}{P_i}=\frac{T_1}{(1-R)^2} \tag{12}$$

where P_i is the input power into the cavity and P_s is the stored power in the cavity. The effective reflectivity R was estimated to be 0.99922 by Eq. (5) with the measured finesse of 4000. The transmittance T_1 of the coupling mirror M_1 was independently measured to be 0.074%. Therefore, power enhancement factor was estimated to be 1200.

In order to understand the consistency between input into, stored in and output from the cavity, we measured power balance of the cavity. The result of a typical measurement is shown in Fig. 15. Here we measured the transmitted and the reflected power long enough after turning on the feedback system, because rapid decrease in power was observed in the initial moment after turning on the feedback system (See, Section 4.4 in detail). When the cavity was off resonance, all power was reflected at the coupling mirror M_1 and was measured to be 6.6 W. When the cavity is on resonance, a part of incoming laser was injected into the cavity and reflected power reduced to 5.4 W. Since the cavity is designed such that reflected power drops zero at the resonance in

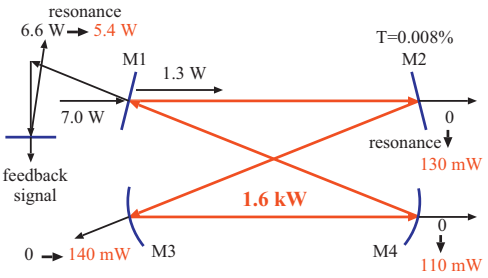

Fig. 15. Measurement of power balance of the cavity. The input, stored and transmitted power for the case that cavity is on/off resonance are shown (see text in detail).

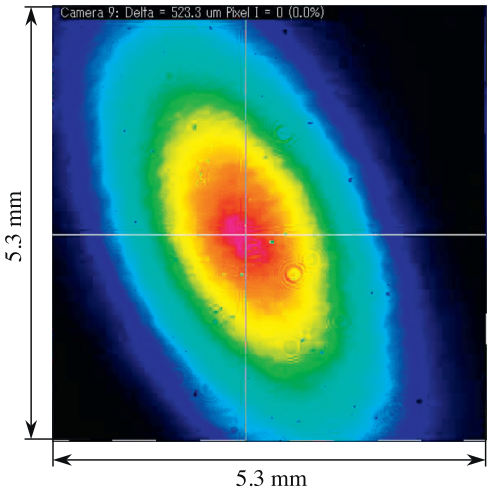

Fig. 16. The transmitted laser beam profile from mirror M_2.

ideal condition[1], the remaining reflected power at the resonance can be regarded as deviation of the coupling from the ideal condition. Hence, from the reflected power at the resonance and off resonance, the coupling was calculated to be (6.6−5.4)/6.6=0.18. It should be noted that the cavity can only resonates with circular polarized state, the coupling efficiency is 0.5 at the maximum for linearly polarized lasers. The transmitted power from M_2 was measured to be 130 mW and the transmittance of M_2, which was independently measured, was 0.008%. The stored power in the cavity was calculated to be $0.13/(8\times10^{-5})=1.6$ kW. On the other hand, the injected power into the cavity was calculated to be 1.3 W ($1.3=7.0\times0.18$) from the coupling efficiency and the power enhancement factor was estimated to be 1200. Then the stored power in the cavity was calculated to be $1.3\times1200=1.6$ kW, which was consistent with the estimate from the transmitted power and the transmittance of M_2.

Summation of the transmitted power from M_2, M_3 and M_4 was (0.13 + 0.14 + 0.11)~0.4 W, while the injected power to the cavity was estimated to be 1.3 W. The difference of the two, (1.3−0.4)~0.9 W, could be attributed to the power losses on the mirror. Assuming the same power loss ratio on each mirror, the power loss on each mirror was estimated as (0.9/4/1600)~100 ppm.

4.3. The effect of misalignment

The transmitted laser beam profile from the cavity is shown in Fig. 16. An elliptical beam profile was observed. It indicates that

[1] Here injection of circularly polarized light is assumed.

the laser beam profile at the laser–electron interaction point is also an ellipse despite the fact that the cavity was designed to obtain a rounder profile as described in Section 3.2.

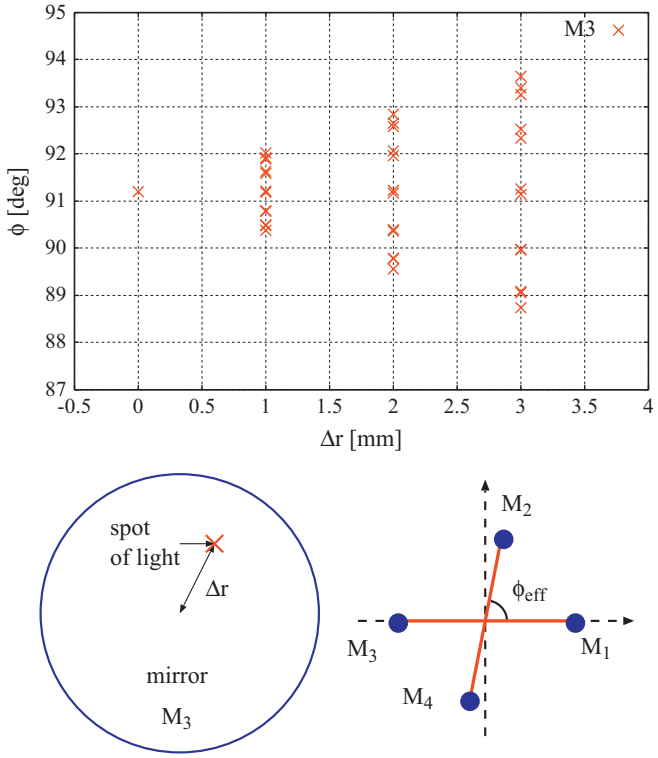

Fig. 17. The change of ϕ_{eff} as a function of the misalignment of the laser beam from the center of M_3.

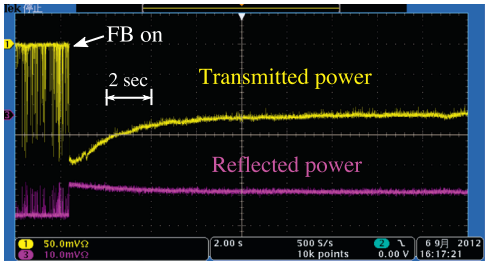

Fig. 18. The observation of stored power reduction after turning on the feedback system.

It is presumed that although the configuration of mirrors were designed to make a round profile of the laser beam by setting the twisted angle $\phi = 91.2^\circ$, the effective angle of the laser path ϕ_{eff} deviated from the designed value. For example, in Fig. 17, we show the change of ϕ_{eff} as a function of the distance of the spot of the light on the M_3 from its center. Since the only mirror holders of M_1 and M_4 had a tilting mechanism for alignment of mirrors, the angle ϕ_{eff} might not be equal to $\phi = 91.2^\circ$ and caused the elliptical profile of the laser beam. Because a round beam was injected into the cavity, it could be a reason for the low coupling efficiency described in previous section.

4.4. Possible thermal effect to the cavity

Fig. 18 shows the transmitted and reflected power from M_1 as a function of time after turning on the feedback system. We observed that the stored power in the cavity decreased to about a half after several seconds. Another observation was the difference of the laser beam profile at the resonance when scanning the length of the cavity and when turning on the feedback system as shown in Fig. 19. In Fig. 19(b), a distortion was observed in the profile, where the picture was taken after rapid decrease of the transmitted and the reflected power shown in Fig. 18. Since the decrease in the transmitted power and the distortion of the laser beam profile were not observed when the stored power in the cavity was low, it is suspected that thermal effects due to the power loss on the mirrors distorted the shape of mirrors. The distortion could be another reason for the small coupling efficiency in addition to the ϕ_{eff} described previously.

5. Experiment on photon generation at the KEK ATF

5.1. Experimental setup

The KEK-ATF is the Accelerator Test Facility to develop an ultra-low emittance electron beam required for the ILC [12]. The energy of the electron beam is 1.28 GeV and the revolution rate is 2.16 MHz. A bunch in the ATF beam contains about 10^{10} electrons and the accelerator is operative up to 10 bunches per train with the bunch separation of 5.6 ns. The experiment was performed in single and 5 bunches per train. The main parameters of the electron beam in the ATF are summarized in Table 3.

The 3D 4-mirror cavity was installed in the north straight section of the ATF in summer of 2011. The photon detector was placed 18 m downstream of the laser–electron interaction point, as shown in Fig. 20. We used a mode-locked pulsed laser (COUGAR,

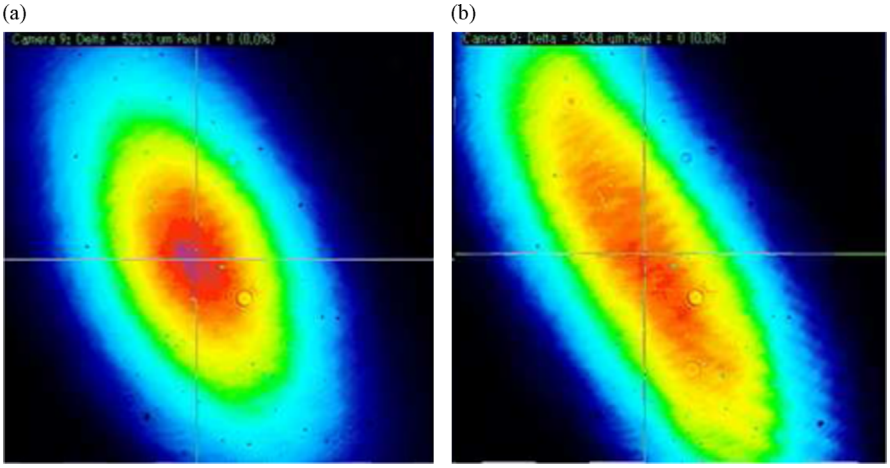

Fig. 19. (a) The transmitted laser beam profile from mirror M_2 when scanning the length of optical path (same as Fig. 16) and (b) the cavity is on resonance.

Table 3
Parameters of ATF damping ring.

Description	Value
Electron energy	1.28 GeV
Beam intensity	1×10^{10} e/bunch
Bunch spacing	5.6 ns
Emittance (ϵ_x/ϵ_y)	$1.1 \times 10^{-9}/12 \times 10^{-12}$ m rad
DR revolution	2.16 MHz

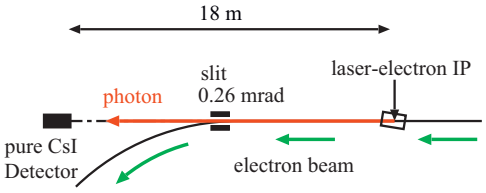

Fig. 20. The schematic view of the cavity and the photon detector. The 3D 4-mirror cavity is installed in the north straight section of the ATF damping ring. A pure CsI detector for photon detection is placed at 18 m downstream of the laser–electron interaction point.

Table 4
Parameters of the laser system.

Description	Value
Laser wavelength	1064 nm
Laser frequency	357 MHz
Laser pulse width	11 ps (FWHM)
Laser power	10 W (28 nJ/pulse)
Crossing angle	14°

Time-Bandwidth Products) whose wave length, repetition rate, average power were, 1064 nm, 357 MHz, and 10 W, respectively, as summarized in Table 4. The crossing angle of the laser and the electron beams was 14°, which determined the maximum energy of the photon at 28 MeV. The energy of the photons in the detector acceptance is 19–28 MeV with the average of 24 MeV, which was limited by the slit of 0.26 mrad aperture placed between the laser–electron interaction point and the detector.

5.2. Experimental procedure and results

In the experiment, the timing of laser pulses relative to electron bunches was adjusted by changing relative phase between the ATF master oscillator and laser pulses. Fig. 21 shows the observed energy in the detector while changing the relative phase. The enhancement of the energy deposit was clearly observed at particular phase which indicated photons from laser-Compton scattering.

Number of photon as a function of the vertical position of the laser beam with respect to the electron beam axis in 5 bunches mode is shown in Fig. 22. The width of the distribution was 16.8 μm in σ, which was the convolution of the size of the laser beam and the electron beam in vertical direction. Since the vertical size of the electron beam was estimated to be 10 ± 1 μm from the measured beam parameter of the ATF during the experiment, the laser beam waist size in vertical direction was estimated to be $\sqrt{16.8^2 - 10^2} = 13$ μm.

The stored laser power in the cavity during the experiment is shown in Fig. 23. It was 2.6 kW in average with the fluctuation of 37 W. From the width (FWHM) of the resonance of the cavity, it means that the optical path was controlled with the precision of about 4 pm while its total length is 1.68 m.

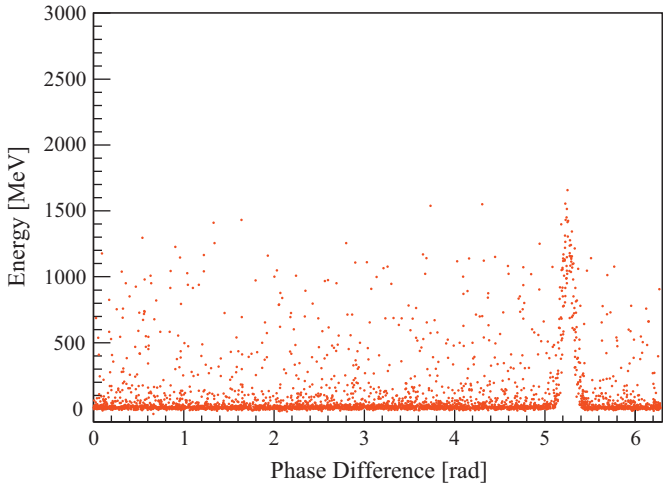

Fig. 21. Compton signal versus phase difference between the ATF master clock and the laser oscillator.

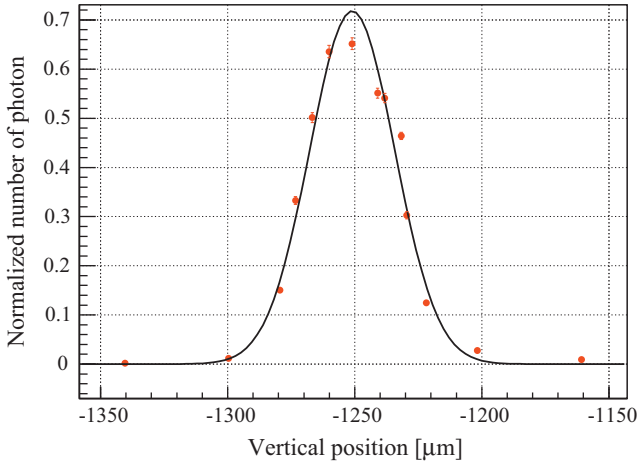

Fig. 22. Observed photon intensity as a function of relative position between the laser beam and the electron beam. Number of photons is normalized by the stored laser power and the electron beam current.

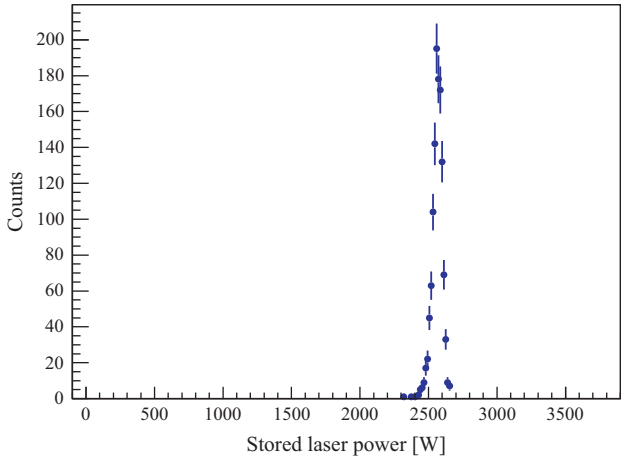

Fig. 23. Stored laser power in the 3D 4-mirror cavity during laser-Compton scattering.

The energy distribution observed by the photon detector is shown in Fig. 24. The average energy was 2970 ± 20 MeV per collision of laser pulses and a train of 5 bunches. Since the average

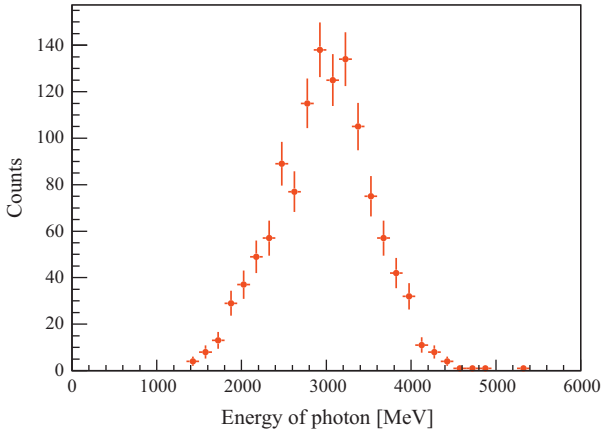

Fig. 24. Energy distribution of observed photon in the detector with 5 electron bunches/train operation.

Table 5
Summary of experimental results and conditions.

Number of bunches	e^- current (mA)	Laser power (kW)	Number of photons (1/train)	Simulation (1/train)
1	2.3	2.5	33.3 ± 0.3	33
5	8.1	2.6	123.8 ± 0.8	123

energy of single photon in the detector is 24 MeV, the total energy corresponds to observation of 124 ± 1 photons per train in the detector. Taking the revolution of the electron beam in the ATF ring into account, it corresponds to the generation of 2.7×10^8 photons per second. The results of the experiment are summarized in Table 5. The expected yield of photons, shown as "simulation" in the table, was calculated by the simulation code CAIN [13]. Parameter for the numerical simulation is summarized in Table 6. The waist sizes of the laser beam were estimated from measured profile of transmitted light from M_2 (Fig. 19(b)), and calculation by using the transfer matrix described in Section 3.2. The estimated laser profile at the laser–electron interaction point is shown in Fig. 25. We used the profile of laser beam in the CAIN simulations. The laser beam spot size of the projection onto the vertical axis is calculated to be 16 μm, which is consistent with the measurement of vertical position scan (see Fig. 22). The expected yield of photons has a systematic error of 5% from the ambiguity of the estimate of laser waist sizes. The photon yield was consistent with the CAIN simulation for 1 and 5 bunches operation.

6. Conclusion

We developed the 3D 4-mirror cavity for the development of the intense photon source by laser-Compton scattering. The average of 2.6 kW of laser light was successfully accumulated in the optical cavity which corresponded to the power enhance factor of 1200. The laser beam spot sizes in its major and minor axis are estimated to be 27 μm and 10 μm, respectively. The average of 124 ± 1 photons per collision was generated in the detector acceptance by laser-Compton scattering in 5 bunches operation of the ATF. It corresponded to the photon intensity of 2.7×10^8 photons per second. The 3D 4-mirror cavity was developed for smaller laser waist and higher finesse than 2-mirror cavity. The high laser power was stored in the cavity as a result of high precision control of the length for the high finesse cavity. This experiment demonstrated the improvement of intense photon

Table 6
Parameters of electron and laser beams.

Description	Value
Electron	
Beam intensity (1 bunch)	0.7×10^{10}
Beam intensity (5 bunches)	2.3×10^{10}
Beam size at IP (σ_x/σ_y)	110/9 μm
Bunch length (σ_z)	20 ps
Laser	
Spot size at IP ($\sigma_{major}/\sigma_{minor}$)	27/10 μm
Pulse width (σ_z)	5 ps
Timing jitter of laser pulse	9–10 ps

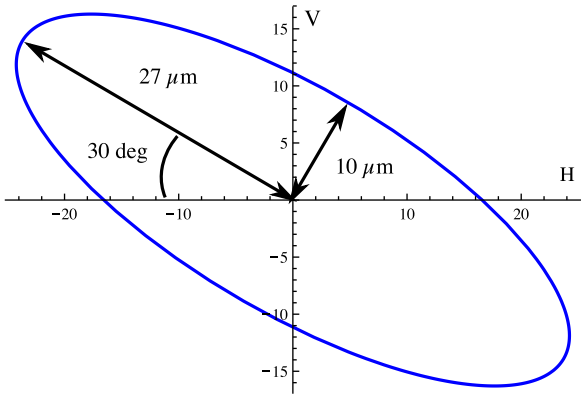

Fig. 25. The estimated laser profile at the laser–electron interaction point.

generation using the 3D 4-mirror cavity and highlighted problems faced by high power stacking such as loss on the mirrors. We observed effect of the thermal load on mirror when high power laser was accumulated in the cavity. For the next step of high power stacking, low-loss mirror is essential.

For further development, we plan to replace mirrors of the cavity with higher reflectivity ones aiming at power enhancement more than 10^4.

Acknowledgments

We express our thanks to all members of ATF-KEK group and LAL collaborators for their helpful support and discussion. This research has been supported by Quantum Beam Technology Program of Japanese Ministry of Education, Culture, Sports, Science and Technology (MEXT). This work was also supported by JSPS KAKENHI Grant number 21340070, 23226020 and 24654076.

References

[1] M. Fukuda, et al., Physical Review Letters 91 (2003) 164801.
[2] T. Omori, et al., Physical Review Letters 96 (2006) 114801.
[3] S. Miyoshi, et al., Nuclear Instruments and Methods in Physics Research Section A 623 (1) (2010) 576.
[4] S. Miyoshi, Ph.D. Thesis, Hiroshima University, 2011.
[5] F. Zomer, et al., Applied Optics 48 (2009) 6651.
[6] F.A. Jenkins, H.E. White, Fundamentals of Optics, McGraw-Hill, 1976.
[7] W.W. Chow, et al., Reviews of Modern Physics 57 (1985) 61.
[8] A.E. Siegman, Lasers, University Science Books, 1986.
[9] S.J.M. Habraken, G. Nienhuis, Physical Review A 75 (2007) 033819.
[10] A. Variola, et al., Physical Review Special Topics—Accelerators and Beams 14 (2011) 031001.
[11] Y. Honda, et al., Optics Communications 282 (15) (2009) 3108–3112.
[12] ATF Collaboration. ⟨http://atf.kek.jp/collab/ap/⟩.
[13] K. Yokoya. ⟨http://lcdev.kek.jp/~yokoya/CAIN/Cain242/⟩.

参考論文

(1) Photon generation by laser-Compton scattering at the KEK-ATF
S. Miyoshi, T. Akagi, S. Araki, Y. Funahashi, T. Hirose, Y. Honda, M. Kuriki, X. Li, T. Okugi, T. Omori, G. Pei, K. Sakaue, H. Shimizu, T. Takahashi, N. Terunuma, J. Urakawa, Y. Ushio and M. Washio
Nuclear Instruments and Methods in Physics Research Section A **623,** 576－578 (2010).

(2) Production of gamma rays by pulsed laser beam Compton scattering off GeV-electrons using a non-planar four-mirror optical cavity
T. Akagi, S. Araki, J. Bonis, I. Chaikovska, R. Chiche, R. Cizeron, M. Cohen, E. Cormier, P. Cornebise, N. Delerue, R. Flaminio, S. Funahashi, D. Jehanno, Y. Honda, F. Labaye, M. Lacroix, R. Marie, C. Michel, S. Miyoshi, S. Nagata, T. Omori, Y. Peinaud, L. Pinard, H. Shimizu, V. Soskov, T. Takahashi, R. Tanaka, T. Terunuma, J. Urakawa, A. Variola and F. Zomer
Journal of Instrumentation **7**, P01021 (2012).

(3) Gamma-rays Generation with 3D 4-mirror Cavity for ILC Polarized Positron Source
T. Akagi, M. Kuriki, S. Miyoshi, T. Takahashi, R. Tanaka, H. Yoshitama, S. Araki, Y. Funahashi, Y. Honda, T. Okugi, T. Omori, H. Shimizu, N. Terunuma, J. Urakawa, K. Sakaue, M. Washio, H. Kataoka and T. Kon
Proceedings of IPAC2012, New Orleans, Louisiana, USA (2012).

Nuclear Instruments and Methods in Physics Research A 623 (2010) 576–578

Contents lists available at ScienceDirect

Nuclear Instruments and Methods in Physics Research A

journal homepage: www.elsevier.com/locate/nima

Photon generation by laser-Compton scattering at the KEK-ATF

S. Miyoshi [a,*], T Akagi [a], S. Araki [b], Y. Funahashi [b], T. Hirose [c], Y. Honda [b], M. Kuriki [a], X. Li [d], T. Okugi [b], T. Omori [b], G. Pei [d], K. Sakaue [c], H. Shimizu [b], T. Takahashi [a], N. Terunuma [b], J. Urakawa [b], Y. Ushio [a], M. Washio [c]

[a] Graduate School of Advanced Sciences of Matter, Hiroshima University, Higashi-Hiroshima, Hiroshima 739-8530, Japan
[b] High Energy Accelerator Research Organization, Tsukuba, Ibaraki 305-0801, Japan
[c] Research Institute for Science and Engineering, Waseda University, Tokyo 162-0044, Japan
[d] Institute of High Energy Physics, Chinese Academy of Sciences, Beijing 100049, China

ARTICLE INFO

Available online 25 March 2010

Keywords:
Compton
ILC
Mode locked laser
Optical resonant
Cavity
Polarized positron source
Pulse laser stacking

ABSTRACT

We performed a photon generation experiment by laser-Compton scattering at the KEK-ATF, aiming to develop a Compton based polarized positron source for linear colliders. In the experiment, laser pulses with a 357 MHz repetition rate were accumulated and their power was enhanced by up to 250 times in the Fabry–Perot optical resonant cavity. We succeeded in synchronizing the laser pulses and colliding them with the 1.3 GeV electron beam in the ATF ring while maintaining the laser pulse accumulation in the cavity. As a result, we observed 26.0 ± 0.1 photons per electron-laser pulse crossing, which corresponds to a yield of 10^8 photons in a second.

1. Introduction

The International Linear Collider (ILC) seeks to provide polarized electron beams for precise measurements of physics phenomena. In addition to the electron beam, there are hopes that polarizing positron beams as well will further improve the performance of the ILC as a machine for making precise measurements [1]. The polarized positrons are generated via pair creation by impinging polarized photons of about 10 MeV into target materials. Therefore, the generation of polarized intense photons of the 10 MeV energy regions would be a key technology for the polarized positron source. The ILC baseline design adopts the helical undulator scheme in which 150 GeV electrons are fed into the helical undulator with a length of more than 150 m to create photons [2]. Though the undulator scheme is the baseline design, a 150 m-long undulator has yet to be developed and we will have to wait until the construction of the main LINAC of the ILC before an electron beam of 150 GeV can be provided.

One option for polarized positron generation is to use laser-Compton scattering for photon generation (the Compton scheme). The advantage of the Compton scheme is that the required energy of the electron beam to generate 10 MeV photons is about 1 GeV, which is low enough to develop positron sources using the existing small electron beam facilities. In addition to the energy of the electron beam, the polarization of the generated positrons can be easily controlled in the Compton scheme by changing the polarization of the laser, though accomplishing this with the undulator scheme is neither a self-evident nor easy task. Thus the Compton scheme is being developed in parallel with the undulator scheme. We report in this paper on the status of the R&D efforts for the Compton scheme in the KEK-ATF.

The proof of the principle of generating polarized positrons with the Compton scheme has been demonstrated by a series of experiments performed at the ATF [3]. The next step toward the positron source will be to increase the intensity of photons required by the ILC. For this purpose, we adopt a scheme to increase the intensity of the laser pulses by accumulating them in an optical resonant cavity. Since accumulation of laser pulses in the cavity requires precise control of the optical system, and the ATF requires sophisticated machine operation to maintain the ultra-low emittance of its beam, it is no easy task to accommodate an optical system in the accelerator environment and to make laser pulses collide with the electron beam. Therefore we installed a Fabry–Perot type optical resonant cavity in the ATF damping ring, as shown in Fig. 1, and performed an experiment to generate photons by laser-Compton scattering.

2. Experimental setup

The beam energy and typical beam size of the ATF are 1.3 GeV and 100 μm (horizontal) ×10 μm (vertical) in the root mean square, respectively. The repetition rate of laser pulses is

* Corresponding author.
E-mail address: miyoshi@hep.adsm.hiroshima-u.ac.jp (S. Miyoshi).

0168-9002/$ - see front matter © 2010 Elsevier B.V. All rights reserved.
doi:10.1016/j.nima.2010.03.075

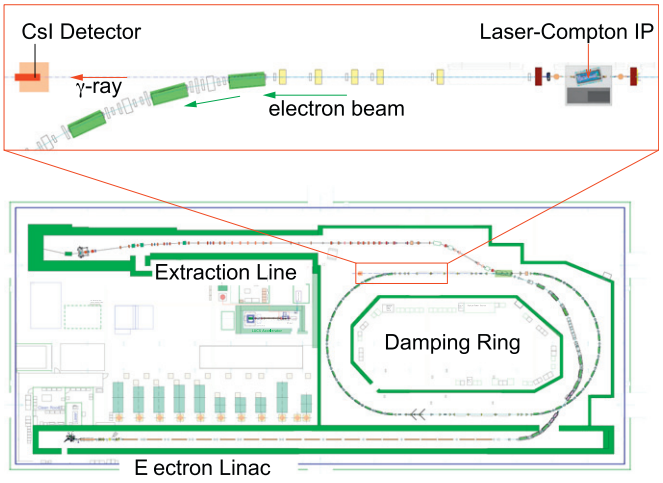

Fig. 1. (color) The optical resonant cavity is installed in the straight section of the KEK-ATF damping ring [4]. A CsI detector for photon detection is placed the 18 m downstream of the laser electron interaction point in the optical resonant cavity.

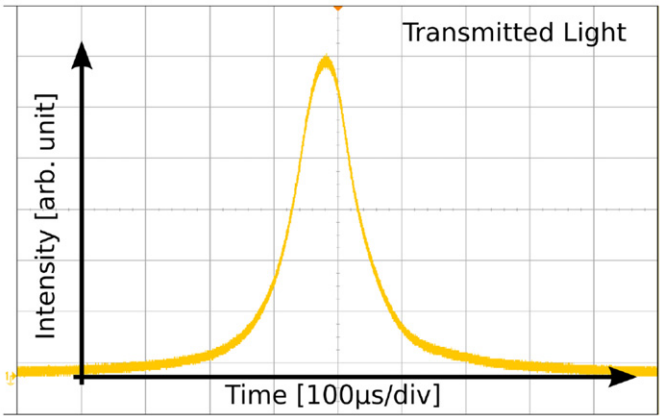

Fig. 2. The intensity of the transmitted light from the optical resonant cavity. The yellow line is the transmitted laser power. The peak for intensity shows the cavity is on-resonance. (For interpretation of the references to color in this figure legend, the reader is referred to the web version of this article.)

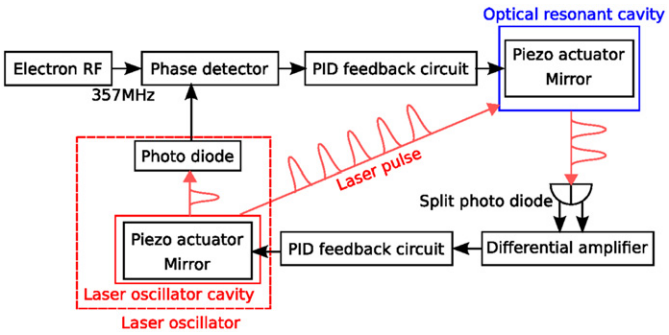

Fig. 3. Schematic of the feedback system for the laser pulse accumulation and timing synchronization. See text and Ref. [6] for detail.

357 MHz, which is the same as the electron bunch spacing in the ATF. The wavelength and pulse width of the laser are 1064 nm and 5 ps in the root mean square. The crossing angle of the laser pulse and the electron beam is 12°, which determined the maximum energy of the Compton gamma at 28 MeV. The energy of the photon was discriminated by the slit placed between the laser–electron interaction point and the CsI photon detector. As a result, the energy of photons detected in the detector is 19–28 MeV with the average of 24 MeV.

In order to accumulate laser pulses in the optical resonant cavity, the cavity has to be on-resonance with the injected laser pulses. It requires the length of the optical resonant cavity to be integer times the half wave length of the laser wave precisely. In addition, accumulation of mode locked pulsed lasers requires that the length of the optical resonant cavity is integer times those of the cavity inside the laser oscillator. Therefore the length of the optical resonant cavity is 420 mm. The waist size of laser pulses is 30 μm (1σ) in the optical resonant cavity, because the curvature radius of mirrors is 210.5 mm. The resonant condition of the optical resonant cavity is monitored by the intensity of the transmitted light from the cavity, which is at the maximum when the cavity is on-resonance. The intensity of the transmitted light obtained by changing the length of the cavity is shown in Fig. 2. We observed a resonant peak with a width of 0.7 nm which indicated that the length of the optical resonant cavity has to be controlled within this precision. The resonant condition in terms of the finesse was estimated from the width and was about 1000, which is consistent with expectations from the mirror reflectivity of 99.6%, within the error.

To accumulate laser pulses in the optical resonant cavity and continuously make collisions of laser pulses and electron bunches, the length of the optical cavity has to be kept within the nm range and the timing between laser pulses and electron bunches has to be synchronized within ps precision. For this purpose we developed the feedback system as schematically shown in Fig. 3, in which special care was taken to achieve stable resonant and timing synchronization [5]. Firstly, the feedback system, consisting of a mode locked laser and the resonant cavity, forms a single closed loop for stable feedback operation. Secondly, the system was constructed taking the required speed for the feedback operation into account. Keeping the resonance of the resonant cavity needs relatively faster feedback while the timing synchronization can be relatively slow. On the other hand, the length of the optical cavity cannot be changed rapidly as it uses relatively large mirrors while laser wave length can change faster as it uses smaller size mirrors. Therefore, the resonant signal from the optical cavity is fed back to the mode locked laser while the timing synchronization is achieved by adjusting the length of the optical cavity. The performance of the feedback system is shown in Fig. 4. The left hand of Fig. 4 shows the transmitted laser power while sweeping the length of the optical resonant cavity. The right hand of Fig. 4 shows the resonance and synchronization signal with the feedback loop system turned on. It shows that we successfully achieved stable resonance of the cavity with the laser wave as well as timing synchronization of the laser pulses and the electron bunches.

3. Experiment

We performed detection of Compton photons with 1, 5, 10 and 15 electron bunches/train in the ATF. First, we scanned the position of the optical resonant cavity relative to the electron beam to find the optimum position. Then, the timing of the laser pulses relative to the electron bunches was adjusted by changing relative phase between the ATF master oscillator and laser pulses. Fig. 5 shows the energy deposit of Compton photons in the CsI detector which was placed 18 m downstream of the laser–electron interaction point. At 15-bunch operation, we observed 26.0 ± 0.1 photons/train. Since the revolution rate of the electron bunches in the ATF is 2.16 MHz, it can be estimated that 10^8 photons are generated per second in all solid angles.

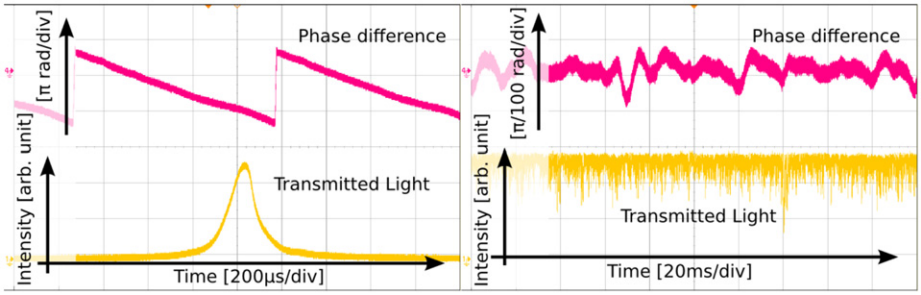

Fig. 4. The intensity of the transmitted light (yellow), and the relative phase between ATF master signal and laser pulse (red) when the feedback is turned off (left) and on (right). The intensity of the transmitted light in the right figure is constant and its value corresponds to the peak in the left figure. The phase signal in the right hand figure is also constant with some fluctuation of about 5 ps. (For interpretation of the references to color in this figure legend, the reader is referred to the web version of this article.)

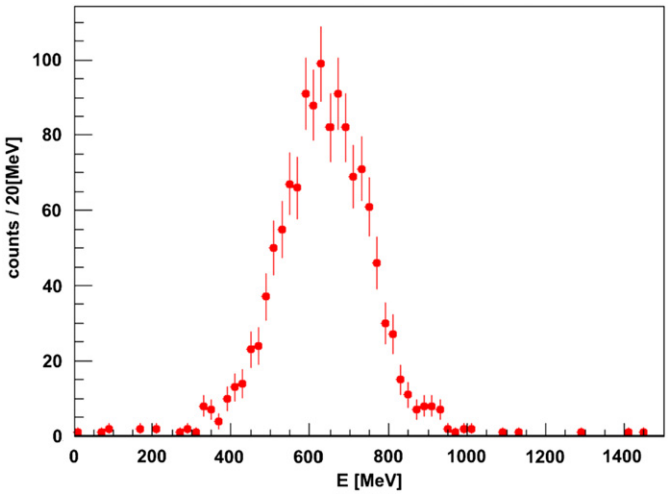

Fig. 5. Energy deposit in the CsI detector observed from laser–electron interaction with 15 electron bunches/train.

Table 1
Summary of experimental results and conditions.

# of bunches	e^- current (mA)	Laser power (W)	Gamma (1/train)	Simulation	Normalize (gamma/AW)
1	2.2	437 ± 2	5.4 ± 0.3	4.9 ± 0.3	5.6 ± 0.3
5	4.7	423 ± 2	10.6 ± 0.1	10.5 ± 0.5	5.3 ± 0.1
10	8.5	470 ± 2	19.0 ± 0.1	21 ± 1	4.8 ± 0.1
15	11	498 ± 2	26.0 ± 0.1	29 ± 1	4.8 ± 0.1

There are additional 3% systematic errors common for all "Gamma" measurements. There are additional 14% systematic errors common for all "Laser power" measurements.

The results of the experiment under each condition, i.e. the number of bunches per train and the laser power, are summarized in Table 1. The expected yields, shown as "Simulation" in the table, were calculated by the simulation code CAIN [7]. The ambiguity of the simulation arose mainly from the uncertainty of the electron bunch length during the experiment, which varied from 6.0 to 9.0 mm depending on accelerator conditions. The photon yields were consistent with the simulation with a smaller number of bunches per train, while they deviated from the simulation with a larger number of bunches per train. The reason for these deviations is under investigation. We suspect that it may be due to synchrotron oscillation of electron bunches, as this effectively enlarges the average bunch length in a train. The bunch oscillation was investigated using a streak camera and larger oscillation for larger number of bunches was observed. However, a detailed comparison with the photon yield taken under accelerator conditions is still in progress.

4. Conclusions

The optical resonant cavity was constructed and installed in the KEK-ATF electron ring for the purpose of the photon generation by laser-Compton scattering, aimed at the development of a polarized positron source. We succeeded in accumulating laser pulses in the optical resonant cavity and synchronizing them with the electron bunches simultaneously under the operation of the ATF. The laser power was enhanced up to 250 times that of injection power by the accumulation. The generated photons were 26.0 ± 0.1 photons/train, which corresponds to 10^8/second. The results demonstrated the feasibility of using the optical resonant cavity for effective photon generation by laser-Compton scattering. The photon yields were almost consistent with expectations but appreciable deviation was observed for larger number of bunches per train. The effect of synchrotron oscillation on the bunch in the ATF may be a cause but further investigation is necessary.

Acknowledgements

The authors would like to thank ATF collaborators for discussing and helping. This work was supported in part by KAKENHI [(B)18340076, 17GS0210], Quantum Beam Technology Program by JST, the KEK Promotion of collaborative research programs in universities and the Hiruma research funds at Hiroshima University.

References

[1] G. Moortgat-Pick, et al., Phys. Rep. 460 (2008) 131.
[2] ILC-REPORT-2007-001, 2007.
[3] T. Omori, et al., Phys. Rev. Lett. 96 (2006) 114801.
[4] H. Shimizu, et al., J. Phys. Soc. Jpn. 78 (2009) 074501.
[5] K. Sakaue, Doctoral Thesis, Waseda University, 2009.
[6] D.A. Shaddock, et al., Opt. Lett. 24 (1999) 1499.
[7] K. Yokoya 〈http://lcdev.kek.jp/yokoya/CAIN/cain235/〉.

JINST

PUBLISHED BY IOP PUBLISHING FOR SISSA

RECEIVED: *November 24, 2011*
ACCEPTED: *January 5, 2012*
PUBLISHED: *January 31, 2012*

Production of gamma rays by pulsed laser beam Compton scattering off GeV-electrons using a non-planar four-mirror optical cavity

T. Akagi,[e] S. Araki,[d] J. Bonis,[a] I. Chaikovska,[a,1] R. Chiche,[a] R. Cizeron,[a] M. Cohen,[a] E. Cormier,[b] P. Cornebise,[a] N. Delerue,[a] R. Flaminio,[c] S. Funahashi,[d] D. Jehanno,[a] Y. Honda,[d] F. Labaye,[a] M. Lacroix,[a] R. Marie,[a] C. Michel,[c] S. Miyoshi,[e] S. Nagata,[e] T. Omori,[d] Y. Peinaud,[a] L. Pinard,[c] H. Shimizu,[d] V. Soskov,[a] T. Takahashi,[e] R. Tanaka,[e] T. Terunuma,[d] J. Urakawa,[d] A. Variola[a] and F. Zomer[a]

[a] *LAL, CNRS-IN2P3, Université Paris-Sud XI, Centre Scientifique d'Orsay, Bâtiment 200, BP 34, 91898 Orsay cedex , France*

[b] *CELIA, CNRS, Université de Bordeaux, Domaine du Haut Carré, 43, Rue Pierre Noailles, 33405 Talence, France*

[c] *LMA, CNRS-IN2P3, Université Claude Bernard Lyon I, Bâtiment Virgo 7, Avenue Pierre de Coubertin, 69622 Villeurbanne cedex, France*

[d] *ATF, High Energy Accelerator Research Organization (KEK), 1-1 Oho, Tsukuba, 305-0801 Ibaraki, Japan*

[e] *Hiroshima University, 1-3-2 Kagamiyama, Higashi-Hiroshima 739-8511, Japan*

E-mail: chaikovs@lal.in2p3.fr

ABSTRACT: As part of the positron source R&D for future $e^+ - e^-$ colliders and Compton based compact light sources, a high finesse non-planar four-mirror Fabry-Perot cavity has recently been installed at the ATF (KEK, Tsukuba, Japan) [1]. The first measurements of the gamma ray flux produced with a such cavity using a pulsed laser is presented here. We demonstrate the production of a flux of 2.7 ± 0.2 gamma rays per bunch crossing ($\sim 3 \times 10^6$ gammas per second) during the commissioning.

KEYWORDS: Instrumentation for particle accelerators and storage rings - high energy (linear accelerators, synchrotrons); Accelerator Applications

ARXIV EPRINT: 1111.5834

[1] Corresponding author.

doi:10.1088/1748-0221/7/01/P01021

2012 JINST 7 P01021

Contents

2012 JINST 7 P01021

1 Introduction

High Energy physics [2–4] as well as applied physics [5–8] are showing a great interest for intense flux of high energy X-rays and gamma rays.

These gamma or alternatively X-rays can be generated by Compton scattering [9]. To achieve a high flux of high energy photons despite the low cross section of Compton scattering one requires a high average power laser system based on a Fabry-Perot cavity [10] together with a high current electron beam [11]. In this context, a two-mirror Fabry-Perot cavity has already been successfully operated at the Accelerator Test Facility [12] (ATF) of KEK [13, 14].

A solution to produce a high flux of circularly polarized gamma rays is to use a four-mirror Fabry-Perot cavity (FPC) where laser pulses can be stacked to reach a high average power at the interaction point (IP). A prototype of non-planar high finesse four-mirror Fabry-Perot cavity has been installed at the KEK ATF and is described in details in [1]. The optical system has been commissioned during summer 2010 and electron-photon Compton collisions were observed on the first attempt in October 2010. In this paper we present measurements of the gamma ray flux recorded during our commissioning. The data analyzed here were taken before the tragic earthquake which struck Japan in March 2011. Recovery and improvement work is being carried out since but is not covered by this paper.

This paper is organised as follows. Section 2 describes the experimental setup used to produce and measure the gamma rays. Section 3 discusses the gamma ray flux expected with our current

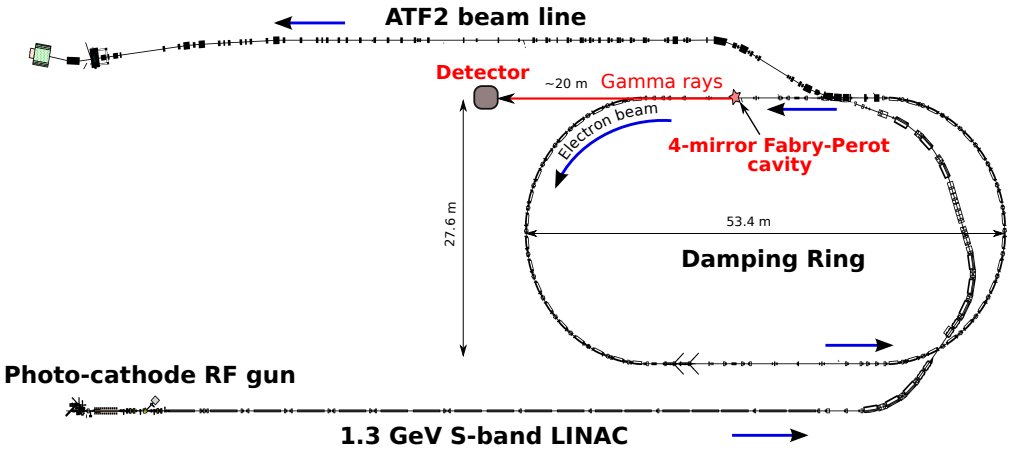

Figure 1. Layout of the Accelerator Test Facility at KEK. The red star indicates the approximate location of the 4-mirror Fabry-Perot cavity described in [1] and used for the measurements presented in this paper. The red arrow indicates the direction of propagation of the gamma rays produced. The grey box indicates the gamma ray detector (adapted from [14]).

setup. Section 4 explains how the data were analyzed. Section 5 presents the gamma ray spectra measured. Finally, the main results and further steps are discussed in section 6.

2 Experimental setup

2.1 Accelerator Test Facility

A detailed description of the ATF at KEK can be found in [12, 15, 16]. The 1.28 GeV damping ring (DR) has a revolution period of 462 ns and operates at the radio frequency (RF) of 357 MHz (165 RF buckets spaced by 2.8ns). Although a total of up to 3 trains of 10 bunches separated by 5.6 ns can be injected in the ring, most operations run with a single bunch in the train or with a train of up to 10 bunches [17]. Our FPC is installed in one of the straight sections of the damping ring as shown on figure 1. After the collisions the gamma rays, propagating along the electron beam, are extracted through a window before passing through several collimators. They are measured by a gamma detector about 20 m downstream the IP.

The main parameters of the electron beam at the ATF DR are given in the table 1.

2.2 Fabry-Perot cavity

The FPC is composed of 2 concave mirrors with a radius of curvature of 0.5 m and two flat mirrors with a non-planar tetrahedron geometry. The mirrors have a very high reflectivity (1 - 1060 ppm for one of them and 1 - 330 ppm for the others) leading to a cavity finesse of the order of 3000 (corresponding to a passive power enhancement of about 1000). A round trip time of 5.6 ns in the FPC is set to match half the RF frequency of the ATF DR at 178.5 MHz.

2012 JINST 7 P01021

Table 1. ATF DR parameters.

Description	Value
Electron energy, E_e	1.28 GeV
Electron bunch population, N_e	$\sim 0.5 \times 10^{10}$
Electron bunch length, $\sigma_z/c = \tau_e$	~ 20 ps
Electron beam size, σ_x/σ_y	~ 110 / 10 μm
Revolution period, T_0	462 ns
Emittance, $\gamma\varepsilon_{x/y}$	5×10^{-6} / 3×10^{-8} m·rad

Table 2. Parameters of the laser system used during the data taking presented here.

Description	Value
Laser photon energy, E_{ph}	1.2 eV (λ_{ph} =1032 nm)
Laser spot size, σ_x/σ_y	26 / 38 μm
Laser repetition rate, f_L	178.5 MHz $\pm$ 4 KHz
Finesse, F	~ 3000
Laser pulse length, τ_L	68 ps
Average power stored in FPC, P_L	~ 160 W
Crossing angle, ϕ	8 deg.

A passively mode-locked oscillator is amplified in a microstructured active fiber and further injected in the FPC. An all-digital double feedback system is used to lock the cavity on the ATF clock and to ensure that the laser pulses are properly stacked with interferometric accuracy.

The FPC is mounted on an optical table which is itself mounted on movers that allow to control precisely the vertical position of the FPC with respect to that of the laser beam.

Table 2 summarises the main parameters of the system and more details on the experimental apparatus can be found in [1].

As there is an odd number of RF buckets in the DR collisions on a given electron bunch occur only every other turn, at a frequency of 1.08 MHz.

Data acquisition. The data acquisition relies on several oscilloscopes to acquire information from the FPC and from the calorimeter. The waveforms acquired are timestamped in a database and saved on disk for later analysis. Data from the accelerator such as beam position and charge are also acquired and saved in the database.

2.3 Calorimeter

To detect the gamma rays produced by the collisions between the laser photons and the electrons, we use a fast scintillation detector made of barium fluoride (BaF_2) coupled with a Photomultiplier Tube (PMT). Two polished rectangular crystals of BaF_2 with dimensions

2012 JINST 7 P01021

100 mm × 70 mm × 70 mm are glued to each other and wrapped into an absorbing tape. The 200 mm depth of the BaF_2 calorimeter is nearly 10 radiation lengths, ensuring high detection efficiency [18].

Barium fluoride is commonly used as it has two emission spectra peaks at 220 nm and 310 nm with decay time constants of about 0.8 ns and 630 ns respectively. The decay time of the fast component of BaF_2 allows to resolve two successive pulses of gamma rays generated from the electron bunches spaced by 5.6 ns. To eliminate the slow component of the scintillation an optical filter has been installed in front of the PMT. A fast PMT (Hamamatsu Photonics R3377) with a rise time of 0.7 ns is used. Data acquisition is performed using a LeCroy WS454 oscilloscope (1GS/s, 500 MHz bandwidth).

GEANT4 simulations. Using Geant4 [19] we simulated the detector to study the development of electromagnetic showers inside the BaF_2 calorimeter.

This allows to perform realistic simulations of high energy gammas passing through the calorimeter. The initial distribution of the gamma rays is obtained by using the beam-beam interaction code CAIN2.40 [20]. Once a gamma ray hits the calorimeter, scintillation light is uniformly emitted along the path of the charged particles produced by the electromagnetic shower. The number of optical photons generated is proportional to the energy loss of the initial gamma rays. The scintillation light then propagates and finally reaches the PMT located at the end of the scintillator.

3 Expected gamma ray flux

Using the Compton scattering physical properties it is possible to estimate the expected number of scattered gamma rays in the experiment. Neglecting the divergence of the electron and laser beam at the IP, the luminosity for the Compton collisions is given by equation 3.1 in [21]:

$$\mathscr{L} = N_e N_{ph} f \frac{\cos(\phi/2)}{2\pi} \frac{1}{\sqrt{\sigma_{ye}^2 + \sigma_{yph}^2}\sqrt{(\sigma_{xph}^2 + \sigma_{xe}^2)\cos^2(\phi/2) + (\sigma_{ze}^2 + \sigma_{zph}^2)\sin^2(\phi/2)}}, \quad (3.1)$$

$$\mathscr{F} = \frac{dN_\gamma}{dt} = \sigma_{Compton} \cdot \mathscr{L}, \quad (3.2)$$

where N_e, N_{ph} are the number of the electrons in the bunch and number of the photons in the laser pulse respectively, f is the repetition frequency, ϕ is the angle of the collisions, $\sigma_{\vec{r}e}$ and $\sigma_{\vec{r}ph}$ indicate respectively the RMS sizes of the electron bunch and the laser pulse. Once, the luminosity of the process is defined, the flux of gamma rays is given by formula 3.2, where $\sigma_{Compton}$ is the total Compton scattering cross section which is determined by the momenta of the incident electron and laser photon [22].

Formulas 3.1 and 3.2 show that the emitted rate is inversely proportional to the transverse electron and laser beam sizes. These formulas shows also that a collision angle reduces the gamma ray flux especially in the case of long electron bunches and laser pulses.

The simulation code CAIN has been used to simulate the Compton scattering process. This code simulates the interaction between one electron bunch and one laser pulse where the Compton cross section is calculated for all the possible polarization states [22] and takes into account the

2012 JINST 7 P01021

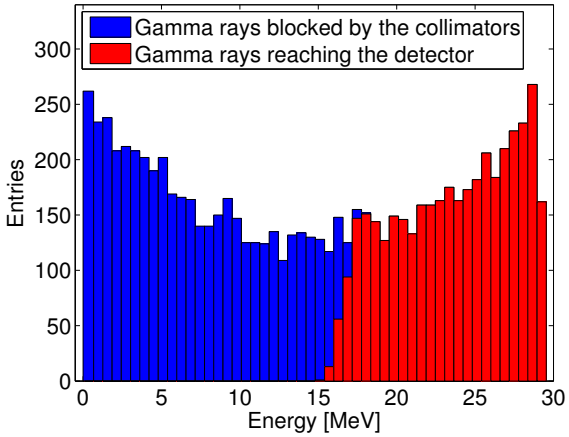

Figure 2. Energy spectrum of the gamma rays. The energies of the gamma rays blocked by the collimators are shown as well as the energies of the gamma rays entering the detector. Only the gamma rays with energies above 15 MeV are accepted by the collimators.

beam geometry. Using the parameters listed in table 1 and 2 the energy spectrum and expected number of the scattered gamma rays per bunch crossing have been obtained.

As it was mentioned before, in the experiment the scattered gamma rays pass through several collimators before entering the detector. This carries out a gamma energy spectrum selection owing to the energy-angle correlation in Compton scattering. Figure 2 shows the simulated energy spectrum of the gamma rays where the red color refers to the gamma rays transmitted by the collimators and blue color refers to the gamma rays filtered out due to their energy/angle.

The average energy of the gamma rays produced is $\sim$15 MeV. However, due to the limited geometrical aperture, the gamma rays below 15 MeV do not reach the detector. The average energy of the gamma rays reaching the detector is therefore 24 MeV. Later, these results are used for the Geant4 simulation and calibration of the calorimeter.

4 Measurements

4.1 Scanning procedure and first data

The FPC was commissioned in October 2010 and Compton collisions were recorded on the first attempt (26 October). Before data taking we investigated how the intensity of the signal is affected by the position of the laser beam waist with respect to the electron beam position and synchronization between the laser and electron beam by doing the position and the phase scans.

The search for the collisions area between the electrons and the laser photons has several degrees of freedom and is not straightforward. The two most sensitive degrees of freedom are the vertical position of the FPC (dimension orthogonal to the plane of the beams) and the relative phase between the laser and the electrons (time dimension). The search for collisions is performed in several steps:

2012 JINST 7 P01021

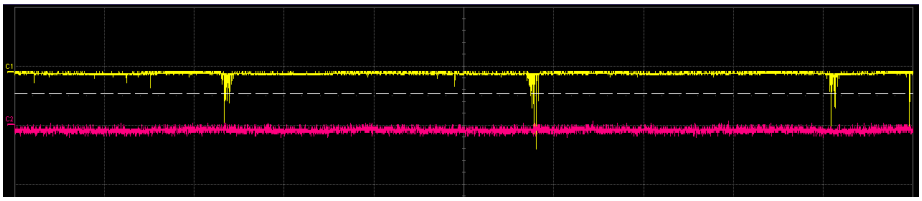

Figure 3. Example of signal observed on our oscilloscope while scanning the parameters space to find the collision area. The yellow line is the signal from the PMT. The duration of the waveform is 10 ms and the vertical scale is 200 mV (on this day the signal was amplified).

- The FPC frequency is offset by at least 100 Hz with respect to the ATF frequency. By doing this the relative phase between the electrons and the laser is automatically scanned at a rate of at least 100 Hz.
- The vertical position of the FPC is swept slowly.
- While performing this vertical scan we look on the data acquisition oscilloscope for the apparition of short bursts in the output of the PMT (see figure 3). The length and the frequency of these bursts are related to the difference between the frequency of the cavity and the frequency of the ATF clock.
- Once these bursts have been found the vertical position of the laser is adjusted to maximize their intensity.
- At this stage the laser frequency can be locked on the ATF frequency.
- The phase of the laser with respect to the electron beam must be adjusted to optimize the intensity of the signal observed on the PMT output.[1]

The bursts correspond to the time at which the phase of the laser matches that of the electrons. The distances between the bursts corresponds to the difference between the ATF frequency and the laser frequency. Each burst contains several peaks spaced by the duration of two DR revolution. The red line records the injection trigger (the trigger itself is off the screen). It was checked that the bursts on the yellow lines disappear when the cavity is moved vertically by a distance greater than the beam size.

4.2 Example of data

During data taking we record the signal from the PMT as well as the 357 MHz ATF clock and the laser power transmitted by the FPC measured by a photodiode. To avoid the mistaking noise from the injection or extraction kickers a typical data acquisition starts at least 200 ms after the injection trigger is received. At this time we expect the beam to be almost fully damped. A typical signal waveform from the calorimeter can be observed on figure 4. A full waveform contains approximately 200 000 samples spaced by 1 ns.

[1] Our experience shows that the variation of this phase from day to day is small however we do observe small drifts which require a new phase scan on each run.

2012 JINST 7 P01021

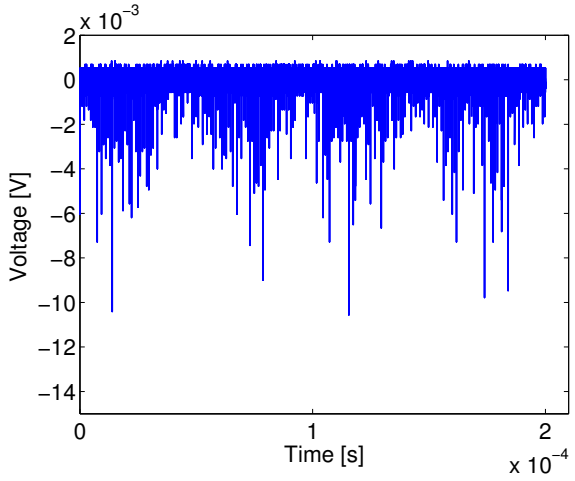

Figure 4. The typical signal shape for the high energy gamma rays produced by Compton scattering observed at the anode output of the PMT. Each spike on the picture corresponds to the gamma production after successive bunch crossings over 0.2 ms. Data shown correspond to a single bunch stored in the ATF DR.

4.3 Data analysis

The raw data recorded contain the intensity of the PMT output as a function of time (see figure 4). Data analysis was carried out to extract the intensity of the Compton signal and remove unwanted backgrounds.

As the data were acquired during the different ATF runs with different filling mode of the DR (1 train, 2 trains, 3 trains stored in the ATF DR) the correct number of Compton peaks and their timing must be found. The 357 MHz ATF clock is used to define the beginning of a 924 ns periods corresponding to the occurrence of the Compton signal (two ATF DR revolutions). All 924 ns periods belonging to one data file (usually 0.2 ms long) are superimposed on top of each other to find the number of the peaks per revolution and their time of arrival with respect to the beginning of the period. Such technique is used to enhance the signal over the background reducing at the same time the electronic noise. This results in a more precise way for the estimation of the number of the peaks and their timing. An example of stacking can be seen on figure 5a.

Once the number of peaks and their positions within the period is found we define a gate around the position where the Compton signal is expected. We use this gate to calculate the height and integral of the peak. The Compton peak height and its integral are our measure of the energy deposited by the gamma rays in the calorimeter. The length of the gate is set to 12 ns in order to entirely contain the signal thus ensuring a correct evaluation of the energy deposited. The distribution of such gates around the peak is presented on figure 5b.

The background level and its RMS are calculated within each period and are subtracted from the corresponding peak height and peak integral. The background level is defined as the mean over the timebase corresponding to a given period excluding the gate containing the signal. The average background level and its RMS for our data sample is estimated to be around 7 μV and 0.2 mV respectively. Finally, the peak height and peak integral are calculated for every peak within the period (see figure 6a).

The shape of the detector's response creates a linear relation between the total charge and the

2012 JINST 7 P01021

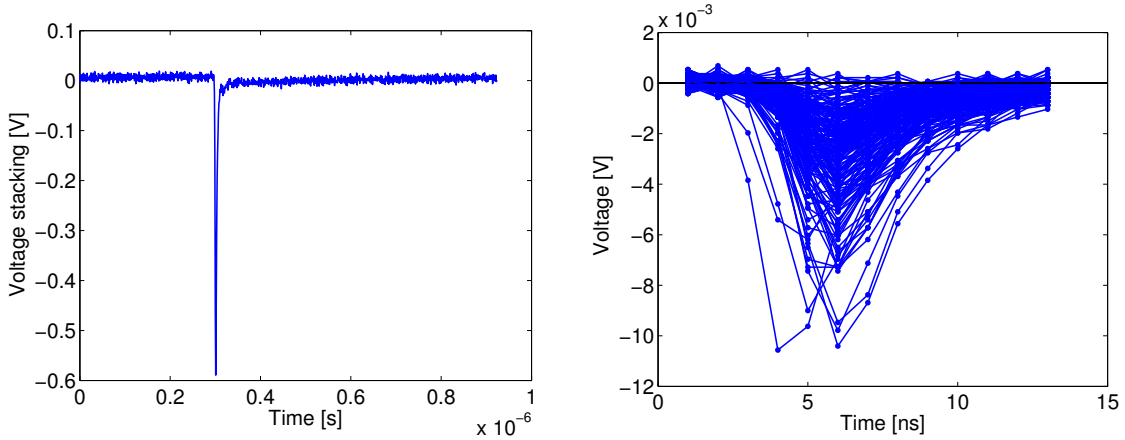

(a) (b)

Figure 5. Stacking of all the 924 ns periods from the data file presented on figure 4 (figure 5a). This stacking is used to find the number of the peaks and their timing. Time profile of the signals for all the periods from the same file is shown on figure 5b.

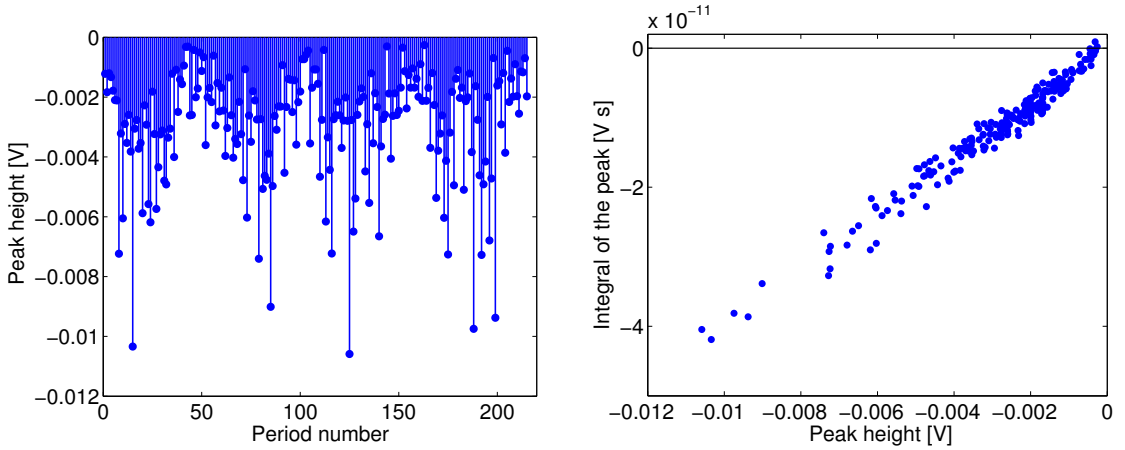

(a) (b)

Figure 6. Figure 6a gives an example of the peak height distribution from the data file presented on figure 4. Peak height vs. peak integral for the same data file is shown on figure 6b.

maximum charge measured. This can be seen as a correlation between the calculated peak height and peak integral as shown on figure 6b

Quality of the data. Different quality cuts are applied to restrict the analysis to a high purity sample. By putting limitations on them we can reject noise and obtain a set of good quality data (see figure 7).

We want all the Compton peaks within one file to have the same phase with respect to the ATF clock. It is achieved, in this case, by requiring the Compton signal to arrive 6 ns after the beginning of the gate (see figure 7a).

2012 JINST 7 P01021

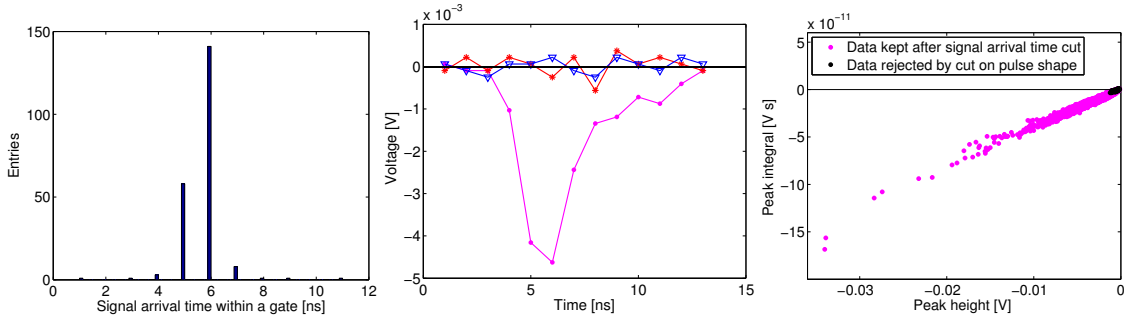

(a) **(b)** **(c)**

Figure 7. Quality cut illustration (figures 7a and 7b) shown together with their effect on all the data sample (figure 7c). Figure 7a: the distribution of the signal arrival time within the gate for all the signals found in the data file presented on figure 4. Figure 7b gives an example of a correct signal (magenta line) as opposed to the noise signal (blue, red line). Figure 7c shows the data sample remaining after the cut on the signal arrival time applied (magenta points) together with the events which are rejected due to the cut on the shape of the pulse (data points tagged in black).

Sometimes, the noise can dominate the signal (see figure 7b). Quite often, these signals can even lead to an integral value with the wrong sign. This is illustrated on figure 6b by the dots with positive values of the integral of the peak. Such events have to be considered as picked up noise and must be rejected. For this, we introduce a variable:

$$V = \frac{2I_{\max}(t_0)}{I(t_0-1)+I(t_0+1)}, \tag{4.1}$$

where $I_{\max}(t_0)$ is the intensity of the signal taken at the time when it reaches maximum, $I(t_0-1)$ and $I(t_0+1)$ are the intensities of the signal in the two nearest data points. By imposing $1 \leq V \leq 10$ the noise is filtered out as V reaches either negative or very high positive values for noise signal. On figure 7b the magenta line corresponds to the real Compton signal for which our estimator variable V is about 1 while the red and blue lines are for the noise events and in this case V equals to -2 and 17 respectively.

The effect of the cuts mentioned above is shown on figure 7c. Cut on the signal arrival time preserve good linear relation between the peak height and peak integral apart from a few high intensity data points for which our data acquisition system saturated. The cut on the shape of the pulse helps to remove noise. However, some low intensity events still remain which correspond to the low energy deposited by the gamma rays in the calorimeter.

Approximately half of the data taken and presented in this study have been rejected after the different quality cuts have been applied. All the results commented below are based on high quality data sample.

Background. While analysing the data we noticed that some data files contain peaks spaced by about 462 ns corresponding to one ATF DR revolution period. With the experimental setup we use this is not possible because the electron bunch can not interact with laser pulses on two consecutive turns (see section 2). Such turn-by-turn background could be caused by the electrons hitting something inside the accelerator. To enforce high purity data, the files with such background are rejected.

2012 JINST 7 P01021

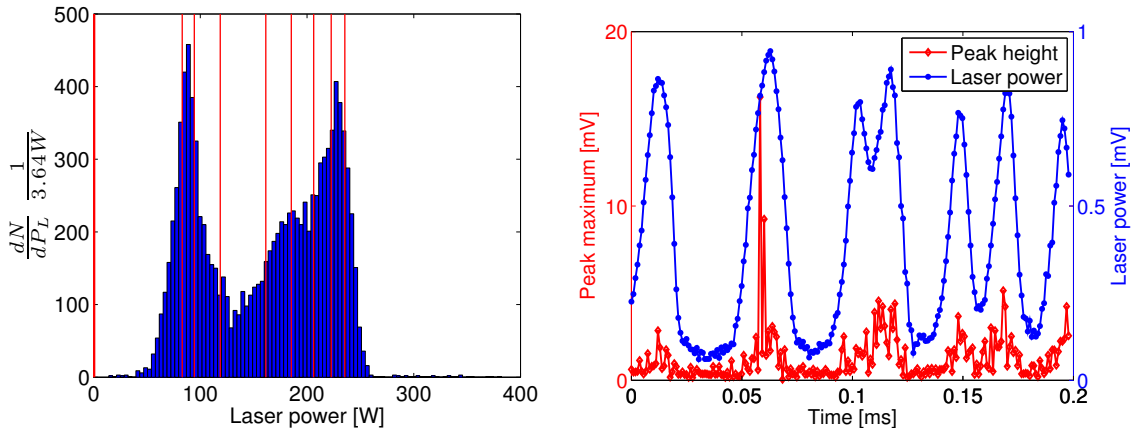

(a) (b)

Figure 8. Figure 8a shows the histogram of the laser power stored in the FPC normalized by its maximum value. Red vertical lines divide the distribution into the nine laser power bins of approximately the same population each (see section 5). Figure 8b gives an example of the correlation between the transmitted FPC laser power and the gamma ray production intensity for a given data file. This can be seen by the correspondence between the peak height distribution (blue line) and the laser power measured by the photodiode at the same time (red line).

Laser power. On the day where the data presented in this article were taken, the average power stored in the FPC was approximately in average 160 W. It was measured by a photodiode placed behind one of the mirrors of the FPC and calibrated with a power-meter. Figure 8a shows the distribution of stored FPC laser power measured by the photodiode. As one can see, the FPC laser power experienced significant fluctuations which can be explained by several resonances in the FPC feedback system. Note that the feedback loop used to stabilize the laser power stored in the FPC had not yet been optimized at the time when these data were taken. On figure 8b the strong correlation between the laser power and the peak height distribution is clearly observed.

4.4 Calibration

In the energy range (tens of MeV) of interest, the calorimeter can be calibrated by using cosmic rays muons. This calibration gives us a relation between the voltage measured on the oscilloscope and the energy deposited in the calorimeter.

In calibration mode the coincidences between two plastic scintillators, one placed at the top and the other at the bottom of the calorimeter, are used to trigger the data acquisition. The signal from the PMT is then digitized by the oscilloscope used to acquire the Compton data. Calibration measurements were performed before each data taking run. A typical measured distribution of pulse heights and pulse integrals is shown on figure 9.

For detectors of moderate thickness such as the one we are using, the energy loss probability distribution is described by the Landau distribution [23]. The most probable energy loss of cosmic muons is the most probable value (MPV) of the Landau distribution.

According to our calibration, the MPV for the integrated signal is (4.87 $\pm$ 0.12) mV·ns and

2012 JINST 7 P01021

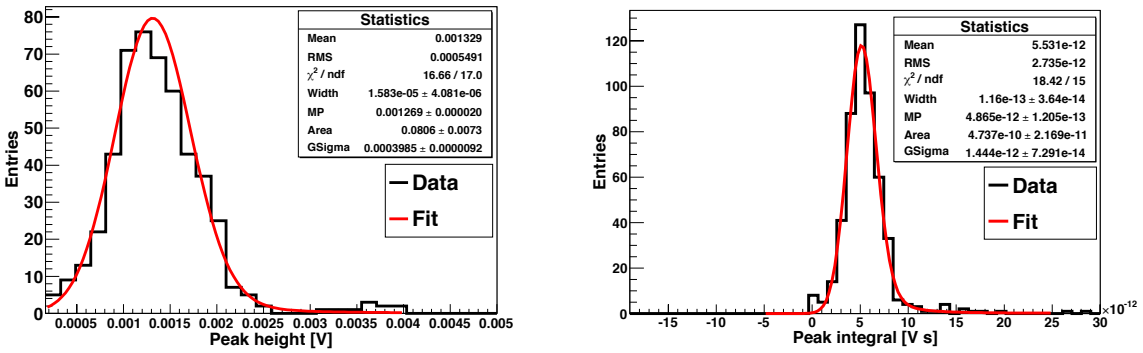

(a) (b)

Figure 9. Energy loss distribution of the cosmic muons in the calorimeter. Figure 9a shows the histogram of the peak heights and figure 9b shows the histogram of the peak integrals. A Landau distribution fit with parameters is shown in both cases.

the MPV for the peak height distribution is (1.27 ± 0.02) mV. Assuming minimum ionization, the energy deposition in the calorimeter is 6.374 MeV/cm [24]. This value corresponds to approximately 45 MeV of energy deposited by a muon passing through the calorimeter. However, this value should be corrected to account for the geometry and the acceptance of the detection system.

To do so, the measure should be scaled by the ratio between the total number of optical photons produced in the BaF_2 crystal and those optical photons which are within the PMT acceptance. Another correction factor appears due to the fact that the two surrounding plastic scintillators are not fully covering the surface of the BaF_2 crystal. Therefore, the previous factor has to be corrected to take into account this difference in overlapping surfaces. To address these two issues we used a Geant4 simulation of the detector which gave a correction factor of $0.745 \pm 0.001(\text{stat}) \pm 0.04(\text{syst})$.

Once, all corrections have been applied, a peak height of 1 mV and peak integral of 1 mV· ns is equivalent in average to (26.6 ± 1.9) MeV and (6.9 ± 0.5) MeV of energy deposited in the calorimeter respectively.

5 Results

The data analysis performed in this study were done to evaluate the number of gamma rays produced during the collisions between the electrons and laser photons.

The spectrum of the gamma rays is shown on figure 10a and 10b. It represents the distribution of the energy deposited in the calorimeter expressed by the peak integrals.[2]

Using our calibration, we can estimate the average number of scattered gammas per bunch crossing. As it was shown in section 3, the mean energy of scattered gammas we measure is 24 MeV. Since the average energy deposited per bunch crossing is 65.1 ± 4.9 MeV, we deduce that approximately 2.7 ± 0.2 gammas are produced in average per bunch crossing (for an average

[2]The similar spectra could be obtained by using the Compton peak height as a measure of energy deposited in the calorimeter.

2012 JINST 7 P01021

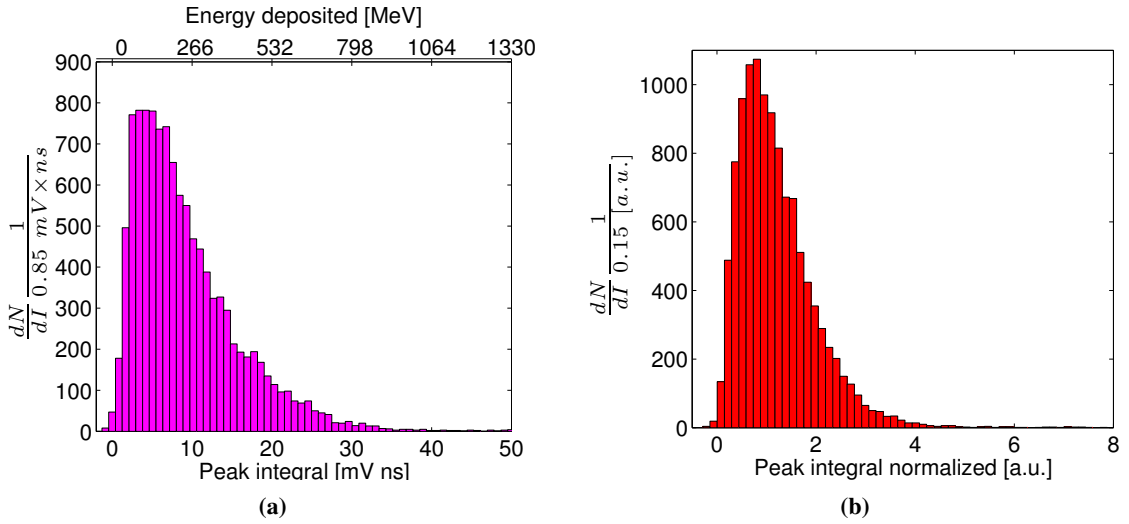

Figure 10. Spectrum of the gamma rays produced for all laser powers. Figure 10a shows the distribution of the integrals of the Compton peaks for the high quality data sample whereas the figure 10b shows the same spectrum normalized by the laser power.

laser power stored in the FPC of about 160 W). This rate of about 2.7 gammas per bunch crossing was successfully sustained over 6 hours until the end of our run. For the given collision repetition frequency in the ATF DR of about 1 MHz, the flux of gamma rays achieved is about 3×10^6 gammas per second (this does not take into account the 0.75 duty cycle of the ATF).

To verify the linearity of the gamma ray flux as a function of the laser power stored in the FPC, we took data over a wide range of laser power (see subsection 4.3). The laser power distribution has been split into the nine bins of approximately 1300 events each as it is shown on figure 8a. Then, the gamma production has been studied within each laser power bin. The spectra of scattered gamma rays which correspond to the different values of laser power stored in the FPC are presented on figure 11a. As expected, the average of the peak integral distribution (energy deposited in the calorimeter by the gamma rays) scales linearly with the laser power stored in the FPC (see figure 11b).

Data — simulations comparison. Simulations were carried out to have a comparison with the gamma ray spectrum obtained experimentally . Noise was introduced in the simulations and quality cuts were applied in the same manner for both data and simulations.

The spectrum of gamma rays measured is shown on figure 12 together with the spectrum simulated for a MPV of 2.7 gammas. The spectrum corresponds to the distribution of the energy deposited in the calorimeter expressed by the peak heights.

Figure 12 shows a very good agreement between the experimental data and simulations.

Highest integrated/instantaneous flux. We scanned our data for the best integrated and instantaneous gamma flux which was produced. The best instantaneous flux we measured (the highest energy deposition) was 34 mV which according to the calibration corresponds to 904 ± 65 MeV deposited in the calorimeter. Assuming 24 MeV per gamma, this gives about 38 ± 3 gammas produced per bunch crossing. The corresponding Compton peak can be seen on figure 13.

2012 JINST 7 P01021

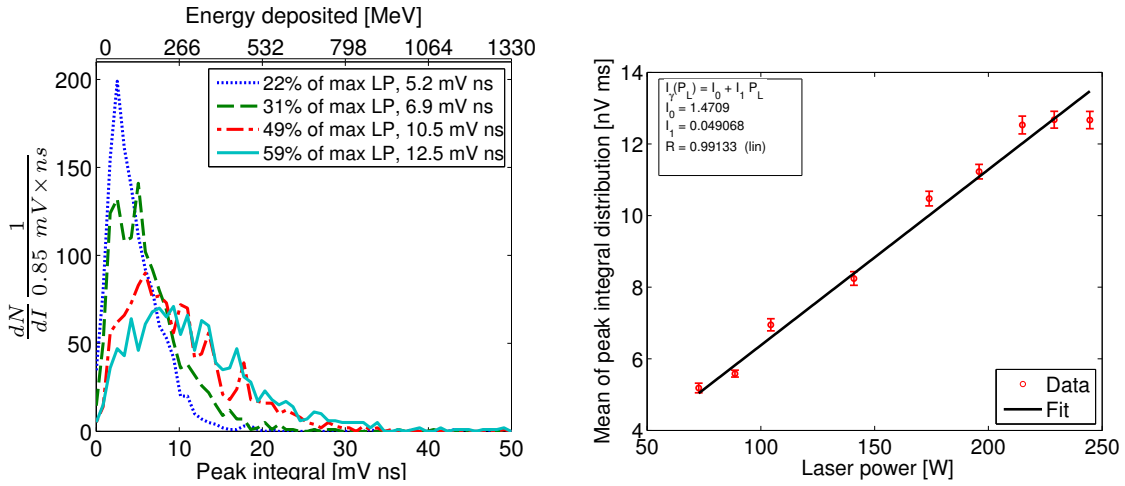

(a) **(b)**

Figure 11. Figure 11a presents gamma spectrum for different FPC stored laser power. Different colors correspond to the spectra taken at different FPC powers. In the legend, the fraction of the maximum FPC stored power and the mean of each of these spectra are shown. Figure 11b shows the linear relation between the mean of gamma spectra for each laser power bin and the correspondent laser power which is defined as a mean of the laser power bins shown on figure 8a. The errors bars indicate the statistical errors.

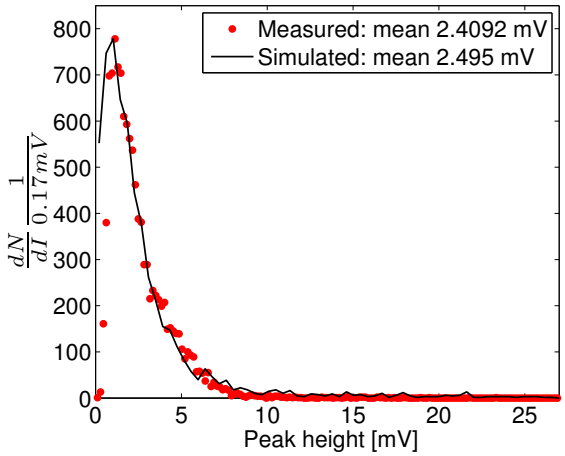

Figure 12. Comparison between the measured and simulated energy spectra of the gamma rays resulting from Compton scattering. The black solid line represents the simulated spectrum and the circles dots represent the measured gamma ray energy distribution expressed in the peak heights. For the simulations the events occur according to a Poisson process with a rate of 2.7 gammas per bunch crossing. The data presented are the same than those of figure 10a.

For the many applications of accelerator driven Compton sources an important characteristic is the total gamma flux. Table 3 summarizes the results concerning the highest gamma ray flux integrated over 0.2 ms (duration of one data file) for different ATF DR filling modes. As one can see, the total flux does not scale linearly with the number of electron bunches stored in the DR contrary to what was expected. Additional studies should be conducted to investigate this issue.

2012 JINST 7 P01021

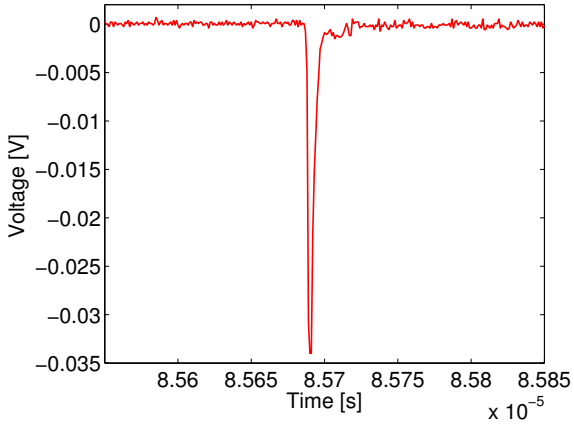

Figure 13. Part of the data file containing the highest energy deposited in the calorimeter per one shot which is about 904 MeV. Waveform shows this event which stands for the highest instantaneous gamma flux we measured. It is equivalent to 38 gammas produced in one bunch crossing.

Table 3. Highest integrated gamma ray flux achieved.

Electron pulse structure	Total intensity over 0.2 ms	Energy deposited over 0.2 ms	Integrated flux over 0.2 ms	Integrated flux over 1 s	Systematic error
1 train	893 mV	23750 MeV	990 γ	$\sim 4.9 \times 10^6$ γ	7%
2 trains	910 mV	24210 MeV	1010 γ	$\sim 5.0 \times 10^6$ γ	7%
3 trains	1010 mV	26800 MeV	1120 γ	$\sim 5.6 \times 10^6$ γ	7%

Figure 14 shows the three data files having the best integrated gamma ray flux.

6 Conclusion and outlook

The MightyLaser project has demonstrated the production of gamma rays using a non-planar four-mirror FPC. In average, 2.7 ± 0.2 gammas are produced per bunch crossing. This result is in agreement with the CAIN simulations for the FPC laser power achieved in the experiment. A good agreement is also observed between the measured and simulated energy spectra of the gamma rays using Geant4 toolkit. The highest integrated flux of 1120 ± 80 gammas over 0.2 ms ($\sim 5.6 \times 10^6$ gammas per second) in three trains mode and an instantaneous flux of 38 ± 3 gammas per bunch crossing were measured. These values are limited by the FPC laser power obtained so far.

Work to improve the laser stability and increase the FPC finesse has been interrupted by the earthquake which hit Japan in March 2011. Operation of the ATF at KEK is to be resumed soon. Our objective for the next campaign is to increase production of high energy gamma rays by several orders of magnitude by increasing both the FPC finesse and the input laser power.

2012 JINST 7 P01021

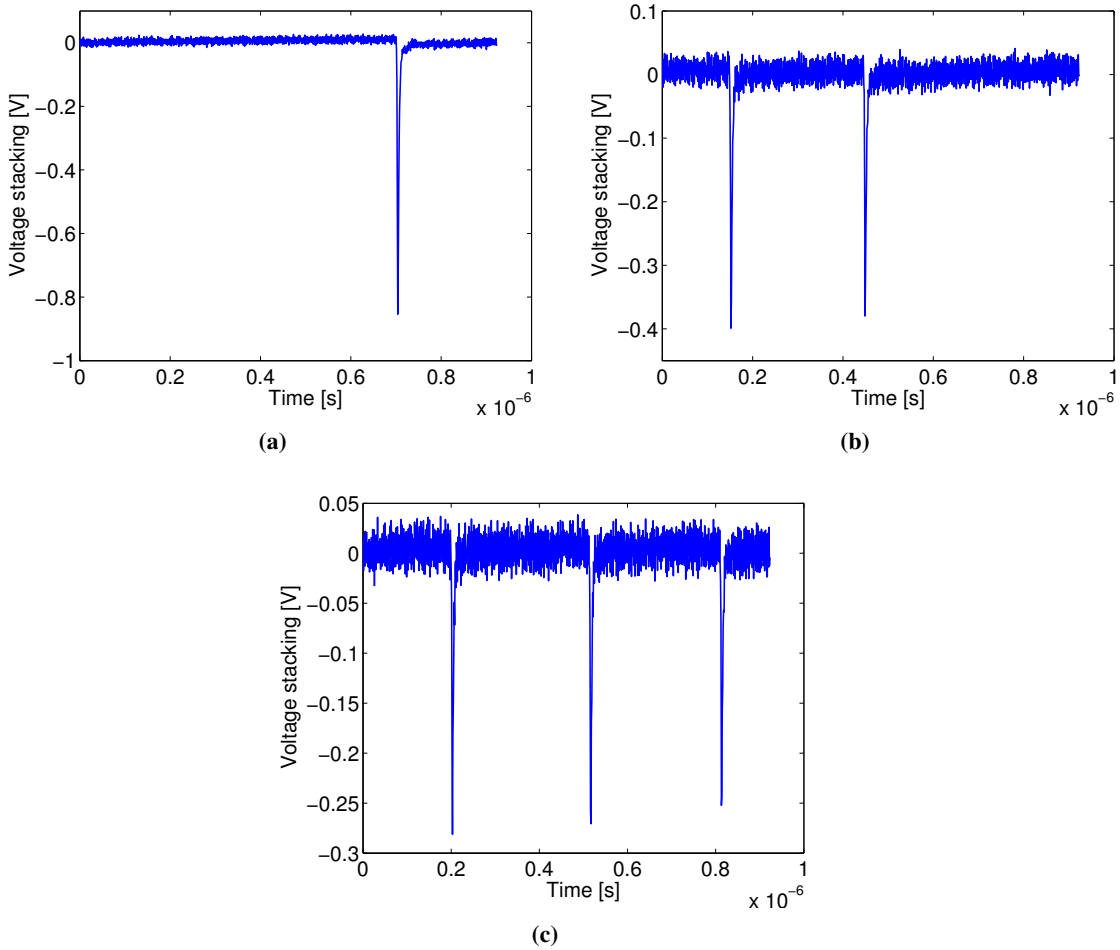

Figure 14. Illustration of three data files containing the highest integrated flux over 0.2 ms for different ATF DR filling modes: one bunch stored in the DR (figure 14a), two trains of one bunch each stored in the DR (figure 14b) and three trains of one bunch each stored in the DR (figure 14c). The figures show all the periods of a given file stacked together.

Acknowledgments

This work has been funded by the French ANR (Agence Nationale de la Recherche) contract number BLAN08-1-382932 and P2I (Physique des 2 Infinis). The authors would like to thank the staff from KEK for their hospitality.

References

[1] J. Bonis et al., *Non-planar four-mirror optical cavity for high intensity gamma ray flux production by pulsed laser beam Compton scattering off GeV-electrons*, to be submitted to *JINST* [arXiv:1111.5833].

[2] S. Araki et al., *Conceptual design of a polarised positron source based on laser Compton scattering*, physics/0509016.

2012 JINST 7 P01021

[3] M. Kuriki et al., *ILC positron source based on laser Compton*, *AIP Conf. Proc.* **980** (2008) 92.

[4] O. Dadoun et al. *The baseline positron production and capture scheme for CLIC*, in 1st *International Particle Accelerator Conference: IPAC'*10, Kyoto Japan May 23–28 2010.

[5] P. Walter et al., *A new high quality X-ray source for cultural heritage*, *Comptes Rendus Physique* **10** (2009) 676.

[6] ThomX collaboration, *Thomx CDR*, IN2P3-00448278, IN2P3, France (2010).

[7] A. Loulergue et al., *A compact ring for the ThomX-ray source*, in 1st *International Particle Accelerator Conference: IPAC'*10, Kyoto Japan May 23–28 2010.

[8] J. Urakawa, *Development of a compact x-ray source based on compton scattering using a* 1.3 *GHz superconducting RF accelerating linac and a new laser storage cavity*, *Nucl. Instrum. Meth.* **A 637** (2010) S47.

[9] P. Sprangle et al., *Tunable, short pulse hard x-rays from compact laser synchrotron source*, *J. Appl. Phys.* **72** (1992) 5032.

[10] H. Kogelnick and T. Li, *Laser beams and resonators*, *Appl. Opt.* **5** (1966) 1550.

[11] Z. Huang and R.D. Ruth, *Laser-electron storage ring*, *Phys. Rev. Lett.* **80** (1998) 976.

[12] F. Hinode et al., *ATF accelerator test facility design and study report No.* 4, http://lcdev.kek.jp/ATF/Pub/KEK-I-95-4.pdf, KEK, Tsukuba Japan (1995).

[13] H. Shimizu et al., *Photon generation by laser-compton scattering using an optical resonant cavity at the KEK-ATF electron ring*, *J. Phys. Soc. Jap.* **78** (2009) 074501.

[14] S. Miyoshi et al., *Photon generation by laser-Compton scattering at the KEK-ATF*, *Nucl. Instrum. Meth.* **A 623** (2010) 576 [arXiv:1002.3462].

[15] H.Hayano et al., *Accelerator test facility study report JFY* 1996–1999, KEK Internal report 2000-6, KEK, Tsukuba Japan (2000).

[16] P. Bambade et al., *Present status and first results of the final focus beam line at the KEK Accelerator Test Facility*, *Phys. Rev. ST Accel. Beams* **13** (2010) 042801.

[17] T. Naito et al., *Timing system for multi-bunch/multi-train operation at ATF-DR*, KEK Preprint 99-144, KEK, Tsukuba Japan (1999).

[18] S. Miyoshi, *Development of polarized positron source by laser Compton scattering with optical resonant cavity*, Ph.D. thesis, Graduate School of Advanced Sciences of Matter, Hiroshima University, Hiroshima Japan (2011).

[19] GEANT4 collaboration, S. Agostinelli et al., GEANT4*: a simulation toolkit*, *Nucl. Instrum. Meth.* **A 506** (2003) 250.

[20] K. Yokoya, *User manual of CAIN, version* 2.40, (2009).

[21] T. Suzuki, *General formulae of luminosity for various types of colliding beam machines*, KEK note 76-3, KEK, Tsukuba Japan (1976).

[22] V.B. Berestetskii et al., *Quantum electrodynamics*, volume 4, Butterworth-Heinemann, Oxford U.K. (1982).

[23] L. Landau, *On the energy loss of fast particles by ionisation*, *J. Phys. USSR* **8** (1944) 201.

[24] D. Groom, *Atomic and nuclear properties of materials. Particle Data Book*, http://pdg.lbl.gov/2011/AtomicNuclearProperties/, (2011).

2012 JINST 7 P01021

GAMMA-RAYS GENERATION WITH 3D 4-MIRROR CAVITY FOR ILC POLARIZED POSITRON SOURCE*

T. Akagi†, M. Kuriki, S. Miyoshi, T. Takahashi, R. Tanaka, H. Yoshitama,
Hiroshima University, Japan
S. Araki, Y. Funahashi, Y. Honda, T. Okugi, T. Omori, H. Shimizu, N. Terunuma, J. Urakawa,
KEK, Tsukuba, Japan
K. Sakaue, M. Washio, Waseda Univ., H. Kataoka, T. Kon, Seikei University, Japan

Abstract

We are developing a ILC polarized positron source based on the laser-Compton scattering. We have already performed a photon generation experiment at the KEK-ATF using a Fabry-Perot type 2-mirror laser pulse stacking cavity [1]. The laser pulses are accumulated and their power was enhanced in the Fabry-Perot cavity. In order further improve performance of the laser power enhancement, a new three dimensional 4-mirror cavity is designed. In this article, we report status of the photon generation experiment.

INTRODUCTION

We are developing ILC polarized positron source based on the laser-Compton scattering. The generation of polarized positron by laser-Compton scattering was already verified [2], [3]. In this scheme, tens of MeV photons can be generated by collisions of laser photons with about 1 GeV electron beam. To increase the intensity of generated photons by laser-Compton scattering, increasing intensity of laser pulses and focusing at collision point by accumulation them in an optical cavity.

We already achieved laser intensity enhancement of 760 and laser waist size is 30μm (1σ) by the 2-mirror Fabry-Perot cavity. To increase the intensity of generated photons more, it is necessary to use high reflectivity mirrors and to make laser waist size smaller. However, it is difficult to achieve the improvement of enhancement and focusing performance at the same time with a 2-mirror Fabry-Perot cavity. Thus, to achieve the two requirement, now we developed three dimensional 4-mirror cavity.

4-MIRROR CAVITY

In order to increase the number of generated photons by laser-Compton scattering, it is necessary to increase the enhancement factor of the optical cavity by using the high reflectivity mirrors and make the laser waist size small. However, it is difficult to make laser waist size smaller than present waist size (30μm) with the 2-mirror Fabry-Perot cavity since it is sensitive to misalignment by its nature.

To reduce the laser waist size with 2-mirror cavity, cavity has to be concentric type ($\rho \sim L/2$), where ρ is the curvature radius of mirror and L is the length of Fabry-Perot cavity. This type is very sensitive to transverse mirror misalignment. In other words, it is unstable as a resonator. On the other hand, in 4-mirror cavity, it is possible to reduce the laser waist size with confocal type ($\rho \sim L$). The 4-mirror cavity consists of two plane mirrors and two concave mirrors, and the confocal type is insensitive to transverse misalignment. So the 4-mirror cavity can be stable with a small laser spot size.

However, in the 4-mirror cavity, effective focal length (f_t, f_s) are different in tangential plane and sagittal plane, and the difference causes astigmatism at the focal point. f_t and f_s are expressed as

$$f_t = \frac{\rho}{2}\cos\theta \quad (1)$$

$$f_s = \frac{\rho}{2\cos\theta} \quad (2)$$

where θ is reflection half angle of concave mirror. Because of this astigmatism, laser profile inside the 4-mirror cavity will be ellipse in principle.

To avoid the astigmatism, the cavity has to be three dimensional configuration. Our 3D 4-mirror cavity is shown in Fig. 1. 3D 4-mirror optical cavity generally have a circular polarization dependent property due to the rotation of the image in the three dimensional optical path. And a new method utilizing this property to obtain a differential signal can be lock an optical cavity at a resonance peak [4].

Circular Polarization Property

In a 3D 4-mirror cavity, only circular polarized light can be stored due to the rotation of the image in the three dimensional optical path. We lock a 4-mirror optical cavity at resonance peak using this property.

A linear polarization light was injected to the 4-mirror cavity. Then we measured the output of the differential amplifier while scanning the cavity length. The setup and signal observed is shown in Fig. 2, Fig. 3. The top line is the signal of the photo-diode that measured the transmission.

* Work supported by the Quantum Beam Technology Program of MEXT.
† tomoya-akagi@hiroshima-u.ac.jp

ISBN 978-3-95450-115-1

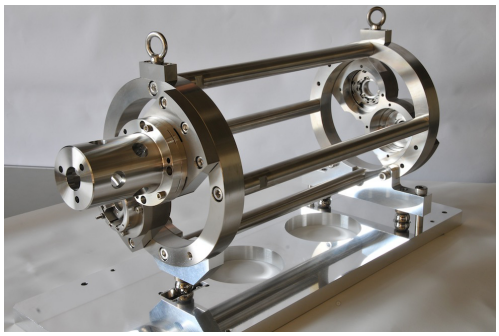

Figure 1: 3D 4-mirror cavity.

And it shows the points that the cavity's resonance of right and left-handed polarized light. The bottom line is output of the differential amplifier. The signal crossed zero at the point of resonance. The circular polarization peak can be switched with this differential signal. It means the polarization of the generated photons by laser-Compton can be switched quickly.

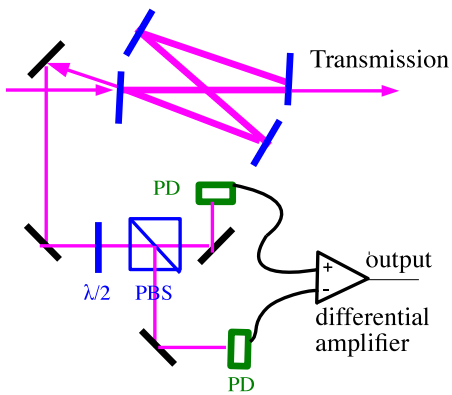

Figure 2: Setup to obtain the differential signal.

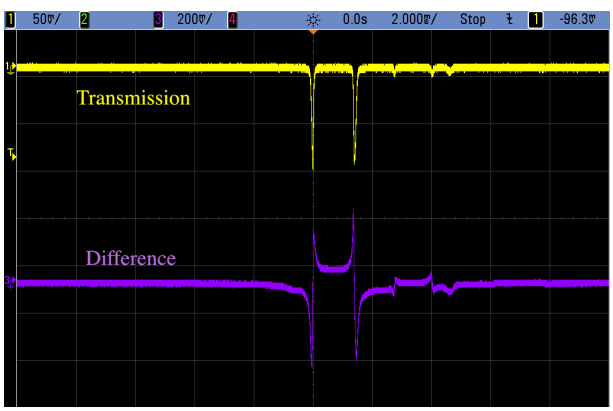

Figure 3: Signal of transmission and difference.

Focusing Property

Focusing property of three dimensional 4-mirror cavity is depend on a geometry of mirrors. Schematic of our 3D 4-mirror cavity is shown in Fig. 4. The configuration of this 4-mirror cavity is slightly twisted. Because, to control the effect of the rotation of the image in the three dimensional optical path.

The calculation of laser spot size at collision point is shown in Fig. 5. In this calculation curvature radius of mirror, ρ is 420mm. The laser profile in a 3D 4-mirror cavity is generally ellipse on a small spot size. According to calculation, our 3D 4-mirror cavity can be achieved $\sim 15\mu m(1\sigma)$ with almost circle laser profile.

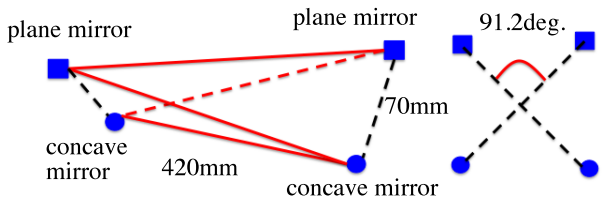

Figure 4: Schematic of the three dimensional 4-mirror cavity.

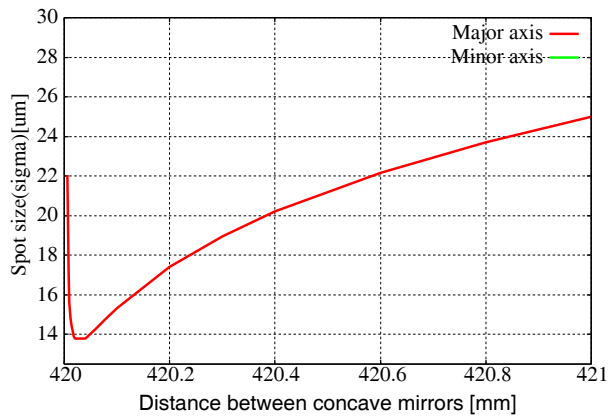

Figure 5: Spot size at collision point.

EXPERIMENT WITH THE 3D 4-MIRROR CAVITY

We performed gamma-rays generation experiment by laser-Compton scattering at the KEK-ATF. The crossing angle of the laser pulses and the electron beam is 14°, which determined the maximum energy of the Compton gamma at 28MeV. The energy of the gamma-rays was discriminated by the slit placed between the laser-electron interaction point and the gamma-ray detector. As a result, the energy of gamma-rays detected in the detector is 19-28MeV with the average of 24.5MeV. The parameters of the electron beam in the ATF DR are in Table 1.

We installed the 4-mirror cavity in the north straight section of ATF damping ring in the summer of 2011. The

ISBN 978-3-95450-115-1

Table 1: Parameters of ATF DR

Description	Value
Electron energy	1.28 GeV
Beam intensity	1×10^{10} e / bunch
Bunch spacing	5.6 ns
Beam size (σ_x / σ_y)	100 / 10 μm
DR revolution	2.16 MHz

optics and the 4-mirror cavity are placed on the movable table. We scanned the position of the optical cavity relative to the electron beam to find the optimum position. Then, the timing of laser pulses relative to electron bunches was adjusted by changing relative phase between the ATF master oscillator and laser pulses. The parameters of our laser system are in Table 2.

Table 2: Parameters of Laser System

Description	Value
Laser wavelength	1064 nm
Laser frequency	357 MHz
Laser power	10 W (28 nJ/ pulse)
Finesse of 4-mirror cavity	5000
Average power stored in cavity	700 W
Crossing angle	14 deg.

RESULT

The laser position dependence of the number of gamma-rays and energy distribution at the optimum position is shown in Fig. 6, Fig. 7.

In the vertical position scanning plot, $\sigma = 17\mu$m. It is convolution of electron beam and laser spot size. At this time, electron beam size was $10 \pm 1\mu$m and expected laser size is 15μm. So the width of vertical scan plot is reasonable.

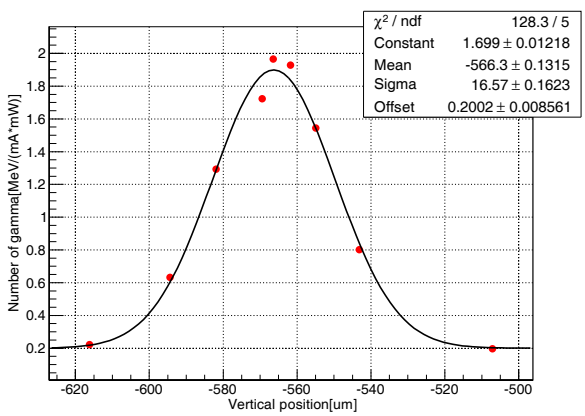

Figure 6: Vertical laser position scan.

And we detected 780MeV gamma-rays per crossing with 5 bunches operation. The average energy of 1γ is 24.5MeV, it is $\sim$32 photons per crossing. Since the revolution of the electron bunches in the ATF DR is 2.16MHz, it can be estimated that $\sim 7 \times 10^7$ photons are generated per second.

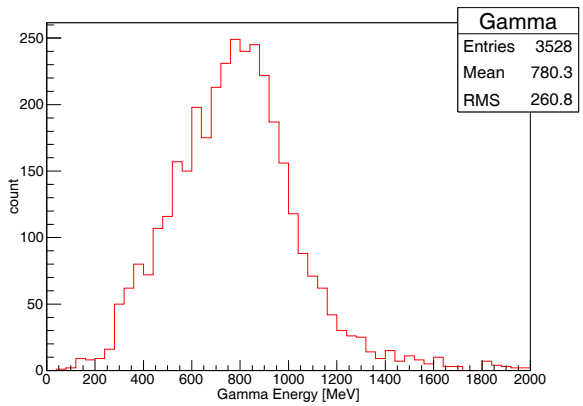

Figure 7: Energy distribution of gamma-rays with 5 bunches operation.

SUMMARY

In order to increase the number of generated photons by laser-Compton scattering, we installed 3D 4-mirror optical cavity in the ATF DR and performed gamma-rays generation experiment using that cavity. Then we detected $\sim$32 photons per crossing with 5 bunches operation.

Laser spot size at collision point seems to be achieved design value. On the other hand, stored laser power in the 4-mirror cavity has to be improve. For example, we need more coupling efficiency (currently, it is $\sim$0.5).

REFERENCES

[1] S. Miyoshi et al., Nucl. Inst. Meth. A 623 (2010) 576.

[2] M.Fukuda et al., Phys. Rev. Lett. 91, 164801(2003)

[3] T.Omori et al., Phys. Rev. Lett. 96, 114801(2006)

[4] Y. Honda et al., Opt. Commun. 282 (2009) 3108.

ISBN 978-3-95450-115-1